Chapter 10

Mass transport processes, injectites and styles of sediment remobilization

Alves, T.M., 3D Seismic Laboratory, School of Earth and Environmental Sciences, Cardiff University, Main-Building – Park Place, Cardiff CF10 3AT, United Kingdom (alvest@cardiff.ac.uk).

Cardona, S., Sediment Mechanics Lab, Department of Geology & Geophysics, Texas A&M University, 3115 TAMU, College Station, Texas 77843, USA (scardona@tamu.edu)

Rodrigues, M.C.N.L., Laboratory on Basin Analysis (Laboratório de Análise de Bacias, LABAP), Departamento de Geologia - Setor Ciências da Terra, Universidade Federal do Paraná, Centro Politécnico - Jardim das Américas – Curitiba, Post Office Box 19027, CEP 81532-980, Brazil (merolyn.rodrigues@ufpr.br)

ABSTRACT

Sediment remobilization of seafloor strata is linked to the early stages of sediment burial, diagenesis and fluid migration in different geological settings. It can impact the depositional architecture of a sedimentary basin by promoting local and widespread erosion while, in parallel, lead to an overall redistribution of near-seafloor strata (the mass movement *per se*). It can also generate relatively deep sediment injections, fluid-flow features and associated sediment extrusion. Sediment remobilization plays an important role in hydrocarbon-rich basins. Mass transport complexes and deposits can contain reservoirs intervals or constitute competent seal units. Sediment injections can form either reservoirs or comprise routes for fluid migration (sand injectites). The existence of deep hydrocarbon reservoirs is often associated with fields of mud volcanoes. This Chapter highlights sediment remobilization

processes as being significant due to their societal, economic and ecological impact as both geohazards and hydrocarbon indicators. While associated with hydrocarbon shows and prolific accumulations at depth, some of these processes can be also damaging to infrastructure, local populations and marine life. In addition, mass movement on continental slopes, volcanic islands or seamounts can trigger catastrophic tsunamis.

Keywords: Sediment remobilization; mass transport; sand and fluid injection; hydrocarbons; societal impact; economic impact.

INTRODUCTION

Sediment remobilization is a common process associated with the early stages of sediment burial, diagenesis and fluid migration in sedimentary basins. It can be divided into two main types depending on their relative timing and depth of occurrence: a) mass transport deposits, or complexes, materializing erosion and an overall redistribution of near-seafloor strata, and b) relatively deeper sediment injections and fluid-flow features, capable of extruding sediment onto the seafloor and surface. This Chapter will focus on mass transport as a process and review associated deformation styles. The aim is to understand the diagnostic features that identify them at outcrop and seismic data in hydrocarbon-rich basins. The styles of sediment remobilization resulting from fluid flow, and the build-up of overpressure in sediment, will also be summarized in this work and identified as a key process occurring below the surface in many a sedimentary basin.

Mass transport deposits (MTDs) and mass transport complexes (MTCs) are often used interchangeably in the scientific community, despite representing distinct scales and degrees of instability on continental slopes. The various types of mass movements occurring in nature generate a wide spectrum of deposits, which are better referred to as mass transport complexes (MTCs) when they are clearly associated in space and time (see Pickering and Hiscott, 2016). Such a broad definition considers all types of gravitational flows, including non-cohesive turbidites and grainflows, as comprising mass transport complexes. However, this Chapter considers sediment remobilization as involving the reworking of previously deposited sediments; therefore, these sediments tend to have a degree of cohesion during their transport and hence exhibit laminar behavior. This is a key characteristic that distinguishes remobilized deposits (e.g., debrites, slumps, slides) from turbidites (Middleton and Hampton, 1976). As the most recent literature discriminates between MTDs and MTCs based on their geometry and character on seismic, borehole and outcrop data, when a single landslide event is believed to have generated a single deposit this is called *mass transport deposit* (MTD). When several stacked MTDs are identified on seismic and sedimentological data, often based on the recognition of distinct basal glide zones separating successive, but discrete MTDs, the term most often used is *mass transport complex* (MTC) (Pickering and Hiscott, 2016). Significantly, while MTDs and MTCs typically occur in marine or lacustrine (i.e., sub-aqueous) environments, sediment injection and associated fluid flow can occur in both onshore and offshore sedimentary basins (Hurst et al., 2011; Andresen, 2021). The notion that mass transport complexes (MTCs) and deposits (MTDs) can be associated with hydrocarbon accumulations is not novel among explorationists (Fairbridge, 1946). Such deposits have historically been considered as a depositional facies to avoid from a viewpoint of hydrocarbon exploration (Posamentier and Kolla, 2003; Weimer and Slatt, 2004), but it is now understood that MTCs and MTDs can contain hydrocarbon source intervals (Tanavsuu-Milkeviciene and Sarg, 2012; Johnson et al., 2015), reservoirs (Shanmugam et al., 2009; Meckel, 2011; Bhatnagar et al., 2019), or constitute competent seal units (Godo, 2006; Alves, 2010a; Algar et al., 2011; Cardona et al., 2016, 2020b; Kessler and Jong, 2018; Amy, 2019) –

see Chapter 7 in this book. In addition, the relief created by the emplacement of MTCs and MTDs on the seafloor can influence the pathways of post-emplacement turbidite flows (Armitage et al., 2009; Jackson and Johnson, 2009; Kneller et al., 2016; Ward et al., 2018; Henry et al., 2018) creating space on the seafloor for "healing phase" top-fill reservoir targets (Wood et al., 2015). Examples of such a control on hydrocarbon trapping and accumulation are documented in the Ubit field of Nigeria, with ~2 billion barrels of oil (BBO) (Clayton et al., 1998), the Tarn field in the North Slope Borough of Alaska with ~100 MMBO, and the Meltwater field also in the North Slope of Alaska with ~50 MMBO (Houseknecht and Schenk, 2007; Houseknecht, 2019), to name three examples.

Sediment remobilization occurs in multiple geological settings, and can markedly impact the depositional architecture of a sedimentary basin (Roy et al., 2019; Palan et al., 2020; Wenau et al., 2021). Furthermore, it is capable of redistributing sub-surface stresses, fluid and heat, in quasi-instantaneous episodes at the geological time scale (Ho et al., 2018; Roelofse et al., 2020). An example is the loss of effective pressure below the paleo-seafloor when large landslides occur via the sudden escape of fluid to the surface, as documented in large, blocky MTDs (Alves, 2010b, 2015). Vast areas with sand injections – themselves representing fluid migration paths and overpressure markers - are also strong enough to redistribute fluid and sediment through previously competent seal units (Sun et al., 2017). Finally, the largest of MTCs on continental margins, namely those associated with the mobilization of slide blocks (also named megaclasts) and subsequent deposition of megabreccias, have been systematically documented to form key markers of tectonism in sedimentary basins. This tectonism can occur at a regional scale (Alves, 2015; Festa et al., 2016; Naranjo-Vesga et al., 2020), or locally in association with tectonically controlled topography (Alves and Cupkovic, 2018).

As summarized in Chapter 6, MTDs and MTCs comprise a wide spectrum of deposits and represent distinct styles of sediment movement, or remobilization. MTDs and MTCs include rock falls, creeps, slides, slumps, and flows presenting some degree of internal cohesion – therefore excluding turbidites and non-cohesive grainflows from their definition. They can comprise more than 50% of the sedimentary record of a single continental margin and are known to respond to varied tectonically and climatically driven triggers (Masson et al., 2006). Hence, modern sediment remobilization processes fall into the realm of Geohazards in economic and physical terms.

This Chapter is divided in specific sections addressing aspects of sediment remobilization in sedimentary basins (**Figure 1**). After this introductory part, a review of the current knowledge (state-of-the-art) about fluid remobilization is developed as a way to inform readers of recent developments under this theme. The regional distribution of field analogues and recognized areas with sediment remobilization are summarized in the following sections, and complemented with relevant examples in seismic data. The paper will conclude on how the analysis of mass transport deposits or complexes at different scales may help to define the potential impact of such sediment remobilization in petroleum plays, as well as the importance of studying sediment remobilization to realize its potential as a geohazard.

DATA AND METHODS

This work uses three-dimensional (3D) seismic and outcrop data from distinct regions to illustrate common aspects of MTCs and MTDs. In particular, our work will present seismic examples from Trinidad and Tobago, Niger Delta and the North Sea, and outcrop data from

Crete (Eastern Mediterranean), Taranaki Basin (New Zealand), and Paraná Basin (South Brazil) (**Figure 1**).

Seismic interpretation

Seismic data in this work include vertical seismic profiles of high resolution and quality, complemented by seismic-attribute maps taken from the published literature. To characterise MTCs, seismic attributes of interest include root-mean-square (RMS) amplitude, maximum magnitude and coherence (or variance), all capable of highlighting structural and depositional features of particular areas of continental slopes affected by slope instability (see Alves et al., 2014). In detail, root-mean-square (RMS) amplitude maps depict the average squared amplitude from individual samples within a defined interval (Brown, 2011). Maximum magnitude undertakes a similar process, but the seismic amplitudes computed are all positive, thus stressing the presence of the higher amplitude features against low-amplitude background strata. Coherence attributes convert a seismic volume of continuity (normal reflections) into a volume of discontinuity, allowing features such as faults, folds and ridges, and stratigraphic boundaries, to be emphasized on time slices (Marfurt and Alves, 2015). The locations of the seismic surveys and outcrops used in this study are shown in **Figure 1**.

Outcropping mass transport deposits in SE Crete (Eastern Mediterranean)

In SE Crete occur a series of Miocene-Quaternary units deposited on the tectonically active continental slopes that bordered what were, at the time, multiple islets and transtensional/extensional basins in the South Aegean Sea (Alves and Cupkovic, 2018; Sakellariou and Tsampouraki-Kraounaki, 2019) (**Figure 1**). The area has been used as an analogue of a marine rift basin, distinct from the Gulf of Corinth and Sperchios Basin in Central Greece insomuch as slope depositional processes dominate over the shallow-marine to continental facies predominating in Central Greece. Furthermore, the erosion of distinct, and spatially variable, basement units allows a more complete understanding of the effect of basement lithology and regolith types on sediment distribution.

Mass transport and turbidite deposits predominated in what is now Crete during a Serravalian-Tortonian ‘syn-rift’ phase that led to widespread deepening of transtensional/extensional basins. At the end of the Miocene, at least four (4) individual islands composed what is now the elongated E-W island of Crete, and the slopes of these islands were bordering transtensional basins roughly striking N20 and N70 (Alves and Lourenço, 2010). Marine deposits predominated in this overall tectonic setting, leading to the concomitant deposition of proximal, coarser deposits near the four highs (islands) that existed at the time, slope turbidites and mass transport deposits on adjacent slopes, and deep-marine clays in the main basin depocenters. In SE Crete, it is possible to map and document the juxtaposition of such facies, and to record the geometry of mass-wasting deposits sourced from distinct basement lithologies.

Outcropping mass transport deposits in the Taranaki Basin (New Zealand)

In the North Island, New Zealand, Late Miocene (Tortonian) outcrops of MTDs are exposed in the Lower Mount Messenger Formation (LMMF). Following its initial development within a synrift setting, the Taranaki Basin evolved as a passive margin in Late Cretaceous to Paleogene times (King & Thrasher, 1996; Strogen et al., 2017). Structural, sedimentological and paleogeographic evidence shows that the Taranaki Basin remained as a passive margin throughout much of the Paleogene (King & Thrasher, 1992; Baur et al., 2014; Strogen et al., 2014).

The case study used in this Chapter is the Rapanui MTD (RMTD). The outcrops of this study were deposited in middle to lower bathyal water depths during the Late Miocene (King et al., 1993) (**Figure 1**). The shelf was relatively narrow (ca. 10 to 15 km wide) and located immediately east of the study area (King et al., 2011). In general, the regional Late Miocene paleoflow direction in the Taranaki basin was to the northwest (King et al., 2011; Masalimova et al., 2016). These clastic sediments were mixed with coeval volcaniclastic material derived from the submarine andesitic Mohakatino volcanic arc in the northern offshore part of the basin (Giba et al., 2013; Shumaker et al., 2018) and were punctuated by several MTDs (King et al., 2011; Rotzien et al., 2014; Sharman et al., 2015; Masalimova et al., 2016).

Outcrop examples from Paraná Basin (S Brazil)

The outcrop examples from South Brazil correspond to MTDs from the Itararé Group, exposed in three regions along the east border of Paraná Basin, and studied by Rodrigues et al. (2020). The Paraná Basin is considered to form a large elongated (NNE-SSW) intracratonic basin (up to 1,600,000 km^2) situated in southeast South America (**Figure 1**). The stratigraphy and structural evolution of the Paraná Basin were controlled by tectonic trends inherited from a heterogeneous basement, which comprises cratonic terrains and orogenic belts agglutinated during the Brazilian Orogeny (Zalán et al., 1990). Several eustatic–tectonic cycles reactivated the basement structural trends and controlled sedimentation from the Ordovician to the Early Cretaceous (Milani et al., 1994).

The Itararé Group (late Mississippian to Cisuralian) forms the lower half of a Permian-Carboniferous supersequence that is up to 2.5 km-thick (Schneider et al., 1974; Zalán et al., 1990; França and Potter 1991; Holz et al., 2010). Sediments were mostly accumulated in marginal to relatively deep-marine environments during multiple deglaciation episodes associated with the late Paleozoic ice age affecting southwestern Gondwana (França and Potter, 1991; Vesely and Assine, 2006; Fallgatter, 2015; Valdez-Buso et al.; 2019). França and Potter (1991) subdivided the Itararé Group into three basin-wide lithostratigraphic intervals that correspond broadly to the formations previously defined by Schneider et al. (1974) and can be correlated with the three palynozones defined by Souza (2006). The outcrop examples include MTDs from Lagoa Azul, Campo Mourão and, mainly, Taciba Formation, comprising the best outcrop exposures, particularly in the southernmost region of Rio do Sul (**Figure 1**).

After the deposition of the Itararé Group, the Paraná Basin was affected by tectonic deformation related to the reactivation of ancient basement faults. This was due to convergence at the active margin of the South American Plate and opening of the Atlantic Ocean (Zalán et al., 1990; Soares, 1991; Milani 1997, 2004). Yet, this post-sedimentary deformation is easy to differentiate from mass transport deformation - brittle structures formed during the youngest deformation episodes crosscut several layers and deposits and are associated with regional structures (Rostirolla et al., 2000; 2002; 2003; Trzaskos et al., 2006).

CLASSIFYING SEDIMENT REMOBILIZATION ON SEISMIC AND OUTCROP

Fundamentally, the processes behind sediment remobilization (i.e., mass transport) occur when the shear component of gravity, as an underlying force, surpasses the shear strength of a deposit due to allogenic or autogenic factors (Dott, 1963; De Blasio, 2011).

Such phenomena are more likely to occur in poorly consolidated sediments (i.e. sediments near the surface or seafloor) than in deeply buried (> ~100 m) units, although evidence for large-scale remobilization of slide blocks is recorded in areas such as offshore Morocco (Dunlap et al., 2010), SE Brazil (Gamboa et al., 2010), Alaska's North Slope (Bhattacharya et al., 2020)) and off Greenland (Cox et al., 2020). Therefore, sediment remobilization is not an uncommon phenomenon and can occur in subaerial and subaqueous environments. Consequently, deposits resulting from sediment remobilization have been documented across different geologic periods in both siliciclastic (Ogiesoba and Hammes, 2012; Cardona et al., 2016; Sun and Alves, 2020; Gutierrez and Snedden, 2021; Steventon et al., 2021) and carbonate settings (Eyles and Eyles, 2001; Jablonská et al., 2018; Le Goff et al., 2020). More recently, they have also been documented in mixed-composition settings (Moscardelli et al., 2019; Cumberpatch et al., 2020; Walker et al., 2021).

Historically, and following the definition of Pickering and Corregidor (2005), deposits resulting from sediment remobilization were routinely termed by the energy industry as mass transport complexes (MTCs). This term was first introduced by Weimer (1989) and its original definition had a clear sequence stratigraphic meaning. Later, Weimer and Shipp (2004) considered the term MTC as applying to "…features at a scale that can only be completely imaged on volumetrically large seismic surveys". Recent studies have demonstrated that deposits identified as MTCs are often composed of multiple individual mass transport deposits (MTDs) typically below the resolution of conventional seismic data (Alves and Lourenço, 2010; Dykstra et al., 2011; Sobiesiak et al., 2017; Cardona et al., 2020b; Jablonska et al., 2021). Although numerous geoscientists use the terms MTDs and MTCs interchangeably, we prefer the definition of MTCs as depositional architectural complexes comprised of several coeval or closely chronologically and genetically related MTDs (Alves and Lourenço, 2010; Pickering and Hiscott, 2015; Cardona et al., 2020a). This hierarchical classification is also helpful when distinguishing between MTC at the seismic scale (~50-200 ms two-way-traveltime (TWT) time thickness or >10 m thick) and those identified at outcrop, core, and borehole scale in so-called MTDs (<10 m thick). In addition, submarine MTCs can be further classified into attached or detached MTCs based on their relative source areas. Attached-MTCs are those sourced either from shelf or slope settings (i.e., shelf-attached or slope-attached MTCs), whereas detached-MTCs are sourced from isolated bathymetric highs (Moscardelli and Wood, 2008b; Ortiz-Karpf et al., 2018) (**Figure 2**). In general, attached-MTCs have areas over 100 km^2, and are approximately an order of magnitude broader than most detached MTCs (Moscardelli and Wood, 2016).

The planform and cross-section architectures of MTCs, which are typically imaged in seismic data, can be divided into three strain-dominated domains, from proximal to distal along dip-direction with respect to the sediment source; the headwall, the translational, and the toe domain (Lewis, 1971; Bull et al., 2009; Steventon et al., 2019) (**Figure 3**). Each domain is characterized by a locally dominant stress regime manifested in syn-depositional deformation structures (e.g., boudinage, folds, faults, pressure ridges, flow fabrics etc.). In general, the headwall domain of MTCs is dominated by extensional stress, manifested by the omnipresence of normal faults and extensional ridges (Martinsen and Bakken, 1990; Bull et al., 2009; Gamboa and Alves, 2016; Doughty-Jones et al., 2019). The translational domain is characterized by structures associated with longitudinal shear stress (Bull et al., 2009; Cardona et al., 2016; Safadi et al., 2017; Steventon et al., 2019). The toe domain is dominated by compressional stress caused by the arrest of the mass flow front, which creates a buttressing effect (Farrell, 1984; Frey-Martínez et al., 2006; Eng and Tsuji, 2019; Nugraha et al., 2020). When outcrops of MTDs are sufficiently exposed, it is possible to identify these key domains and their associated syn-depositional deformation structures (Alves and

Lourenço, 2010; Alves, 2015; Sharman et al., 2015; Le Goff et al., 2020; Cardona et al., 2020).

SEDIMENT REMOBILIZATION AS AN OVERARCHING PHYSICAL PROCESS

Sediment remobilization reflects a broad spectrum of phenomena, from soft-sediment instability near the sea floor to deeper, fluid-driven injection of sand and fluid usually related with the build-up of overpressures several 100s of metres below the seafloor. Sediment remobilization also records different scales and shows distinct areal distributions in sedimentary basins, from discrete features such as fluid pipes and chimneys to widespread fields of mud volcanoes and sand injection features (Milkov, 2000; Hurst et al., 2011). Close to the seafloor, MTCs and MTDs can be of different scales and, potentially, affect continental slopes for long periods of time. Sediment remobilization occurs on most continental margins and is recorded at outcrop in multiple regions of the world.

Several studies have focused on the geomorphological characterization of lithological and structural variations within MTDs using remote data (e.g., seismic, side-scan sonar), core and outcrop information with the purpose of understanding the process of mass failure and its controlling factors (Moscardelli et al., 2006; Frey-Martínez, 2010; Alves and Lourenço, 2010; Dykstra et al., 2011; Ogata et al., 2014; Moscardelli and Wood, 2016; Sobiesiak et al., 2017; Cardona et al., 2020a). The distribution, frequency and internal character of submarine landslides have revealed some key insights. According to Hühnerbach and Masson (2004), a series of landslide headscarps occur at a water depth of 1000–1300 m and the influence of slope gradient on landslide distribution is seemingly limited. However, Hühnerbach and Masson (2004) also recognized that the largest landslides occur in the gentler of continental slopes, where strata involved in the mass transport of sediment can affect broader areas. In parallel, Urgeles and Camerlenghi (2013) identified the presence of many small failures on active margins, proving at the same time that passive margins show fewer, but relatively larger landslides. More recently, Moscardelli and Wood (2016) have analysed the morphometry of several MTCs from different settings around the world. Morphometric parameters such as length, area, volume, and thickness of MTCs suggest that the geometry, geological setting, and causal mechanisms are to a variable degree linked and that predictive models can be applied in areas with incomplete, or low-quality, data.

Mass transport deposits consist of chaotic, convoluted strata resulting from meters to hundreds of meters of sediments being translated downslope, sometimes for hundreds of kilometers. In seismic data, these deposits are commonly composite bodies of blocky to highly disrupted, chaotic seismic facies with variable amplitude (Moscardelli and Wood, 2008a,b; Bull et al., 2009; Sawyer et al., 2009; Posamentier and Martinsen, 2011; Gamboa and Alves, 2015; Scarselli et al., 2016). They common geomorphic features and structures, most of which were generated during mass flows, that may allow an understanding of MTDs development. Many of these features can also be used as kinematic indicators (Woodcock, 1979; Farrell, 1984; Strachan, 2008; Bull et al., 2009). Ultimately, the identification of geomorphic features and structures within MTDs allows the definition of three main regions within these deposits: 1) a headwall region dominated by extension, which comprises a headwall scarp, extensional ridges, blocks, normal faults and boudins, 2) a translational region dominated by basal shearing and sediment downslope movement, where a transition from extensional deformation (or stretching) to compression occurs, and 3) a toe region dominated by compression, and marked by the development of folds and thrust systems in frontally confined landslides, or pressure ridges resulting from thrusts in frontally emergent/unconfined landslides (Martinsen and Bakken 1990; Frey-Martínez et al., 2006) (**Figure 3**).

The basal shear zones of MTDs document different styles of interaction between the material being remobilized and the substrate (Alves and Lourenço, 2010; Alves, 2015; Sobiesiak et al., 2018; Cardona et al., 2020). Mass transport deposits may also show some distinctive geomorphic features and structures, such as compressional and extensional features not restricted to their toe and headwall regions, respectively, as a result of the presence of blocks, substrate topography or complex soft sediment deformation processes (Strachan 2008; Alsop and Marco 2011; 2014). Finally, some blocks may travel beyond the edge of the toe region, the so-called outrunner blocks, to form basal shear surface striations (Nissen et al., 1999; Moscardelli et al., 2006; Kumar et al., 2021).

SEDIMENT REMOBILIZATION AS A GEOHAZARD IN SUBMARINE ENVIRONMENTS

Mass movements are commonly attributed to different triggering mechanisms, usually a combination of local and regional factors such as slope geometry and changes in slope gradient, evolving tectonic settings, local and far-field seismicity, high sedimentation rates, seafloor deformation associated with salt tectonics, pore-fluid overpressure, destabilization of gas hydrates, isostatic rebound, glacial-eustatic low-stands, climate change and rapid variations in sea level (Nisbet and Piper, 1998; McAdoo et al., 2000; Posamentier and Kolla, 2003; Sultan et al., 2004; Lee et al., 2007; Alves et al., 2009; Bertoni et al., 2013; Berton and Vesely, 2016). In addition, mass flow initiation and the distribution of associated deposits depend on changes in rheological properties, liquefaction, diagenesis, differential compaction and fluid expulsion (Bryn et al., 2005; Kvalstad et al., 2005; Locat et al., 2014). For the well-studied Storegga Slide, offshore Norway, the failure is considered to have been preconditioned by high pore-fluid pressure related to high sedimentation rates that followed glacial retreat, and was later triggered by an earthquake (and subsequent slope undercutting) on the lower continental slope in association with isostatic rebound (Haflidason et al., 2003; Kvalstad et al., 2005; Bellwald et al., 2019). A local control of strike-slip transport faults is also suggested for its northern flank, near the Modgunn Arch (Song et al., 2020).

Mass movement on continental slopes, volcanic islands or seamounts, is often damaging to infrastructure and life, with the added danger of being able to trigger tsunamis that may affect coastal populations (Nisbet and Piper, 1998; Masson et al., 2006; Paris et al., 2020). In the particular case of volcanic islands, their evolution is a result of periods of rapid volcanic-edifice growth, followed by the large-scale collapse of their flanks (Boulesteix et al., 2013; Hunt et al., 2013), often involving volumes of rock greater than 100 km^3 and comprising some of the largest mass movements in the world (Masson et al., 2002, 2008; Oehler et al., 2008). In the Canary Islands, NW Africa, the last 2 million years saw the onset of 11 different landslides that remobilized strata and rocks from different eruptive complexes (Masson et al., 2002; Boulesteix et al., 2013). These 11 landslides triggered tsunamis such as that associated with flank failure on the eastern coast of Tenerife (Güìmar and La Orotava mega-landslides), as proven by the accumulation of tsunami deposits on the Agaete Valley of Gran Canaria (Pérez-Torrado et al., 2006; Giachetti et al., 2011; Paris et al., 2018). Modeling studies have predicted the future collapse of the Cumbre Vieja volcano of La Palma as a single block with a volume of 500 km^3 and a thickness of 1400 m, but recording different amplitudes and impact in coastal areas. Models have shown that the ensuing tsunami would mostly affect near-field areas of the Canary Islands and Northwest Africa, potentially inundating the Atlantic coastline of the United States of America and Western Europe in a worst-case scenario (Ward and Day 2001; Mader 2001; Gisler et al., 2006; Lovholt et al., 2008; Abadi et al., 2012; Tehranirad et al., 2015). As of the final compilation of this Chapter (October 2021), the Cumbra Vieja volcano is erupting and feeding large volumes of lava to the SW flank of La Palma. Large-volume landslides resulting from flank collapses of ocean island volcanoes are thus considered one of the main causes of mega-tsunamis (Paris et al., 2018; 2020), but catastrophic tsunami waves can also be trigged by relatively small subaqueous landslides such as that of Anak Krakatau in Indonesia (September 2018). This submarine landslide remobilized a volume of 0.22-0.3 km^3 (Grilli et al., 2019; Zengaffinen et al., 2020) and generated a tsunami with a height approaching 13 m, resulting in the loss of more than 400 lives (Muhari et al., 2019).

SEDIMENT REMOBILIZATION DUE TO FLUID FLOW AND SUB-SURFACE OVERPRESSURE

Sediment remobilization is also considered a geohazard when associated with subsurface fluid flow, as the sudden release of overpressured fluid may jeopardize offshore drilling sites, their associated infrastructure, new CO_2 sequestration storage sites, and even structures for geothermal, wind and solar energy production (Roelofse et al., 2020). In parallel, characterising and dating fluid flow and structures associated with mass wasting can provide information concerning past events of fluid migration in a sedimentary basin. It also contributes to a better characterization of the magmatic processes leading to escape of heat and hydrothermal fluids from deeper parts of the crust.

Mud volcanoes are a category of fluid vent structures (**Figure 4A**) formed in sedimentary basins as the surface expression of hydrocarbon migration. This results in the extrusion of a three-phase mixture of solids and fluids (fine-grained solid phase derived from underlying sediments and at least two fluid phases, water and gas - mainly methane, and occasional liquid hydrocarbons; Kopf et al., 2001; Dimitrov, 2002; Levin, 2005; Judd and Hovland, 2009; Etiope, 2015; Mazzini and Etiope, 2017). They are the surface expression of subsurface processes characterized by movements of large masses of sediments and fluids, such as diapirs, diatremes, domes, dewatering pipes, mud intrusions, mud mounds, chimneys and pipes (Kopf, 2002; Skinner and Mazzini, 2009; Mazzini and Etiope, 2017). The mixture of solids and fluids is commonly sourced from depths of several kilometers (Stewart and Davies, 2006; Kirkham, 2015; Blouin et al., 2019).

Mud volcanoes occur on tectonically active margins (e.g. compressional zones of accretionary complexes, fold-and-thrust belts), passive margins, deep sedimentary basins related to active plate boundaries, as well as delta regions and areas with important salt diapirism (Milkov, 2000; Kopf, 2002; Etiope, 2015; Mazzini and Etiope, 2017). They are located in petroliferous basins, both offshore (Black Sea, Gulf of Cadiz, Caspian Sea, Mediterranean Sea, Gulf of Mexico, Indian Ocean, Caribbean Sea, Norwegian Sea, Atlantic Ocean, Pacific Ocean, China Sea) and onshore in countries as Colombia, Azerbaijan, Papua New Guinea, Japan, Romania (see Mazzini and Etiope, 2017 and references herein), along anticline axes, strike slip faults, normal faults and fault-related folds.

Fluid vents vary significantly in size and geometry depending on the fluid rheology and source, and eruption processes and subsequent erosion (Kopf, 2002; Murton and Biggs, 2003; Mazzini and Etiope, 2017). They may display various morphologies such as conical, elongated, pie-shaped, multicrater, growing diapir-like, stiff neck, swamp-like, plateau-like, impact crater-like, subsiding structure, subsiding flanks and sink-hole type (Roelofse et al., 2020) (**Figure 4B**). One common morphology is that of subcircular hills, classified as mud cones (slope of the flanks $> 5°$) and mud pies (slope $< 5°$) (Kopf, 2002).

Mud volcanoes are usually composed of a group of cones and crater systems (Mazzini and Etiope, 2017). Mud volcanoes may display areal extension ranging from the order of a square meter up to several square kilometers, a width of 4 km onshore and up to 12 km offshore, and a height of a few centimeters to hundreds of meters (Yusifov and Rabinowitz, 2004; Orange et al., 2009; Mazzini and Etiope, 2017) (**Figure 5**). The migration of fluid and mud is mainly driven by a combination of gravity driven instability of shales and fluid overpressure build-up in shales, reservoir rocks or fractures, followed by the hydrofracturing of impermeable barriers (Kopf, 2002; Revil, 2002; Mazzini and Etiope, 2017). Fluid overpressure may be caused by fast rates of sediment deposition (Judd and Hovland, 2007; Wu et al., 2019), tectonic subduction and compression (Conrad et al., 2018), seismic-induced shock and gas buoyancy (Kopf et al., 2001).

Overpressure in shales may result in volumetric expansion due to generation of hydrocarbons and other additional mechanisms such as the thermal effect in pore fluids (as temperature gradient increases), dehydration reactions (e.g., illitization of clay minerals), disequilibrium compaction, related to lithostatic loading or compressive tectonic stresses, and pressure dissipation by fluid flow (Revil, 2002; Mazzini and Etiope, 2017). In contrast, gravity driven instability generally occurs due to rapid sedimentation in subsiding basins and blanketing of low density clay-bearing strata, which can be buoyant in surrounding units (Mazzini and Etiope, 2017). Intragranular overpressure also tends to increase by mechanical compaction during the gradual burial of clays, or during sudden depositional events (slides, slumps, thick turbidite deposits) associated with high rates of sedimentation and subsidence. Rapid subsidence of porous sediments rich in water and organic matter, and the subsequent thermal maturation of hydrocarbons during early diagenesis, also produce fluid-mud mixtures that migrate upward under high pressures (Dimitrov, 2002; Milkov, 2000; Kopf, 2002; Mazzini and Etiope, 2017). Hydrofracturing may result from this processe and also by increases in fluid pressure, tectonic stresses, fault reactivation and seismicity (Mazzini and Etiope, 2017).

Sand injections can occur as dykes, sills, conical and saucer-shaped intrusions with wings (**Figure 6**), and are usually identified as discordant, high-amplitude anomalies on seismic profiles (Hurst et al., 2005; Huuse et al., 2007; Cartwright et al., 2008; Hurst et al., 2011 Andresen and Clausen 2014) (**Figure 7**). According to Hurst et al. (2011), the injection of sand into overburden units requires fluid overpressure as a precondition, initiating hydrofractures and driving the subsequent fluid flow. The development of sand injectites results from fluid overpressuring (usually the generation of excess water and, sometimes, hydrocarbons), the hydrofracturing of sealing strata, liquefaction, fluidization and the injection of sand (Jolly and Lonergan, 2002; Duranti and Hurst, 2004; Vigorito and Hurst, 2010; Hurst et al., 2011). Different triggering mechanisms are associated with the formation of sand injectites: i) local earthquakes resulting in sand liquefaction (Obermeier, 1996; 1998; Rosseti, 1999; Boehm and Moore, 2002; Obermeier et al., 2005); ii) overpressure caused by rapid loading and good seal integrity (Truswell, 1972; Allen, 1985; Strachan, 2002; Hildebrandt and Egenhoff, 2007); iii) thermal pressurization (Ujiie et al., 2007); and, iv) fluid migration causing increased overpressure (Lonergan et al., 2000; Davies et al., 2006).

Seismicity and rapid loading (by submarine landslides or sediment derived from storm waves) are considered the most typical triggering mechanisms for sand injection and extrusion (Truswell, 1972; Strachan, 2002; Jonk et al., 2007; Jonk, 2010; Obermeier, 1996; Obermeier et al., 2005 Boehm and Moore, 2002; Hildebrandt and Egenhoff, 2007), though seismicity is unlikely to act alone considering the energy required to fluidize and inject the 10's of km^3 of sand (Huuse et al., 2005; Duranti, 2007; Szarawarska, 2009; Vetel and Cartwright, 2009; Vigorito and Hurst, 2010). The overpressure caused by the rapid migration of fluid into depositional sand bodies can be related to: i) the formation of polygonal faults in mudstones (Cartwright and Dewhurst, 1998; Cartwright et al., 2003; Wattrus et al., 2003); ii) mineralogical phase changes (Davies et al., 2006); iii) the rapid migration of hydrocarbon gas

(Brooke et al., 1995); and iv) the decomposition of gas hydrates during periods of eustatic sealevel change or ocean warming (Hurst et al., 2011). Importantly, the migration of fluids from deep sedimentary sources is one of the factors responsible for the development of large-scale sand injectites - some capable of crosscutting more than 200 m of fine-grained strata (Hurst et al., 2003b, 2011; Huuse et al., 2005).

The North Sea giant sand injectite province was the first where subsurface sand injectites, up to several 100 of meters high and 1000 of meters wide, where recognized in the literature and proven in wells and seismic data (Lonergan and Cartwright, 1999; Huuse and Mickelson, 2004; Huuse et al., 2005; Cartwright et al., 2007; Hurst and Cartwright, 2007a; Huuse et al., 2007; Shoulders et al., 2007; Andresen and Clausen 2014). The recent study of Andresen and Clausen (2014) described injectites from this province as comprising geometries ranging from basal sills with wings to V-shaped and conical injectites 300 to 3700 m in width and up to 150 m in height. The formation of these injectites was due to overpressure caused by rapid differential loading during the Oligocene, combined with a possible influx of fluids from underlying Paleozoic half-grabens. The authors suggested the Upper Paleocene sand within the Lista Formation as the source sand for the injectites, which are connected with the top of these formation by potential feeder conduits.

For the sand injectites in the Tertiary petroleum reservoirs of the northern North Sea, suggested trigger mechanisms include seismicity, rapid loading and fluid migration (Lonergan et al., 2000; Jolly and Lonergan, 2002; Duranti and Hurst, 2004; Huuse et al., 2004). In the south Viking Graben, injectites consist of dikes (discordant to bedding) and sills (concordant to bedding), with thicknesses ranging from subcentimeter to meter scale, and commonly associated with injection breccias (up to 10-m thick), sand-supported with mud-clasts (Jonk et al., 2005). Sand injection was possibly triggered by earthquake activity and may have been facilitated by petroleum fluids (Huuse et al., 2004; Jonk et al., 2005).

Sand injectites that comprise significant hydrocarbon reservoirs also occur in the Paleogene section of the northern North Sea (Dixon et al., 1995; Lonergan et al., 2000; Hurst et al., 2003a). Large-scale tabular dykes associated with extrusions (subhorizontal extensions) occur along the margins of the Nauchlan Member (Late Eocene Alba Formation), which comprises a deep-water channel fill extensively modified by post-depositional sand remobilization and injection that terminates at the Eocene–Oligocene unconformity (Duranti and Hurt, 2004) (**Figure 7D**). These injectites resulted from a sudden increase in the ratio of overpressure to confining pressure, possibly caused by static liquefaction and enhanced by hydrocarbon gas (Duranti and Hurt, 2004). Fluid overpressure and associated hydraulic fracturing resulted in the severe disruption of adjacent mudstones, as proven by the fragments of mudstone that were incorporated into the injectites. According to Duranti and Hurst (2004), two main phases of sand injection occurred at different burial depths: the first was a shallow burial phase (below 100 m) that produced thin folded dykes and sills, while the second phase - with injectites at the boundary between the Eocene and Oligocene - was deeper (about 300m burial depth), more voluminous and formed large-scale tabular wing-like dykes that project from the edges of the channel fill. Numerous sharp-sided, thick dykes and sills were also formed (Duranti and Hurt, 2004).

In central California, at least three sand injection complexes have been the subject of several recent studies: a) the Panoche Giant Injection Complex (**Figure 7A**; Vigorito et al., 2008; Vigorito and Hurst 2010; Scott et al., 2013; Palladino et al., 2018), b) the Tumey Giant Injection Complex (**Figures 6A and 7B**; Huuse et al., 2007; Zvirtes et al., 2019; 2020), and c) the Santa Cruz Injection Complex (**Figure 6B-E**; Boehm and Moore 2002; Thompson et al., 2007; Scott et al., 2009; Palladino et al., 2020). The Panoche Giant Injection Complex (PGIC) comprises a well-defined system of sand dikes and sills intruded within the Upper Cretaceous to Paleocene Moreno Formation (Vigorito and Hurst 2010). Different architectural elements are present in the PGIC, from its base to its top, such as parent units, intrusive bodies and extrudites (Vigorito et al., 2008; Hurst et al., 2011; Scott et al., 2013). In the PGIC, parent units consist of turbiditic channel-complexes and isolated sandstone channels, which occur in the lower part of the Moreno Formation (Vigorito et al., 2008). Injectites correspond to interconnected single or multi-layered sills and dikes with a thickness ranging from centimeters to meters, while extrudites are mound-like sand bodies located in the upper part of the Moreno Formation (Vigorito and Hurst, 2010). These extrudites are composed of fine- to medium-grained sands and link to the underlying intrusive complex via isolated dikes. According to Vigorito and Hurst (2010), the PGIC was the result of a large-scale overpressure event that occurred in the Lower Paleocene, involving an area of at least 1500 km^2. At the base of the injection complex, the estimated pore-fluid pressures likely reached 22.26 to 25.08 MPa, or 0.81 and 0.95 of lithostatic pressure (Vigorito and Hurst, 2010). A diachronous timing for sand injection, combined with fluid pressure in excess of the lithostatic load pressure within the source units that was, were also suggested by Vétel and Cartwright (2010) based on the analysis of cross-cutting relationships in the field. These authors recognised that the opening of the sand intrusions did not obey a systematic sense of movement, a character resulting from the presence of short-range mechanical interactions between adjacent sills and dikes.

Two different families of sandstone-filled normal faults occur in the lower portion of the Moreno Formation and, particularly, at the top of PGIC (Palladino et al 2018). The first normal-fault family resulted from the rapid increase of pore-fluid pressure in poorly-consolidated sandstones, with associated hydraulic failure of the overlying host strata, i.e. pressure build-up and overburden collapse extension. The second family resulted from regional extensional and related draining of fluidized sand towards active tectonic structures.

The Tumey Giant Injection Complex (TGIC) is composed of a network of dikes and sills emplaced in an interval ca. 450 m-thick in the so-called Kreyenhagen Shales (Middle to Upper Eocene; Huuse et al., 2007; Zvirtes et al., 2019). According to Zvirtes et al. (2020), the parent units of the TGIC are the turbiditic channels of the Kreyenhagen Formation, lacking a contribution from the underlying Lodo and Domengine formations. When considering its stratigraphic and structural relationships, the TGIC consists of lower and upper intrusive intervals, (Zvirtes et al., 2019). The lower intrusive interval comprises a sill complex with a stepped, staggered and multi-layered geometry connected by narrow, short low- and high-angle dykes with planar and irregular geometry. The upper intrusive interval is a network of interconnected sills, dykes, irregular intrusive bodies and injection breccias, which show several intrusive shapes. These range from sheet-like intrusions with planar margins to highly irregular, bulbous and curved margins to asymmetric saucer-shaped intrusions with large wings emanating from the channelized turbidites (parent units; Zvirtes et al., 2019) (**Figures 6A and 7E-G**).

As the TGIC intrudes the Lower-Middle Eocene Kreyenhagen Shale, but does not affect the overlaying Miocene Temblor Formation, the timing of sand injection must have occurred between the Middle Eocene and the Miocene (Palladino et al., 2018). In the Kreyenhagen Shale were identified sandstone-filled normal faults associated with pressure build-up with overburden collapse extension (Palladino et al., 2018), and sandstone-filled contractional structures related to regional contractional tectonics (Palladino et al., 2016).

The Santa Cruz Injection Complex (SCIC) corresponds to a network of partially tar-saturated and unsaturated injectites emplaced in the Santa Cruz Mudstone (Thompson et al., 1999; Scott et al., 2009). Four different architectural elements occur in the SCIC, including parent units, injectites, extrudites and sandstone-filled faults (Palladino et al., 2020). The parent unit is commonly identified as the Santa Margarita Sandstone (Boehm and Moore

2002; Thompson et al., 2007); however, some studies indicate multiple parent sandstones based on mineralogical data (Clark 1981; Scott et al., 2009). The injectites consist of a well-developed intrusive network that includes single or swarms of dikes, water and tar saturated, occasional sills and locally preserved saucer-shaped intrusions (Palladino et al., 2020) (**Figure 6B-E**). The thicknesses of individual injectites generally ranges from a few centimeters to a decimeter. Yet, some isolated dikes or sills are up to a few meters wide and the Yellowbank/Panther beach sill is, at least, 15 m thick (Thompson et al., 1999; Scott et al., 2009). Sandstone-filled faults are sand injections emplaced directly along tectonic structures, predominantly normal faults and less common strike-slip and compressional fault planes (Palladino et al., 2020). Extruded sands occur as multiple, laterally discontinuous tar-saturated mounds emplaced in different stratigraphic levels of the Santa Cruz Mudstone (Boehm and Moore 2002; Hurst et al., 2006; Palladino et al., 2020). They span hundreds of meters, are several meters thick and, locally, the original structure of sand volcanoes shows multiple conduits and laminated flanks (Palladino et al., 2020).

The age of emplacement of the SCIC is constrained to the Late Miocene (7–9 Ma), as extrudites occur within the Santa Cruz Mudstone (Palladino et al., 2020). However, two distinct sand injection phases are identified (Palladino et al., 2020). The first phase (Late Miocene) resulted in large volumes of sand emplaced within the top-seal units and controlled by compaction and compressional tectonic processes. This phase was followed by hydrocarbon accumulation within newly injected sandstones. The second phase is related to a series of brittle tectonic events associated with the San Andreas/San Gregorio Fault System, which promoted the remobilization and accumulation of sand along newly formed fault planes, mostly high-angle extensional faults. As a result of this brittle deformation, the top seal was breached and previously accumulated hydrocarbons were leaked. The age of this phase still uncertain but ranges between the Late Miocene to Quaternary (Palladino et al., 2020).

ECONOMIC AND SOCIETAL RELEVANCE OF SEDIMENT-REMOBILIZATION PROCESSES

Processes of sediment-remobilization in deep-water settings, such as submarine landslides, turbidity currents, and sub-surface fluid flow and seafloor expulsion (Clare et al., 2017), can have societal, economic and ecological impacts (Talling et al., 2014). Submarine landslides may affect marine biological communities due to the disturbance and modification of seafloor ecology during their emplacement, or by acting as habitat hotspots on their scars and remobilized elements (De Mol et al., 2009). This process is also considered a mechanism for the dispersion of species between isolated islands, so influencing local evolution (Caujapé-Castells et al., 2017).

The economic impact of submarine landslides is related to damage of strategically important seafloor infrastructure including telecommunication cables, production platforms and hydrocarbon pipelines caused by these processes (Piper et al., 1999; Shipp et al., 2004; Mosher et al., 2010b; Thomas et al., 2010; Carter et al., 2014; Forsberg et al., 2016; Pope et al., 2017). The repair of cables and subsea infrastructure networks may cost hundreds of millions of dollars, while the subsequent interruption of global communication, global financial trading, and global supply chains, can potentially be immense as trillions of dollars are traded per day on this network (Carter et al., 2009; 2014). In parallel, damage to seafloor hydrocarbon infrastructure (platforms and pipelines) can result in production delays and marine environment contamination due to uncontrolled losses of hydrocarbons (Kaiser et al., 2009; Skogdalen and Vinnem 2012). The cost of damage to hydrocarbon pipelines due to submarine instability processes is estimated in more than $400 million per year (Mosher et al., 2010).

Submarine landslides may also cause tsunamis, such as the 3000 km^3 Storegga Slide that occurred offshore Norway at ~8.2 ka b.p. (Talling et al., 2014). Tsunamis comprise a threat to many a coastal community and may result in large numbers of fatalities (Tappin et al., 2001; Ward 2001; Harbitz et al., 2014). Even small submarine landslides (i.e., less than 0.1 km^3) can be dangerous, causing tsunami waves as high as tens of meters (Bohannon and Gardner, 2004; Von Huene et al., 2004) and landward flooding (retrogression) leading to loss of life (Vardy et al., 2012). The destruction potential of such events has been associated with the volume, vertical displacement, water depth and velocity of the remobilized sediments (McAdoo and Watts, 2004; Álvarez-Gómez et al., 2011; Schnyder et al., 2016).

Hazard assessments for possible future tsunamis triggered by landslides have been a concern among researchers and non-scientists throughout the world (Paris et al., 2020). Based on identification of landslide populations and their morphology, numerical simulations can help estimate the impact of past-tsunamis resulting from landslides and areas affected by such events (Gianchetti et al., 2011; Lovholt et al., 2015; Yavari-Ramshe and Ataie-Ashtiani 2016). Future large-scale landslides and ensuing tsunamis, such as the tsunami predicted for future flank collapse of the Cumbre Vieja volcano in the Canary Islands (Ward and Day 2001; Tehranirad et al., 2015), can only be characterised using a combined geophysical, geological and modeling approach. Climate change is another issue that makes risk assessments for landslide-tsunamis relevant in the short to long term; paleoclimatic changes and eustatic variations have being identified as major factors triggering instability factors on some continental margins (McMurtry et al., 2004; Quidelleur et al., 2008; Boulesteix et al., 2013; Berton and Vesely 2016).

Economically speaking, submarine landslides can generate thick, extensive mass transport deposits, playing an important role as seal or reservoir intervals in deepwater petroleum systems (Moscardelli and Wood 2008b; Gamberi et al., 2011; Posamentier and Martinsen 2011; Alves et al., 2014). Mass transport deposits associated with turbidites have been identified as comprising some of the world's largest oil and gas fields (Barley, 1999; Eyrton 2005). In terms of their sedimentological character, mass transport deposits cover a wide range of depositional facies, from MTDs with a highly mud content (i.e., remobilized slope muds) to complex deposits with interconnected and interfingering sand intervals, i.e., slumped levees or channel bodies. Consequently, MTDs may act as competent barriers to fluid flow (top seals or intra-reservoir barriers and baffles) or, instead, reservoirs and conduits to fluid flow (Shultz 2004; Dykstra et al., 2011). The impact of submarine landslides in petroleum systems is also related to the distribution of stratigraphic traps on the slope as a result of seafloor remobilization, the geometry of facies developed within mass transport deposits and the morphology of these deposits, in which local lows are, usually, controlled by their internal structure (Kneller et al., 2016). Reservoir geometry can be influenced by the different slumps, slides and debris flows domains identified in submarine landslides, as these flow processes usually lead to discontinuous and compartmentalized sand reservoirs (Shanmugam et aI. 1995). In turn, turbidity currents generally form continuous, sheet-like sand bodies, with the caveat that, where mass transport deposits are present, or in areas of slide scars, turbidite systems location, nature, and geometry may vary widely (Brami et al., 2000; Armitage et al., 2009; Kneller et al., 2016).

Fluid flowing in buried MTDs, and its eventual expulsion onto the seafloor, may constitute a hazard in multiple settings. Sediment remobilization resulting in mud volcanoes and sand extrusion due to fluid flow and sub-surface overpressure may also impact sub-sea infrastructures, such telecommunication cables, production platforms and hydrocarbon pipelines (Lupi et al., 2013; Kilb 2008). Sediment injection and/or free gas in the sub-surface may result in slope instability once they modify sediment shear strength, compressibility, and effective stress (Chillarige et al., 1997; Evans 2010; Riboulot et al., 2013). Mud volcanoes represent geohazards due to the potentially violent release of large amounts of hydrocarbons and mud, the degradation of sediments at seafloor and quicksand effect, and episodic dissociation of submarine gas hydrates (Mazzini and Etiope 2017). They are also one of the geological sources of methane that are currently considered a major contributor to the atmospheric methane budget (Etiope, 2015). At shallow depths, the presence of gas may result in gas kicks and blowouts while drilling, subsidence and leaks outside casing, and issues with cementing wells (Nimblett et al., 2005). Natural seepage of fluids at the seafloor may be associated with sediment remobilization at depth, such as eruptive mud volcanoes with associated caldera collapses (Gray et al., 2013), and sand extrusions related to sand liquefaction, fluidization and injection (Hurst et al., 2011). The expulsion of fluids on the seafloor can create corrosive pore fluids and locally modify seafloor geotechnical properties (Thomas et al., 2011); hence, it can lead to problems for pipeline design, particularly where seeps occur in high spatial densities (Gafeira, et al., 2012; Moss et al., 2012).

Sand injectites can influence traps, reservoirs, seals, and fluid migration in sedimentary basins (MacLeod et al., 1999; Duranti et al., 2002; Hurst and Cartwright, 2007b). They may affect the distribution and geometry of hydrocarbon reservoirs, connect otherwise isolated sand bodies to form possible hydrocarbon migration routes and thief zones (Hurst and Cartwright, 2007; Satur and Hurst 2007). Therefore, sand injectites may impact hydrocarbon plumbing systems and represent potential drilling hazards (Hurst and Cartwright, 2007b; Andresen and Clausen 2014). Mud volcanoes are common in several petroleum provinces worldwide, including major hydrocarbon exploration and production regions (e.g., the North Sea, the Caspian Sea, the Gulf of Mexico, the Black Sea, the Sea of Okhotsk, the Sea of

Japan) and often related to modern (Mazzini and Etiope 2017; Cortes et al., 2018). These geological features consist of ideal targets for hydrocarbon exploration, as they indicate the existence of relevant subsurface reservoirs (Mazzini and Etiope 2017).

OUTCROP EXAMPLES FROM KEY ANALOGUES: CRETE, NEW ZEALAND AND PARANÁ

Fault-bounded slopes in SE Crete

Slope deformation styles in SE Crete include the presence of mass transport deposits with distinct lithologies reflecting a marked contrast between remobilized mass-wasting deposits and 'background' slope deposits. Hence, it is relatively straight-forward to distinguish not only the source areas of mass transport deposits on Crete, but also their exact geometries when exposed in the field (**Figure 8**). Specific structures are associated with the largest mass transport deposits: a) recumbent folds of ductile material are common in areas where the slopes were tectonically oversteepened, or where sliding strata were buttressed in a locally emergent configuration sensu Frey-Martinez et al. (2006), b) bed-parallel shearing occurs sporadically as small, localized slope-instability features, c) rolling of larger blocks under breccia-conglomerate carpets, d) sliding of large carbonate blocks occurs over siliciclastic slope strata, and e) moderate sliding of carbonate blocks and siliciclastic volumes of rock (slumps) is observed over detachment faults.

Figure 9 shows, as an outcrop example, a Late Miocene slide block transported over siliciclastic turbidites on the paleoslope of SE Crete. The area in question comprises autochthonous carbonate fan cones and boulder conglomerates, with slide blocks proving the widespread collapse of fault-bounded slopes during the Miocene (**Figure 8**). Slide blocks reflecting large-distance transport are scattered throughout the mid to lower paleoslopes of SE Crete. Slide blocks occur mainly over the Parathiri Member and Kalamavka Formation (see Alves and Lourenço, 2010). Their size varies from 10 to 100 m, with individual blocks >100 m long occurring in particular parts of the paleoslope (**Figure 8**).

Other silicilastic MTDs are common towards the most distal parts of SE Crete's paleoslope, where carbonate blocks were sparser and debris-flows dominated instability processes (**Figures 8 and 9**). Here, scarce polymictic breccia-conglomerates give rise to siliciclastic debrites with minor presence of cm-size blocks. Basal contacts are commonly erosional below individual blocks and slope strata, and also in debrites/siliciclastic MTDs. In fact, basal contacts comprise dictinct lithologies and structures. Alves and Lourenço (2010) have shown that polymictic breccia–conglomerates and siliciclastic (sandy to conglomeratic) blocks are often embedded within a debris-flow matrix below the largest blocks. In **Figure 9** is shown an example of one of such limestone slide blocks under which a basal polymictic breccia changes into an area of siliciclastic slope sediment that was also deformed by the movement of the block. Below the first 1–2 m of basal strata, in which the polymictic breccia is observed, the basal slip plane is formed by contorted fragments of strata (sandy to silty) embedded in a clayey matrix (Fig. 8b). Below other blocks, sheath folds are visible and often intercalated with more chaotic strata comprising sandy and silty material injected during the basal deformation event.

A series of structural features appear on SE Crete's paleoslope, from shear structures at the basal shear zone of MTDs and blocks, to bookshelf sliding ans micro-structural features indicating sediment shearing and local slope collapse (**Figures 11 and 12**). **Figure 12** shows S-C fabrics, foliation and pinch-and-swell structures are observed below a 40-m tall slide block. In particular, S-C fabrics and pinch-and-swell structures are diagnostic of the direction of movement of MTDs and slide blocks (see Alves, 2015).

Comparisons between statistical data from slide blocks (and MTDs) in SE Crete and high-resolution seismic data from 60 published case studies have been presented in Alves and Lourenço (2010) as an attempt to understand the scale relationship between the thickness of failed megablocks and the corresponding thickness of deformed basal strata. In **Figure 13** are shown key graphs illustrating the thickness of failed strata vs. thickness of basal shear surfaces, as published in Alves and Lourenço (2010). Of importance in these graphs is the apparent scale discrepancy among the seismic data and outcrop examples studied by the authors - the difference between the average thickness of basal shear surfaces recorded in geophysical data (12.8 m on average, reaching a maximum of 65 m), and the thickness observed in SE Crete (3.1 m on average) is clear on the graphs. Nevertheless, both the submerged and outcropping examples show failed strata to be 2.0 to 20 times thicker than the underlying basal shear surface, a value further investigated in Alves (2015), who demonstrated that the ratio between the thickness of failed deposits and the corresponding thickness of deformed strata at the base of the blocks (R) is usually in the order of $5 < R < 10$. Average ratios between failed strata and their corresponding basal shear surfaces reach 5:1 for the outcropping examples from SE Crete and just above 9:1 for documented examples from offshore landslides (**Figure 13**). Such threshold values are important as the thickness of seismically imaged basal shear zones is often not resolved on industry seismic data; the ratio R can thus be used to predict the thickness of such deformed basal shear zones.

The Rapanui MTD outcrop, Miocene Mount Messenger Formation, Taranaki Basin (New Zealand)

The outcrops of the Rapanui MTD (RMTD) are dominated by soft-sediment deformation associated with submarine mass flows (**Figure 14**). The RMTD is sandwiched between two sandstone units (Lobe 1 and Lobe 2) interpreted as submarine fan lobes by Masalimova et al. (2016) and Do (2018). Based on sedimentary structures, slide blocks, matrix disruption and deformation features, three domains in the RMTD were identified: headwall (**Figure 15**), translational (**Figure 16**) and toe domains (**Figure 17**). The thickness of the RMTD varies spatially from 4 m near the headwall, to at least ca 15 m in the toe, reflecting a thickness inflation of about 27%. The average thickness is 7.4 m and the RMTD maintains this value through the translational domain. Although the true dimensions of outcropping MTDs are generally unknown (Martinsen, 1989), the length of the RMTD can be estimated as approximately 10 km using the average deposit thickness (see Moscardelli and Wood, 2015, for methodology).

The headwall domain of the RMTD is not fully exposed but does make up approximately 15% of the outcrop extent. Where this domain is exposed, the RMTD has an average thickness of 4 m and is dominated by structures reflective of extensional strain, for example, boudinage, fractures and clastic injectites (**Figure 15**). Slide blocks are scarce in the headwall domain. The original bedding of the RMTD protolith can still be recognized and is comprised of thinly-interbedded sandstones with siltstones and mudstones (**Figure 15B and D**). The syndepositional intrafolial folds in the headwall (n = 11) have orientations from upright to recumbent and their interlimb angles are predominantly close (30 to 70°). Furthermore, the headwall is devoid of isoclinal-shaped and ptygmatic-shaped folds, and open-shaped folds (interlimb angle between 70°and 120°) were only documented in this domain.

The deformation structures described in the headwall are confined within the RMTD and the interaction between the RMTD and the underlying deposits is minor. The translational domain in the RMTD has an average thickness of 7.4 m and comprises 60% of the outcrop extent. The transition into this domain can be identified by conspicuous stratal disruption and homogenization of the RMTD matrix (Ogata et al., 2012). In this domain, nearly all the original bedding/stratification from the RMTD protolith has been obliterated (**Figure 16**). Flow folds or flowage fabric are also pervasive in this domain. Brodzikowski and Van Loon (1985) defined flow structures as those resulting from partial or complete deformation via fluidization (viscoplastic nature) without tectonic influence. Syndepositional folds (n = 35) are common in this domain and are primarily moderately inclined to recumbent tight-shaped folds with average interlimb angle of 16°. No open-shaped folds were identified in this domain. Folds become rootless up-section in the RMTD and decrease in number. The described structures are characteristic of low-viscosity Bingham flow deposits (Tripsanas et al., 2008).

The toe domain exhibits the greatest thickness in the RMTD reaching at least 15 m, even though its upper contact is truncated here by the Early Holocene Rapanui wave cut surface. The extent of this domain is estimated to be around 25% of the RMTD exposure. The largest megablock (ca 35 m width) in the RMTD is located in the toe (**Figure 14C**). The RMTD matrix in the toe is substantially enriched in fine to medium-sand fraction in comparison with the other domains (samples S 8, S 9 and S 10 in **Figure 2B**). Similar to the translational domain, syndepositional folds are abundant in the toe (n = 33) and openshaped folds are absent. Most folds in this domain are moderately inclined to recumbent tight-shaped folds with an average interlimb angle of 17°. The dominant deformation structures in the toe are associated with a compressional stress regime such as metre-scale sheath-like folds of sandstone beds (**Figure 17B and D**). These metre-scale folds are associated with pressure ridges (Frey-Martınez et al., 2006; Bull et al., 2009) and high shear strains (Farrell, 1984; Bradley and Hanson, 1998). Additionally, the mud-rich portions surrounding some folds show a weak crenulation texture formed in response to folding (Fossen, 2016) (**Figure 17B**).

Outcrop analogues from the Itararé group, Paraná Basin (Southern Brazil)

MTDs have been identified along all the stratigraphic section and area of exposure of the Itararé Group (Gama Jr. et al., 1992; Eyles et al., 1993; Carneiro and Costa 2006; Vesely and Assine 2006; d'Ávila 2009; Suss et al., 2014; Carvalho and Vesely 2017; Valdez-Buso et al., 2019; Mottin et al., 2018; Vesely et al., 2018; Schemiko et al., 2019; Rodrigues et al., 2020; 2021). The full extent and thickness of a single MTD is usually difficult to assess due to the limited exposure of the Itararé Group. The thickness of the some MTDs generally ranges from about 5 m to 10s of meters (Carvalho and Vesely 2017; Mottin et al., 2018; Schemiko et al., 2019). When the boundaries between MTD and non-MTD strata are exposed, they show sharp aspects, with the base of MTDs being commonly erosive and irregular. The top surface of MTDs is usually flat but low amplitude relief has been described locally, on which fine-grained facies may be ponded (Vesely et al., 2018).

Although the Itararé Group presents penecontemporaneous deformation associated with glaciotectonics (Aquino et al., 2016; Rosa et al., 2019; Ferdochuk et al., 2019), most deformation structures described in this group resulted from subaqueous mass movements associated with turbiditic deposits, with or without a definite record of glacial influence (Salamuni et al., 1966; Schneider et al., 1974; França and Potter 1991; Gama Jr. et al., 1992; Eyles et al., 1993; Vesely et al., 2005; Carneiro and Costa 2006; Vesely and Assine 2006; d'Ávila 2009; Suss et al., 2014; Carvalho and Vesely 2017; Valdez-Buso et al., 2019; Mottin et al., 2018; Vesely et al., 2018; Schemiko et al., 2019; Rodrigues et al., 2020). Several structures have been identified within these MTDs, such as folds, faults, boudins, shear features (as quarter-like structures, sheared lamination, etc.), plus deformation at the borders of intrabasinal clasts in diamictites, injectites, and others (Vesely and Assine 2006; Suss et al., 2014; Carvalho and Vesely 2017; Valdez-Buso et al., 2019; Mottin et al., 2018; Vesely et al., 2018; Schemiko et al., 2019; Rodrigues et al., 2020; 2021).

The MTDs of the Itararé Group consist mostly of: 1) large allochthonous intrabasinal clasts (IC) of sandstones, rhythmites and mudstones; 2) deformed sandstone, rhythmite and shale; and 3) heterogeneous (banded matrix) to homogeneous (massive matrix) sandy-muddy diamictites with dispersed granules to boulders of intrabasinal clasts (sandstones, shale, rhythmites and plant fragments) and extrabasinal clasts (granites and metamorphics), with some striated and faceted. Heterogeneous diamictite corresponds to pebbly-sandy-mudstone containing disrupted fragments of deformed strata in which the original bedding is still preserved (Vesely and Assine 2006; Suss et al., 2014; Carvalho and Vesely 2017; Valdez-Buso et al., 2019; Mottin et al., 2018; Vesely et al., 2018; Schemiko et al., 2019; Rodrigues et al., 2020; 2021). Based on the degree of deformation, disaggregation and mixing of sediments of the remobilized layers, MTDs have been described as slides, slumps and debris flows, or a transition between all these mass-movement deposits in all three stratigraphic units of the Itararé Group (Vesely and Assine 2006; Suss et al., 2014; Carvalho and Vesely 2017; Valdez-Buso et al., 2019; Mottin et al., 2018; Vesely et al., 2018; Schemiko et al., 2019; Rodrigues et al., 2020; 2021).

Large intrabasinal clasts (IC) consist mainly of deltaic sandstone and were identified within the Taciba Formation in the southernmost and northernmost areas (**Figure 18**; outcrops Ib-1, RS-2, RS-4 and RS-5). These clasts extend from tens of meters to 100 m and are a few tens of meters thick (**Figures 19A-E and 23F**). Well preserved bedding, sometimes tilted, occur within these clasts, usually accompanied by sedimentary structures with little or no deformation (Rodrigues et al., 2020). Some of these clasts were described resting on internally deformed diamictite (**Figures 19D and 23F**, Ib-1 and RS-2 respectively). Although large intrabasinal clasts have shown little internal deformation, folds are identified at the base of IC sandstone; these may be related to the clasts' downslope movement and emplacement.

Normal faults and sand injections near to, and in the contact with diamictite, may also relate to the clasts' translation (**Figures 19D and 19E**).

MTDs with slide to slump features were also described in the Taciba Formation, in the Rio do Sul region (e.g., RS-1 and RS-2) (**Figure 18**). These MTDs display well preserved bedding with sedimentary structures and partially preserved bedding with up to 5% of matrix, a result of sediment mixing. Structures consist mainly of normal and reverse faults and folds (symmetric to asymmetric, upright to recumbent folds), as well as symmetric and asymmetric boudins. Other shear-related features, such as quarter-like structures and intrastratal detachment surfaces, are also observed (Fig. 20A-G). When present, the matrix is massive and formed of partially mixed zones with little or no bedding/lamination. These mixed zones occur in the vicinity of disrupted layers with internal bedding/lamination preserved and deformed (**Figure 20F and G**).

Outcrop RS-1 exemplifies MTDs that with deformed layers and a relative lack of matrix. This MTD consist of rhythmite deformed by recumbent folds and, locally, symmetric boudins (**Figure 20A-C**). In turn, outcrop RS-3 presents at least two intervals of deformed rhythmite and sandstone that are separated by an interval of rhythmite with no clear deformation (**Figure 20D-H**). In the lower MTD, exposed in the southernmost part of outcrop RS-3, normal faults and associated thin shear zones subparallel to the lamination correspond to the extensional domain of the MTD. The upper MTD is better exposed and easily accessed in the central to northernmost part of the outcrop, where it shows partially to highly folded layers locally disrupted in symmetric boudins (**Figure 20E-G**). Folds are asymmetric, inclined to recumbent and may show complex patterns with local refolding and thrust faults (**Figure 20E**). Normal fault can deform the folded layers, relating to the main deformation stage or, instead, to a later stage of the mass movement marked by stress relaxation in the compressional domain of the upper MTD. A flow direction toward the NW is reinforced by the location of extensional (lower MTD) and compressional domains (upper MTD) to the south and north, respectively.

MTDs described as debris flows were identified, in the three regions (**Figure 18**), within the Lagoa Azul (CTM-1), Campo Mourão (outcrop CTM-2) and Taciba formations (RS-2, Ib-1, Ib-2 e CTM-3). These debris flows consist of sandy-muddy diamictites with a banded to mostly massive matrix that, usually, forms more than 75% of the volume of the deposit (Rodrigues et al., 2020). The matrix tends to show little (banded diamictites) or no bedding/lamination (massive diamictites), a character that subtly changes on a meter scale within the same outcrop (Rodrigues et al., 2020). In contrast, intrabasinal clasts dispersed within the matrix are disrupted and highly deformed with poorly to well-preserved bedding.

Deformation structures include folds, normal and inverse faults (with or without a sand/clay smear), symmetric and asymmetric boudins, and other shear-related features, such as sheared laminations and/or fragments (**Figures 21, 22 and 23**). These structures are visible in deformed remnants of beds or banded matrix, as well as within sedimentary clasts formed by the rupture or boudinage of larger sandstone blocks. Internal deformation structures in intrabasinal clasts do not affect the surrounding matrix and have been interpreted to predate the clasts rupture (Rodrigues et al., 2020). Deformation styles of intrabasinal clasts thus include faulting, mutual injection between clasts and matrix sediments, and, more commonly, shearing and ‘grooves’ that affect their borders (**Figures 21B, 21C, 21G, 21H, 23A, 23C, 23D and 23G**). Disrupted lenses described in the matrix result from shearing of intrabasinal clasts and remnants of lamination. Other record of deformation described in some diamictites correspond to the preferential orientation of extra- and intrabasinal clasts long axes that tend to be roughly parallel to the flow direction (Rodrigues et al., 2020).

Debris flows from Lagoa Azul Formation were identified in the Campo do Tenente-Mafra region (outcrop CTM-1; **Figures 18 and 21A-E**). The diamictite in CTM-1 is rich in intrabasinal clasts consisting of sandstone and occasionally rhythmites that are deformed internally by faulting and shearing. These intrabasinal clasts tend to occur in the same level with rounded/eye shaped features interpreted as symmetric boudins. Some clasts are deformed by normal faults and tend to show sheared features (mostly at the top and borders of clasts) and grooves/ “scratch” marks at their borders. Sheared sand fragments and remnant lamina in the matrix, together with the faults and shear bands in intrabasinal clasts, indicate shearing during mass flow (Rodrigues et al., 2020).

Mass-transported diamictite from Campo Mourão Formation was described in Campo do Tenente-Mafra region (outcrop CTM-2; **Figures 18 and 21F-M**). This diamictite reveals a higher content of sand compared to other diamictites. Intrabasinal clasts consist of mudstone and rhythmites with internal shear deformation of lamina. Cobble- to boulder-size clasts display sheared borders on which sediments or matrix fragments are incorporated, while intrabasinal granules tend to show a preferential orientation. Subhorizontal to inclined shear planes with mostly normal kinematics and clay smears were described in the matrix and in fractures corssing intrabasinal clasts. The matrix varies from massive to banded along outcrop CTM-2. Banded matrix display folds, asymmetric boudins and shear features.

Mass transport diamictites from the Taciba Formation were described in Ibaiti, Campo do Tenente-Mafra e Rio do Sul regions (outcrops Ib-1, Ib-2, CTM-3 and RS-2) (**Figures 18, 22 and 23**). Diamictites in outcrop Ib-1 and Ib-2 record a heterogeneous matrix (**Figure 22A-D and 22F**). At outcrop Ib-1, the diamictite is characterized by banded matrix deformed by reverse faults and folds that are locally disrupted or show fluidization and injection at their hinges (**Figure 22A-C**). Diamictite at outcrop Ib-2 shows sandy lamina that are sheared and vestiges of folded beds (**Figure 22F**).

MTDs at outcrops CTM-3 and RS-2 tend to show a homogeneous matrix (i.e. they are massive) with portions of heterogeneous matrix with disrupted lamina and preserved remnants of the original bedding (**Figures 23A-E and 23F-I**). Shear planes and zones characterized by clay and sand smear were described in the matrix at both outcrops. At CTM-3, diamictite in the shear planes/zones show both normal and reverse kinematics, whereas shear planes/zones at RS-2 show mostly reverse faults. Shear features such as “S-C” fabrics and asymmetric boudins may occur associated with these shear zones in diamictite intervals. Intrabasinal clasts consist of sandstones and rhythmites that, usually, display internal deformation by folds and faults and border deformation. Reverse faults that affect both matrix and intrabasinal clasts were also identified in these diamictites.

Recent studies in the Campo do Tenente-Mafra and Rio do Sul regions have interpreted MTDs as the result of delta slope collapse caused by high sedimentation rates associated with intervals of maximum ice retreat (Suss et al., 2014; Fallgatter 2015; Carvalho and Vesely 2017; Valdez-Buso et al., 2019; Schemiko et al., 2019). These MTDs have been related to progradational or progradational-aggradational stacking patterns of a clinoform system with fluvio-deltaic to marine deposits, which sourced turbidites and non-cohesive density-flows deposits more distally on the delta slope (Carvalho and Vesely 2017; Schemiko et al., 2019). According to Carvalho and Vesely (2017), a rapid progradation of fluvio-deltaic systems with recurrent collapse of their sand-rich portion is suggested by the occurrence of allochthonous fluvial and deltaic blocks within MTDs. Nevertheless, MTDs in the Ibaiti region were interpreted as resulting from isostatic rebound and base-level fall due to ice-margin retreat, which caused slope instability and the resedimentation of previously accumulated glaciomarine sediments (Mottin et al., 2018).

Sand injections in outcropping MTDs

Sand injections have been described at outcrop in the Campo Mourão and Taciba formations by Rodrigues et al. (2020) (**Figures 18, 20E, 20H, 21I, 21K-M, 22A, 22C-E and 24A-C**). The injectites are composed of very fine to very coarse sand and may show silt, granules (including mud fragments) and fragments of the host rock. These structures seem to be pre-, syn- to post-MTD. According to Rodrigues et al. (2020), no parental rock was identified in most cased. Where the parental rock was identified, it corresponds to sand layers within the MTD (**Figure 24A and C**). Injectites with breccia features were described in one of these cases, sometimes with sheared host-rock fragments (**Figures 24A and24B**). In another cases the injections seem to be syn-MTD, once they deform and are deformed by MTD structures (**Figure 24C**). Such observations indicate sand injection within the MTD due to increase in pore-fluid pressure of sand layers during the mass flow. The trigger mechanism for most sand injection cases and the relationship with MTDs is still not clear and requires further investigation; nevertheless, the recurrence of injectites at outcrops suggests mass flows as a trigger mechanism for sand injection (Strachan 2002).

At outcrop Ib-1, injectites crossing the diamictite consist of first-phase dikes and sills, in places folded with the banded matrix (**Figure 22A, 22D and 22E**). This suggests that the injection of sand predates the mass flow, which naturally occurred when the host rock and injectites were still unconsolidated. In a second phase, thin injectites crosscut the first-stage injectites and folds in the banded matrix (**Figure 22C**). This second phase of injectites occurred in the last phases of the mass flow or even later. Thin irregular to tabular injectites were also described in diamictite intervals at outcrop CTM-2 (Rodrigues et al., 2020) (**Figure 21I, K-M**). These injectites crosscut the deformed banded matrix and clay smear shear planes or zones. They also occur parallel to subparallel to the shear structures. The temporal relationship between injectites and MTD structures suggest intrusion syn- and later to post-mass flow, but no possible parental rock was identified. The slumped MTDs at outcrop RS-3 also present injectites, which crosscut the deformed layers as dikes with an “en échelon” pattern (**Figure 20E and H**). These injectites seem to have occurred after the cessation of mass flow; they were identified locally and without a clear relationship with tectonic structures. They may have been injected due during the relaxation stage of the mass flow.

CONCLUDING REMARKS

Several studies have demonstrated the direct and diverse relationship between different sediment remobilization and petroleum plays, including MTCs and MTDs, mud volcanoes and sand injections. Mud volcanoes and sand injectites are related to overpressured fluid flow occurring in different basins, onshore or offshore, and in different tectonic contexts. Mud volcanoes result from the flow of pressurized fluids with mud at depth, particularly hydrocarbons that ascend to the surface and commonly occur in association with petroleum systems. Therefore, mud volcanoes are considered ideal indicators of hydrocarbon plays that can be targetted for further exploration. Sand injections (or injectites) can influence different aspects of petroleum plays, including reservoir, seal, traps and fluid migration. The distribution and geometry of injectites may affect the distribution of hydrocarbons reservoirs, connect isolated sand bodies, break through rocks that would otherwise be potential seals, indicate fluid migration routes and thief zones. Thus, the occurrence of sand injectites in petroleum systems has consequences for hydrocarbon plumbing systems.

Deepwater traps continue to be important targets for future hydrocarbon exploration and are likely to deliver future volumes in both mature and frontier basins (Amy, 2019; Collard, 2020). The several examples discussed here show that MTCs and MTDs, particularly the thicker and more extensive, may act as seals (top seals or intra-reservoir barriers) or reservoirs in deepwater petroleum systems. In addition, the irregular morphology of these deposits and of the seafloor affected by submarine landslides can influence the deposition of turbidites, which are potental deepwater reservoirs.

Submarine landslides can generate deposits with widely varying characteristics, geometries, morphologies, structures and depositional facies, as exemplified in this Chapter. Although mass transport deposits show domains with preferential aspects of deformation, a wide variety of structures at seismic to subseismic scales, and deformation styles, can occur along these deposits. Furthermore, submarine landslides can be triggered by several coexisting mechanisms in different types of basins and tectonic contexts. Future studies of these deposits at different scales (at seismic to outcrop scales) will help address their different aspects and relationship with other deposits, thus, identifying potential impacts on petroleum systems. Integration of seismic data with core data and comparison with analogous outcrop is probably the best approach to understanding the formation of these deposits and their impacts on petroleum plays. We acknowledge that resolution of seismic data is still unable to define the potential of MTCs to act as a source, reservoir, or seal, and therefore, integration of different datasets is paramount to address the subsurface uncertainty. Moreover, not all MTCs/MTDs are made equal and explorationists need to assess them in a case-by-case scenario.

The phenomena resulting in sediment remobilization generate geohazards and need to be considered in offshore and subsurface projects. Because sediment remobilization can be directly or indirectly related to climate change, understanding how different sediment remobilization processes occur and their roles as geohazards is highly relevant. For instance, changes in marine dynamics, relative sea level, and sediment input can favour the destabilization of submarine slopes and trigger large landslides with the potential to affect infrastructure on the seafloor and generate tsunamis, depending on the volume of remobilized sediments.

The remobilization of sediments associated with fluid flow, including mud volcanoes and sand extrusion (associated with the formation of sand injections), can be triggered by several mechanisms, such as seismicity, high deposition rate and fluid migration. Large sediment remobilization related to submarine landslide may also result in fluid overpressure in underlying sediments and trigger fluid migration, mud volcanism and sand extrusions. Studies also indicate that these sediment remobilizations can affect subsea infrastructures, as well as expulsing fluid and hydrocarbons to the surface to contaminate marine and lacustrine environments. In addition, sediment remobilization associated with fluid flow, particularly mud volcanoes, is an important source of methane. Therefore, these sediment remobilization processes can also contribute to climate change. Lastly, as offshore infrastructure keeps growing in the energy transition landscape, understanding such phenomena and associated deposits will be important for a responsible development of offshore infrastructure.

Acknowledgements

Tiago M. Alves thanks V. Lykousis (HCMR), I. Zananiri, N. Carras and K. Perissoratis (IGME–Athens) for permits to the field campaigns in Crete (2008, 2009, 2013 and 2015-2018). His work on slide blocks in SE Crete was partly sponsored by Royal Society grant RSSV 2008/R3, TEPA's (Total-Angola) RAFTS consortium, Petrobras and Husky Energy. The COST Action ES1301: FLOWS - Impact of Fluid circulation in old oceanic Lithosphere on the seismicity of transfOrm-type plate boundaries: neW solutions for early seismic monitoring of major European Seismogenic zones is acknowledged for a meeting and field trip in 2016. M.C.N.L. Rodrigues thanks the Brazilian National Council for Scientific and

Technological Development for funding the research on the Paraná Basin (CNPq, grant 461650/2014–2, PQ 302842/2017-9 and PQ 306780/2019-4) and the Coordination for the Improvement of Higher Education Personnel (CAPES) for providing a PhD scholarship. In addition to the Federal University of Paraná, colleagues from the Laboratory on Basin Analysis (LABAP) and Professor Ian Alsop (University of Aberdeen) contributed for the research undertaken in Southern Brazil. S. Cardona thanks the Sediment Mechanics Lab at Texas A&M University for funding while writing this chapter. Malcolm Arnot, Greg Browne, Mimi Do and Estefania Lopez are thanked for assistance with fieldwork in New Zealand, and Lesli Wood at the Sedimentary Analogs Database (SAnD) research program and Zane Jobe at the Chevron Center of Research Excellence (CoRE) at Colorado School of Mines for financial, technical, and logistical support for fieldwork. Finally, we thank the comments provided by Editors Jon Rotzien, Javier Hernández- Molina and Octavian Catuneanu, Cindy Yeilding and Richard A. Sears, which have significantly improved this Chapter.

REFERENCES

Abadi S. M., Harris J. C., Grilli S. T., Fabre R. 2012. Numerical modeling of tsunami waves generated by the flank collapse of the Cumbre Vieja Volcano (La Palma, Canary Islands): Tsunami source and near field effects, J. Geophys. Res., 117, C05030, doi:10.1029/2011JC007646.

Acosta J., Uchupi E., Muñoz A., Herranz P., Palomo C., Ballesteros M. 2003. Geologic evolution of the Canary Islands of Lanzarote, Fuerteventura, Gran Canaria and La Gomera and comparison of the landslides at these islands with those at Tenerife, La Palma and El Hierro, Mar. Geophys. Res., 24, 1–40, doi:10.1007/s11001-004-1513-3.

Algar, S., Milton, C., Upshall, H., Roestenburg, J., and Crevello, P., 2011, Mass-Transport Deposits of the Deepwater Northwestern Borneo Margin—Characterization from Seismic-Reflection, Borehole, and Core Data with Implications for Hydrocarbon Exploration and Exploitation, *in* Shipp, R.C., Weimer, P., and Posamentier, H.W. eds., Mass-Transport Deposits in Deepwater Settings, SEPM (Society for Sedimentary Geology), p. 351–366, doi:10.2110/sepmsp.096.351.

Alves, T.M., 2010a, 3D Seismic examples of differential compaction in mass-transport deposits and their effect on post-failure strata: Marine Geology, v. 271, p. 212–224, doi:10.1016/j.margeo.2010.02.014.

Alves, T.M., 2010b, A 3-D morphometric analysis of erosional features in a contourite drift from offshore SE Brazil: Geophysical Journal International, v. 183, p. 1151–1164, doi:10.1111/j.1365-246X.2010.04827.x.

Alves, T.M., 2015, Submarine slide blocks and associated soft-sediment deformation in deep-water basins: A review: Marine and Petroleum Geology, v. 67, p. 262–285, doi:10.1016/j.marpetgeo.2015.05.010.

Alves, T.M., Cartwright, J., and Davies, R.J., 2009, Faulting of salt-withdrawal basins during early halokinesis: Effects on the Paleogene Rio Doce Canyon system (Espírito Santo Basin, Brazil): AAPG Bulletin, v. 93, p. 617–652, doi:10.1306/02030908105.

Alves, T.M., and Cupkovic, T., 2018, Footwall degradation styles and associated sedimentary facies distribution in SE Crete: Insights into tilt-block extensional basins on continental margins: Sedimentary Geology, v. 367, p. 1–19, doi:10.1016/j.sedgeo.2018.02.001.

Alves, T.M., and Lourenço, S.D.N., 2010, Geomorphologic features related to gravitational collapse: Submarine landsliding to lateral spreading on a Late Miocene–Quaternary slope (SE Crete, eastern Mediterranean): Geomorphology, v. 123, p. 13–33, doi:10.1016/j.geomorph.2010.04.030.

Amy, L.A., 2019, A review of producing fields inferred to have upslope stratigraphically trapped turbidite reservoirs: Trapping styles (pure and combined), pinch-out formation, and depositional setting: AAPG Bulletin, v. 103, p. 2861–2889, doi:10.1306/02251917408.

Andresen, K.J., 2021, The Norwegian–Danish Basin: a dynamic setting for subsurface sand remobilization – established concepts on distribution and controlling factors: Geological Society, London, Special Publications, v. 493, p. 47–68, doi:10.1144/SP493-2018-026.

Armitage, D. a., Romans, B.W., Covault, J. a., and Graham, S. a., 2009, The Influence of Mass-Transport-Deposit Surface Topography on the Evolution of Turbidite Architecture: The Sierra Contreras, Tres Pasos Formation (Cretaceous), Southern Chile: Journal of Sedimentary Research, v. 79, p. 287–301, doi:10.2110/jsr.2009.035.

Bellwald, B., Hjelstuen, B.O., Sejrup, H.P., Stokowy, T., and Kuvås, J., 2019, Holocene mass movements in west and mid-Norwegian fjords and lakes: Marine Geology, v. 407, p. 192–212, doi:10.1016/J.MARGEO.2018.11.007.

Berton, F., and Vesely, F.F., 2016, Stratigraphic evolution of Eocene clinoforms from northern Santos Basin, offshore Brazil: Evaluating controlling factors on shelf-margin growth and deep-water sedimentation: Marine and Petroleum Geology, v. 78, p. 356–372, doi:10.1016/j.marpetgeo.2016.09.007.

Bertoni, C., Cartwright, J., and Hermanrud, C., 2013, Evidence for large-scale methane venting due to rapid drawdown of sea level during the Messinian Salinity Crisis: Geology, v. 41, p. 371–374, doi:10.1130/G33987.1.

Bhatnagar, P., Verma, S., and Bianco, R., 2019, Characterization of mass transport deposits using seismic attributes: Upper Leonard Formation, Permian Basin: Interpretation, v. 7, p. SK19–SK32, doi:10.1190/INT-2019-0036.1.

Bhattacharya, S., Verma, S., and Rotzien, J.R., 2020, 3D seismic imaging of the submarine slide blocks on the North Slope, Alaska: Interpretation, v. 8, p. SR37–SR44, doi:10.1190/INT-2020-0038.1.

De Blasio, F. V., 2011, Physical models of giant subaqueous rock avalanches: EPL (Europhysics Letters), v. 96, p. 59004, doi:10.1209/0295-5075/96/59004.

Boulesteix, T., Hildenbrand, A., Soler, V., Quidelleur, X., and Gillot, P.-Y., 2013, Coeval giant landslides in the Canary Islands: Implications for global, regional and local triggers of giant flank collapses on oceanic volcanoes: Journal of Volcanology and Geothermal Research, v. 257, p. 90–98, doi:10.1016/J.JVOLGEORES.2013.03.008.

Bull, S., Cartwright, J., and Huuse, M., 2009, A review of kinematic indicators from mass-transport complexes using 3D seismic data: Marine and Petroleum Geology, v. 26, p. 1132–1151, doi:10.1016/j.marpetgeo.2008.09.011.

Cardona, S., Wood, L.J., Day-Stirrat, R.J., and Moscardelli, L., 2016, Fabric Development and Pore-Throat Reduction in a Mass-Transport Deposit in the Jubilee Gas Field, Eastern Gulf of Mexico: Consequences for the Sealing Capacity of MTDs, *in* Lamarche, G. et al. eds., Submarine Mass Movements and their Consequences, Cham, Springer International Publishing, Advances in Natural and Technological Hazards Research, v. 41, p. 27–37, doi:10.1007/978-3-319-20979-1_3.

Cardona, S., Wood, L.J., Dugan, B., Jobe, Z., and Strachan, L.J., 2020a, Characterization of the Rapanui mass-transport deposit and the basal shear zone: Mount Messenger Formation, Taranaki Basin, New Zealand (J. Baas, Ed.): Sedimentology, v. 67, p. 2111–2148, doi:10.1111/sed.12697.

Cardona, S., Wood, L., Moscardelli, L., and Dunlap, D., 2020b, Cannibalization and sealing of deepwater reservoirs by mass-transport complexes — The Jubilee field, Gulf of Mexico: Interpretation, v. 8, p. SV17–SV30, doi:10.1190/INT-2019-0274.1.

Collard, J., 2020, Searching for Future Super-Basins, *in* Global Super Basins, Sugar Land, AAPG.

Cox, D.R., Huuse, M., Newton, A.M.W., Gannon, P., and Clayburn, J., 2020, Slip sliding away: Enigma of large sandy blocks within a gas-bearing mass transport deposit, offshore northwestern Greenland: AAPG Bulletin, v. 104, p. 1011–1043, doi:10.1306/10031919011.

Cumberpatch, Z., Soutter, E., Kane, I.A., and Casson, M. Evolution of a mixed siliciclastic-carbonate deep-marine system on an unstable margin: the Cretaceous of the Eastern Greater Caucasus, Azerbaijan:, doi:10.31223/OSF.IO/WSVU6.

Dott, R.H., 1963, Dynamics of Subaqueous Gravity Depositional Processes: AAPG Bulletin, v. 47, p. 104–128, doi:10.1306/BC743973-16BE-11D7-8645000102C1865D.

Doughty-Jones, G., Lonergan, L., Mayall, M., and Dee, S., 2019, The role of structural growth in controlling the facies and distribution of mass transport deposits in a deep-water salt minibasin: Marine and Petroleum Geology, v. 104, p. 106–124, doi:10.1016/J.MARPETGEO.2019.03.015.

Dunlap, D.B., Wood, L.J., Weisenberger, C., and Jabour, H., 2010, Seismic geomorphohgy of offshore Morocco's east margin, Safi Haute Mer area: AAPG Bulletin, v. 94, p. 615–642, doi:10.1306/10270909055.

Dykstra, M., Garyfalou, K., Kertznus, V., Kneller, B., Milana, J.P., Molinaro, M., Szuman, M., and Thompson, P., 2011, Mass-Transport Deposits: Combining Outcrop Studies and

Seismic Forward Modeling to Understand Lithofacies Distributions, Deformation, and their Seismic Stratigraphic Expression, *in* Mass-Transport Deposits in Deepwater Settings, SEPM (Society for Sedimentary Geology), p. 293–310, doi:10.2110/sepmsp.096.293.

Eng, C., and Tsuji, T., 2019, Influence of faults and slumping on hydrocarbon migration inferred from 3D seismic attributes: Sanriku-Oki forearc basin, northeast Japan: Marine and Petroleum Geology, v. 99, p. 175–189, doi:10.1016/J.MARPETGEO.2018.10.013.

Eyles, and Eyles, 2001, Subaqueous mass flow origin for Lower Permian diamictites and associated facies of the Grant Group, Barbwire Terrace, Canning Basin, Western Australia: Sedimentology, v. 47, p. 343–356, doi:10.1046/j.1365-3091.2000.00295.x.

Fairbridge, R.W., 1946, Submarine Slumping and Location of Oil Bodies: AAPG Bulletin, v. 30, p. 84–92, doi:10.1306/3D9337C8-16B1-11D7-8645000102C1865D.

Farrell, S.G., 1984, A dislocation model applied to slump structures, Ainsa Basin, South Central Pyrenees: Journal of Structural Geology, v. 6, p. 727–736, doi:10.1016/0191-8141(84)90012-9.

Festa, A., Ogata, K., Pini, G.A., Dilek, Y., and Alonso, J.L., 2016, Origin and significance of olistostromes in the evolution of orogenic belts: A global synthesis: Gondwana Research, v. 39, p. 180–203, doi:10.1016/j.gr.2016.08.002.

Frey-Martínez, J., 2010, 3D Seismic Interpretation of Mass Transport Deposits: Implications for Basin Analysis and Geohazard Evaluation, *in* Submarine Mass Movements and Their Consequences, Dordrecht, Springer Netherlands, p. 553–568, doi:10.1007/978-90-481-3071-9_45.

Frey-Martínez, J., Cartwright, J., and James, D., 2006, Frontally confined versus frontally emergent submarine landslides: A 3D seismic characterisation: Marine and Petroleum Geology, v. 23, p. 585–604, doi:10.1016/j.marpetgeo.2006.04.002.

Gamboa, D., and Alves, T.M., 2016, Bi-modal deformation styles in con fi ned mass-transport deposits : Examples from a salt minibasin in SE Brazil: Marine Geology, v. 379, p. 176–193, doi:10.1016/j.margeo.2016.06.003.

Gamboa, D., and Alves, T.M., 2015, Spatial and dimensional relationships of submarine slope architectural elements: A seismic-scale analysis from the EspIrito Santo Basin (SE Brazil): Marine and Petroleum Geology, v. 64, p. 43–57, doi:10.1016/j.marpetgeo.2015.02.035.

Gamboa, D., Alves, T., Cartwright, J., and Terrinha, P., 2010, MTD distribution on a “passive” continental margin: The Espírito Santo Basin (SE Brazil) during the Palaeogene: Marine and Petroleum Geology, v. 27, p. 1311–1324, doi:10.1016/j.marpetgeo.2010.05.008.

Giachetti, T., Paris, R., Kelfoun, K., and Pérez-Torrado, F.J., 2011, Numerical modelling of the tsunami triggered by the Güìmar debris avalanche, Tenerife (Canary Islands): Comparison with field-based data: Marine Geology, v. 284, p. 189–202, doi:10.1016/J.MARGEO.2011.03.018.

Godo, T.J., 2006, Identification of stratigraphic traps with subtle seismic amplitude effects in Miocene channel/levee sand systems, NE Gulf of Mexico: Geological Society Special Publication, v. 254, p. 127–151, doi:10.1144/GSL.SP.2006.254.01.07.

Le Goff, J., Slootman, A., Mulder, T., Cavailhes, T., Ducassou, E., Hanquiez, V., Jaballah, J., and Reijmer, J.J.G., 2020, On the architecture of intra-formational Mass-Transport Deposits: Insights from the carbonate slopes of Great Bahama Bank and the Apulian Carbonate Platform: Marine Geology, v. 427, p. 106205, doi:10.1016/j.margeo.2020.106205.

Grilli, S.T. et al., 2019, Modelling of the tsunami from the December 22, 2018 lateral collapse of Anak Krakatau volcano in the Sunda Straits, Indonesia: Scientific Reports, v. 9, p. 11946, doi:10.1038/s41598-019-48327-6.

Grippa, A., Hurst, A., Palladino, G., Iacopini, D., Lecomte, I., and Huuse, M., 2019. Seismic imaging of complex geometry: Forward modeling of sandstone intrusions. Earth and Planetary Science Letters, v. 513, p. 51-63, doi: 10.1016/j.epsl.2019.02.011.

Gutierrez, M.A., and Snedden, J.W., 2021, Integrated characterization and failure mechanism for a mid-Pleistocene mass transport complex-dominant interval in the Mars Ursa Basin, northern Gulf of Mexico, USA: Interpretation, v. 9, p. T253–T274, doi:10.1190/INT-2019-0293.1.

Haflidason, H., Sejrup, H.P., Berstad, I.M., Nygård, A., Richter, T., Bryn, P., Lien, R., and Berg, K., 2003, A Weak Layer Feature on the Northern Storegga Slide Escarpment, *in* European Margin Sediment Dynamics, Berlin, Heidelberg, Springer Berlin Heidelberg, p. 55–62, doi:10.1007/978-3-642-55846-7_7.

Henry, L.C., Wadsworth, J.A., Hansen, B., and Hartman, K., 2018, Erosion and ponding of Thunder Horse deepwater turbidites by mass transport complexes in Mississippi Canyon based on image log sedimentology: Marine and Petroleum Geology, v. 97, p. 639–658, doi:10.1016/J.MARPETGEO.2018.08.006.

Ho, S., Hovland, M., Blouet, J.-P., Wetzel, A., Imbert, P., and Carruthers, D., 2018, Formation of linear planform chimneys controlled by preferential hydrocarbon leakage and anisotropic stresses in faulted fine-grained sediments, offshore Angola: Solid Earth, v. 9, p. 1437–1468, doi:10.5194/se-9-1437-2018.

Houseknecht, D.W., 2019, Petroleum systems framework of significant new oil discoveries in a giant Cretaceous (Aptian–Cenomanian) clinothem in Arctic Alaska: AAPG Bulletin, v. 103, p. 619–652, doi:10.1306/08151817281.

Houseknecht, D.W., and Schenk, C.J., 2007, Outcrops of turbidite channel facies in the Torok Formation: reservoir analogs for the Alaska North Slope, *in* Nilsen, T., Shew, R.D., Steffens, G.S., and Studlick, J.R.J. eds., An Atlas of Deepwater Outcrops – Models and Analogs, Am. Assoc. Petrol. Geologists Geol. Stud., p. 373–377, doi:10.1306/1240980St5685.

Hühnerbach, V., and Masson, D.G., 2004, Landslides in the North Atlantic and its adjacent seas: an analysis of their morphology, setting and behaviour: Marine Geology, v. 213, p. 343–362, doi:10.1016/J.MARGEO.2004.10.013.

Hunt, J.E., Wynn, R.B., Talling, P.J., and Masson, D.G., 2013, Multistage collapse of eight western Canary Island landslides in the last 1.5 Ma: Sedimentological and geochemical evidence from subunits in submarine flow deposits: Geochemistry, Geophysics, Geosystems, v. 14, p. 2159–2181, doi:10.1002/ggge.20138.

Hurst, A., Scott, A., and Vigorito, M., 2011, Physical characteristics of sand injectites: Earth-Science Reviews, v. 106, p. 215–246, doi:10.1016/J.EARSCIREV.2011.02.004.

Jablonská, D., Di Celma, C.N., Alsop, G.I., and Tondi, E., 2018, Internal architecture of mass-transport deposits in basinal carbonates: A case study from southern Italy (C. Betzler, Ed.): Sedimentology, v. 65, p. 1246–1276, doi:10.1111/sed.12420.

Jablonska, D., Pitts, A., Di Celma, C., Volatili, T., Alsop, G.I., and Tondi, E., 2021, 3D outcrop modelling of large discordant breccia bodies in basinal carbonates of the Apulian margin, Italy: Marine and Petroleum Geology, v. 123, p. 104732, doi:10.1016/J.MARPETGEO.2020.104732.

Jackson, C.A.-L., and Johnson, H.D., 2009, Sustained turbidity currents and their interaction with debrite-related topography; Labuan Island, offshore NW Borneo, Malaysia: Sedimentary Geology, v. 219, p. 77–96, doi:10.1016/J.SEDGEO.2009.04.008.

Johnson, R.C., Birdwell, J.E., Brownfield, M.E., and Mercier, T.J., 2015, Mass-Movement Deposits in the Lacustrine Eocene Green River Formation , Piceance Basin , Western Colorado:, doi:10.3133/ofr20151044.

Kessler, F., and Jong, J., 2018, Hydrocarbon Retention In Clastic Reservoirs Of NW Borneo - Examples Of Hydrocarbon Trap, Reservoir, Seal And Implications On Hydrocarbon Column Length: Berita Sedimentologi, v. 40, p. 6–44.

Kneller, B., Dykstra, M., Fairweather, L., and Milana, J.P., 2016, Mass-transport and slope accommodation: Implications for turbidite sandstone reservoirs: AAPG Bulletin, v. 100, p. 213–235, doi:10.1306/09011514210.

Kumar, P.C., Omosanya, K.O., Eruteya, O.E., and Sain, K., 2021, Geomorphological characterization of basal flow markers during recurrent mass movement: A case study from the Taranaki Basin, offshore New Zealand: Basin Research, v. 33, p. 2358–2382, doi:10.1111/bre.12560.

Kvalstad, T.J., Andresen, L., Forsberg, C.F., Berg, K., Bryn, P., and Wangen, M., 2005, The Storegga slide: evaluation of triggering sources and slide mechanics: Marine and Petroleum Geology, v. 22, p. 245–256, doi:10.1016/J.MARPETGEO.2004.10.019.

Lee, H.J., Locat, J., Desgagns, P., Parsons, J.D., McAdoo, B.G., Orange, D.L., Puig, P., Wong, F.L., Dartnell, P., and Boulanger, E., 2007, Submarine Mass Movements on Continental Margins, *in* Continental Margin Sedimentation, Oxford, UK, Blackwell Publishing Ltd., p. 213–274, doi:10.1002/9781444304398.ch5.

Lewis, K., 1971, Slumping on a continental slope inclined at 1–4°: Sedimentology, v. 16, p. 97–110, http://onlinelibrary.wiley.com/doi/10.1111/j.1365-3091.1971.tb00221.x/abstract (accessed October 2014).

Martinsen, O.J., and Bakken, B., 1990, Extensional and compressional zones in slumps and slides in the Namurian of County Clare, Ireland: Journal of the Geological Society, v. 147, p. 153–164, doi:10.1144/gsjgs.147.1.0153.

Masson, D.G., Le Bas, T.P., Grevemeyer, I., and Weinrebe, W., 2008, Flank collapse and large-scale landsliding in the Cape Verde Islands, off West Africa: Geochemistry, Geophysics, Geosystems, v. 9, p. n/a-n/a, doi:10.1029/2008GC001983.

Masson, D.G., Harbitz, C.B., Wynn, R.B., Pedersen, G., and Lovholt, F., 2006, Submarine landslides: processes, triggers and hazard prediction: Philosophical Transactions of the Royal Society A: Mathematical, Physical and Engineering Sciences, v. 364, p. 2009–2039, doi:10.1098/rsta.2006.1810.

Masson, D.G., Watts, A.B., Gee, M.J.R., Urgeles, R., Mitchell, N.C., Le Bas, T.P., and Canals, M., 2002, Slope failures on the flanks of the western Canary Islands: Earth-Science Reviews, v. 57, p. 1–35, doi:10.1016/S0012-8252(01)00069-1.

McAdoo, B.., Pratson, L.., and Orange, D.., 2000, Submarine landslide geomorphology, US continental slope: Marine Geology, v. 169, p. 103–136, doi:10.1016/S0025-3227(00)00050-5.

Meckel, L.D., 2011, Reservoir characteristics and classification of sand-prone submarine mass-transport deposits, *in* Ship, R.C., Weimer, P., and Posamentier, H.W. eds., Mass-Transport Deposits in Deepwater Settings, Society of Sedimentary Geology (SEPM), p. 423–452, http://sepm.org/CM_Files/sp 96 TOC and abstracts.pdf.

Middleton, G.V., and Hampton, M.A., 1976, Subaqueous sediment transport and deposition by sediment gravity flows, *in* Stanley, D.J. and Swift, D.J.P. eds., Marine sediment transport and environmental management, New York, Wiley, p. 197–218.

Milkov, A.., 2000, Worldwide distribution of submarine mud volcanoes and associated gas hydrates: Marine Geology, v. 167, p. 29–42, doi:10.1016/S0025-3227(00)00022-0.

Moscardelli, L., 2007, Mass Transport Processes and Deposits in Offshore Trinidad and Venezuela, and their role in Continental Margin Development: PhD Dissertation thesis: The University of Texas at Austin, 185 p.

Moscardelli, L., Ochoa, J., Hunt, I., and Zahm, L., 2019, Mixed siliciclastic–carbonate systems and their impact for the development of deep-water turbidites in continental margins: A case study from the Late Jurassic to Early Cretaceous Shelburne subbasin in offshore Nova Scotia: AAPG Bulletin, v. 103, p. 2487–2520, doi:10.1306/02151917318.

Moscardelli, L., and Wood, L., 2016, Morphometry of mass-transport deposits as a predictive tool: Geological Society of America Bulletin, v. 128, p. 47–80, doi:10.1130/B31221.1.

Moscardelli, L., and Wood, L., 2008, New classification system for mass transport complexes in offshore Trinidad: Basin Research, v. 20, p. 73–98, doi:10.1111/j.1365-2117.2007.00340.x.

Moscardelli, L., Wood, L., and Mann, P., 2006, Mass-transport complexes and associated processes in the offshore area of Trinidad and Venezuela: AAPG Bulletin, v. 90, p. 1059–1088, doi:10.1306/02210605052.

Muhari, A., Heidarzadeh, M., Susmoro, H., Nugroho, H.D., Kriswati, E., Supartoyo, Wijanarto, A.B., Imamura, F., and Arikawa, T., 2019, The December 2018 Anak Krakatau Volcano Tsunami as Inferred from Post-Tsunami Field Surveys and Spectral

Analysis: Pure and Applied Geophysics, v. 176, p. 5219–5233, doi:10.1007/s00024-019-02358-2.

Naranjo-Vesga, J., Ortiz-Karpf, A., Wood, L., Jobe, Z., Paniagua-Arroyave, J.F., Shumaker, L., Mateus-Tarazona, D., and Galindo, P., 2020, Regional controls in the distribution and morphometry of deep-water gravitational deposits along a convergent tectonic margin. Southern Caribbean of Colombia: Marine and Petroleum Geology, v. 121, p. 104639, doi:10.1016/J.MARPETGEO.2020.104639.

Nisbet, E.G., and Piper, D.J.W., 1998, Giant submarine landslides: Nature, v. 392, p. 329–330, doi:10.1038/32765.

Nissen, S.E., Haskell, N.L., Steiner, C.T., and Coterill, K.L., 1999, Debris flow outrunner blocks, glide tracks, and pressure ridges identified on the Nigerian continental slope using 3-D seismic coherency: The Leading Edge, v. 18, p. 595, doi:10.1190/1.1438343.

Nugraha, H.D., Jackson, C.A.-L., Johnson, H.D., and Hodgson, D.M., 2020, Lateral variability in strain along the toewall of a mass transport deposit: a case study from the Makassar Strait, offshore Indonesia: Journal of the Geological Society, v. 177, p. 1261–1279, doi:10.1144/jgs2020-071.

Oehler, J.-F., Lénat, J.-F., and Labazuy, P., 2008, Growth and collapse of the Reunion Island volcanoes: Bulletin of Volcanology, v. 70, p. 717–742, doi:10.1007/s00445-007-0163-0.

Ogata, K., Mountjoy, J.J., Pini, G.A., Festa, A., and Tinterri, R., 2014, Shear zone liquefaction in mass transport deposit emplacement: A multi-scale integration of seismic reflection and outcrop data: Marine Geology, v. 356, p. 50–64, doi:10.1016/j.margeo.2014.05.001.

Ogiesoba, O., and Hammes, U., 2012, Seismic interpretation of mass-transport deposits within the upper Oligocene Frio Formation, south Texas Gulf Coast: AAPG Bulletin, v. 96, p. 845–868, doi:10.1306/09191110205.

Ortiz-Karpf, A., Hodgson, D.M., Jackson, C.A.-L., and McCaffrey, W.D., 2018, Mass-transport complexes as markers of deep-water fold-and-thrust belt evolution: insights from the southern Magdalena fan, offshore Colombia: Basin Research, v. 30, p. 65–88, doi:10.1111/bre.12208.

Palladino, G., Alsop. G.I., Grippa, A., Zvirtes, G., Phillip, R.P., and Hurst, A., 2018. Sandstone-filled normal faults: A case study from central California: Journal of Structural Geology, v. 110, p. 86-101, doi: 10.1016/j.jsg.2018.02.013.

Palan, K., Green, A.N., Andrews, B., Sink, K., and Wiles, E.A., 2020, A morphometric analysis of the fluid flow features of the southern Orange Basin, South Africa: Marine Geology, v. 423, p. 106145, doi:10.1016/J.MARGEO.2020.106145.

Paris, R. et al., 2018, Mega-tsunami conglomerates and flank collapses of ocean island volcanoes: Marine Geology, v. 395, p. 168–187, doi:10.1016/J.MARGEO.2017.10.004.

Paris, A., Heinrich, P., Paris, R., and Abadie, S., 2020, The December 22, 2018 Anak Krakatau, Indonesia, Landslide and Tsunami: Preliminary Modeling Results: Pure and Applied Geophysics, v. 177, p. 571–590, doi:10.1007/s00024-019-02394-y.

Pérez-Torrado, F.J., Paris, R., Cabrera, M.C., Schneider, J.-L., Wassmer, P., Carracedo, J.-C., Rodríguez-Santana, Á., and Santana, F., 2006, Tsunami deposits related to flank collapse in oceanic volcanoes: The Agaete Valley evidence, Gran Canaria, Canary Islands: Marine Geology, v. 227, p. 135–149, doi:10.1016/J.MARGEO.2005.11.008.

Pickering, K.T. (Kevin T.., and Hiscott, R.N., 2015, Deep-marine systems : processes, deposits, environments, tectonics and sedimentation: American Geophysical Union, https://www.wiley.com/en-us/Deep+Marine+Systems%3A+Processes%2C+Deposits%2C+Environments%2C+Tectonics+and+Sedimentation-p-9781118865422 (accessed April 2020).

Posamentier, H.W., and Kolla, V., 2003, Seismic Geomorphology and Stratigraphy of Depositional Elements in Deep-Water Settings: Journal of Sedimentary Research, v. 73, p. 367–388, doi:10.1306/111302730367.

Posamentier, H.W., and Martinsen, O.J., 2011, The character and genesis of submarine mass-transport deposits: insights from outcrop and 3D seismic data, *in* Shipp, R.C., Weimer, P., and Posamentier, H.W. eds., Mass-transport deposits in deepwater settings, SEPM Tulsa, p. 7–38.

Roelofse, C., Alves, T.M., and Gafeira, J., 2020, Structural controls on shallow fluid flow and associated pockmark fields in the East Breaks area, northern Gulf of Mexico: Marine and Petroleum Geology, v. 112, p. 104074, doi:10.1016/J.MARPETGEO.2019.104074.

Roy, S., Senger, K., Hovland, M., Römer, M., and Braathen, A., 2019, Geological controls on shallow gas distribution and seafloor seepage in an Arctic fjord of Spitsbergen, Norway: Marine and Petroleum Geology, v. 107, p. 237–254, doi:10.1016/j.marpetgeo.2019.05.021.

Safadi, M., Meilijson, A., and Makovsky, Y., 2017, Internal deformation of the southeast Levant margin through continued activity of buried mass transport deposits: Tectonics, v. 36, p. 559–581, doi:10.1002/2016TC004342.

Sakellariou, D., and Tsampouraki-Kraounaki, K., 2019, Plio-Quaternary Extension and Strike-Slip Tectonics in the Aegean, *in* Transform Plate Boundaries and Fracture Zones, Elsevier, p. 339–374, doi:10.1016/B978-0-12-812064-4.00014-1.

Sawyer, D.E., Flemings, P.B., Dugan, B., and Germaine, J.T., 2009, Retrogressive failures recorded in mass transport deposits in the Ursa Basin, Northern Gulf of Mexico: Journal of Geophysical Research, v. 114, p. B10102, doi:10.1029/2008JB006159.

Scarselli, N., McClay, K., and Elders, C., 2016, Seismic geomorphology of cretaceous megaslides offshore Namibia (Orange Basin): Insights into segmentation and degradation of gravity-driven linked systems: Marine and Petroleum Geology, v. 75, p. 151–180, doi:10.1016/J.MARPETGEO.2016.03.012.

Scarselli, N. (2020). Chapter 16 - Submarine landslides – architecture, controlling factors and environments. A summary. In: Scarselli, N., Adam, J., Chiarella, D., Roberts, D.G., Bally, A.W. *Regional Geology and Tectonics - second edition*. Vol. 1: Principles of Geological Analysis, Elsevier, p. 417-439, doi: 10.1016/B978-0-444-64134-2.00015-8.

Shanmugam, G., Shrivastava, S.K., and Das, B., 2009, Sandy Debrites and Tidalites of Pliocene Reservoir Sands in Upper-Slope Canyon Environments, Offshore Krishna-Godavari Basin (India): Implications: Journal of Sedimentary Research, v. 79, p. 736–756, doi:10.2110/jsr.2009.076.

Sharman, G.R., Graham, S.A., Masalimova, L.U., Shumaker, L.E., and King, P.R., 2015, Spatial patterns of deformation and paleoslope estimation within the marginal and central portions of a basin-floor mass-transport deposit, Taranaki Basin, New Zealand: Geosphere, v. 11, p. 266–306, doi:10.1130/GES01126.1.

Sobiesiak, M.S., Alsop, G.I., Kneller, B., and Milana, J.P., 2017, Sub-seismic scale folding and thrusting within an exposed mass transport deposit: A case study from NW Argentina: Journal of Structural Geology, v. 96, p. 176–191, doi:10.1016/j.jsg.2017.01.006.

Steventon, M.J., Jackson, C.A.-L., Hodgson, D.M., and Johnson, H.D., 2019, Strain analysis of a seismically imaged mass-transport complex, offshore Uruguay: Basin Research, doi:10.1111/bre.12337.

Steventon, M.J., Jackson, C.A.-L., Johnson, H.D., Hodgson, D.M., Kelly, S., Omma, J., Gopon, C., Stevenson, C., and Fitch, P., 2021, Evolution of a sand-rich submarine channel-lobe system and impact of mass-transport and transitional flow deposits on reservoir heterogeneity: Magnus Field, northern North Sea: Petroleum Geoscience, p. petgeo2020- 095, doi:10.1144/petgeo2020-095.

Strachan, L.J., 2008, Flow transformations in slumps: A case study from the Waitemata Basin, New Zealand: Sedimentology, v. 55, p. 1311–1332, doi:10.1111/j.1365-3091.2007.00947.x.

Sultan, N. et al., 2004, Triggering mechanisms of slope instability processes and sediment failures on continental margins: A geotechnical approach: Marine Geology, v. 213, p. 291–321, doi:10.1016/j.margeo.2004.10.011.

Sun, Q., and Alves, T., 2020, Petrophysics of fine-grained mass-transport deposits: A critical review: Journal of Asian Earth Sciences, v. 192, p. 104291, doi:10.1016/J.JSEAES.2020.104291.

Sun, Q., Alves, T., Xie, X., He, J., Li, W., and Ni, X., 2017, Free gas accumulations in basal shear zones of mass-transport deposits (Pearl River Mouth Basin, South China Sea): An important geohazard on continental slope basins: Marine and Petroleum Geology, v. 81, p. 17–32, doi:10.1016/j.marpetgeo.2016.12.029.

Tanavsuu-Milkeviciene, K., and Sarg, J.F., 2012, Evolution of an organic-rich lake basin - stratigraphy, climate and tectonics: Piceance Creek basin, Eocene Green River Formation: Sedimentology, v. 59, p. 1735–1768, doi:10.1111/j.1365-3091.2012.01324.x.

Urgeles, R., and Camerlenghi, A., 2013, Submarine landslides of the Mediterranean Sea: Trigger mechanisms, dynamics, and frequency-magnitude distribution: Journal of Geophysical Research: Earth Surface, v. 118, p. 2600–2618, doi:10.1002/2013JF002720.

Walker, W., Jobe, Z.R., Sarg, J.F., and Wood, L., 2021, Progradational slope architecture and sediment distribution in outcrops of the mixed carbonate-siliciclastic Bone Spring Formation, Permian Basin, west Texas: Geosphere, v. 17, p. 1268–1293, doi:10.1130/GES02355.1.

Ward, N.I.P., Alves, T.M., and Blenkinsop, T.G., 2018, Submarine sediment routing over a blocky mass-transport deposit in the Espírito Santo Basin, SE Brazil: Basin Research, v. 30, p. 816–834, doi:10.1111/bre.12282.

Weimer, P., 1989, Sequence stratigraphy of the Mississippi fan (Plio-Pleistocene), Gulf of Mexico: Geo-Marine Letters, v. 9, p. 185–272, doi:10.1007/BF02431072.

Weimer, P., and Shipp, C., 2004, Mass Transport Complex: Musing on Past Uses and Suggestions for Future Directions, *in* Offshore Technology Conference, Offshore Technology Conference, p. 1–10, doi:10.4043/16752-MS.

Wenau, S., Spiess, V., and Zabel, M., 2021, Giant Seafloor Depressions Caused by Slope Failures and Bottom Currents on the Namibia Continental Margin: Geochemistry, Geophysics, Geosystems, v. 22, p. e2020GC009548, doi:10.1029/2020GC009548.

Woodcock, N., 1979, Sizes of submarine slides and their significance: Journal of Structural Geology, v. 1, p. 137–142, doi:10.1016/0191-8141(79)90050-6.

Zengaffinen, T., Løvholt, F., Pedersen, G.K., and Muhari, A., 2020, Modelling 2018 Anak Krakatoa Flank Collapse and Tsunami: Effect of Landslide Failure Mechanism and

Dynamics on Tsunami Generation: Pure and Applied Geophysics, v. 177, p. 2493–2516, doi:10.1007/s00024-020-02489-x.

FIGURES

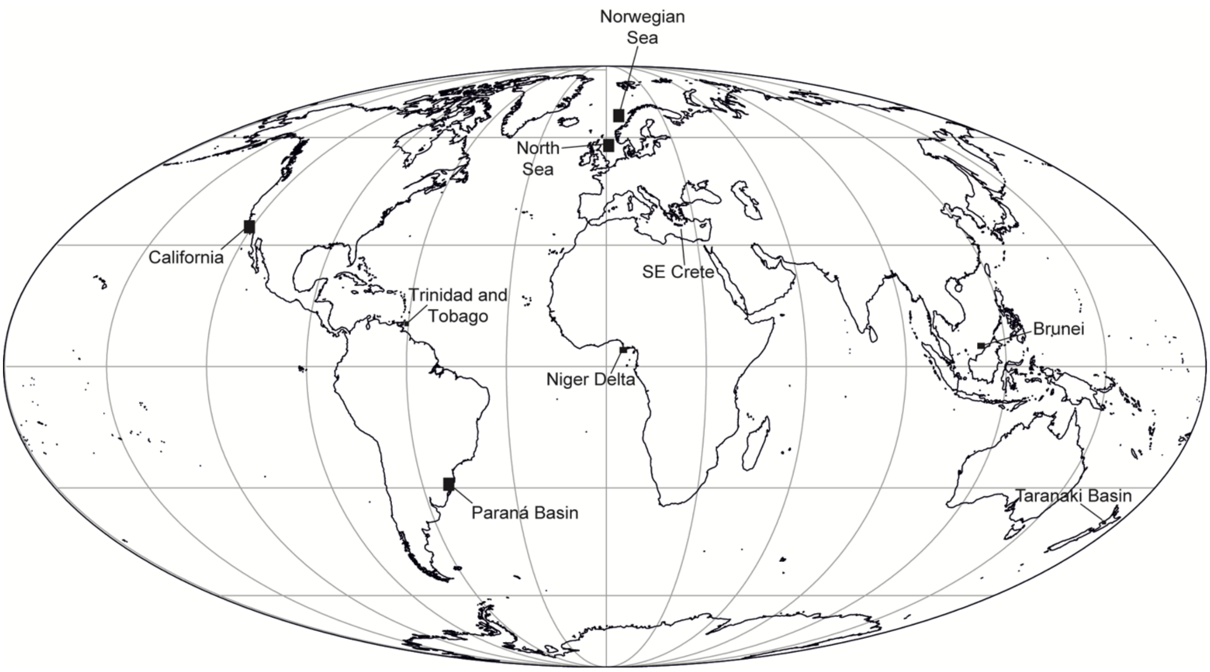

Figure 1 World map indicating the location of the case studies documented in this Chapter. The distribution of the sediment remobilization features referred to in the Chapter is associated with the regional tectonic setting and includes: a) mass-wasting on tectonically active continental margins, b) sand injection features in discrete, overpressured basins, c) mass-flows (non-glacial) occurring in proglacial marine deposits and related to ice-margin retreat in an intracratonic basin. Main triggers of sediment remobilization are varied and have a clear relationship to local physiography and the stress history of sediments below these same remobilization features.

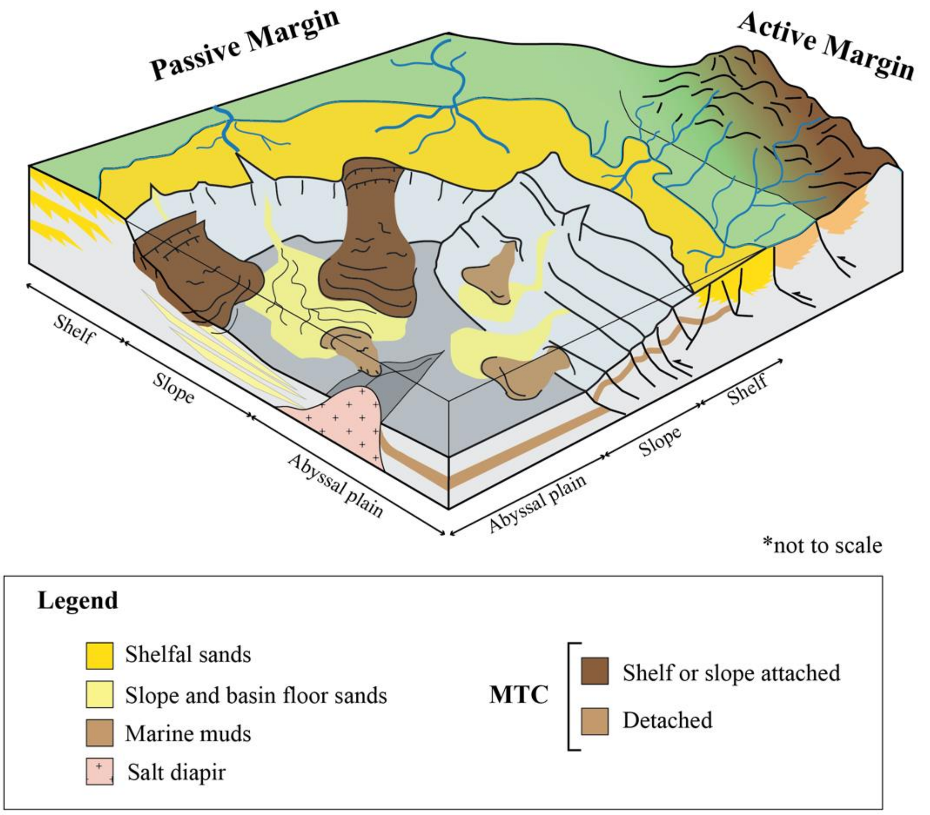
Passive Margin
Active Margin
Shelf
Slope
Abyssal plain
Abyssal plain
Slope
Shelf
*not to scale
Legend
Shelfal sands
Slope and basin floor sands
Marine muds
Salt diapir
MTC
Shelf or slope attached
Detached

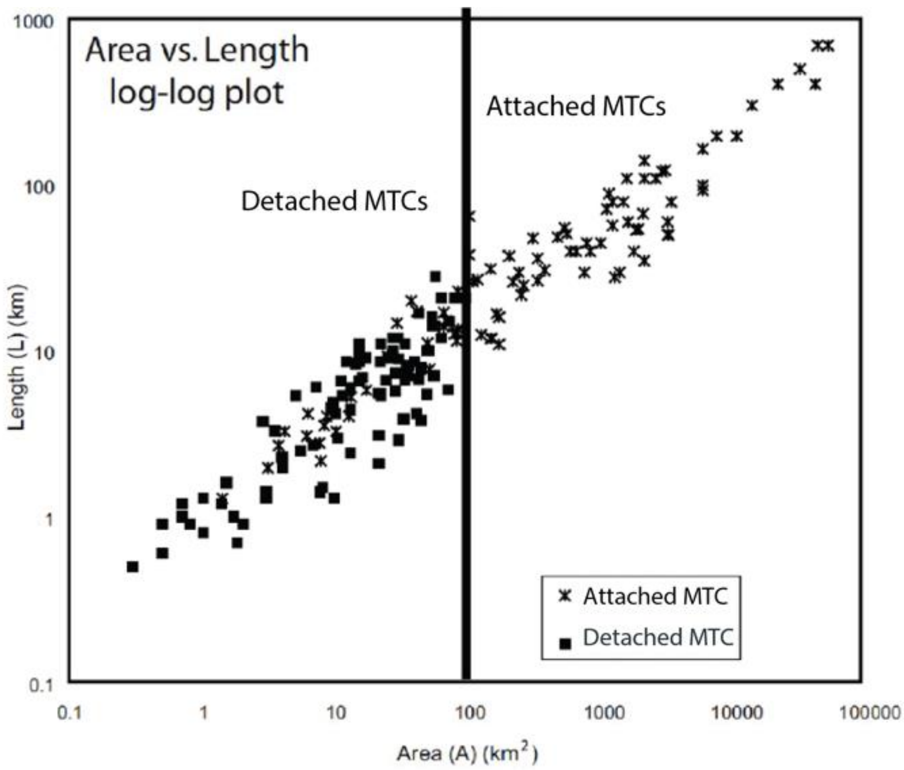
Area vs. Length
log-log plot
Attached MTCs
Detached MTCs
Attached MTC
Detached MTC
Length (L) (km)
Area (A) (km^2)
1000
100
10
1
0.1
0.1
1
10
100
1000
10000
100000

Figure 2 Schematic model of attached and detached mass transport complexes (MTC) in active and passive margins. Log-log scatter plot of length (km) versus area (km^2) for several detached and attached MTCs. Note that attached MTCs (either slope or shelf attached) typically cover larger areas in comparison to detached ones. Data for plot found in Moscardelli (2007).

(A)

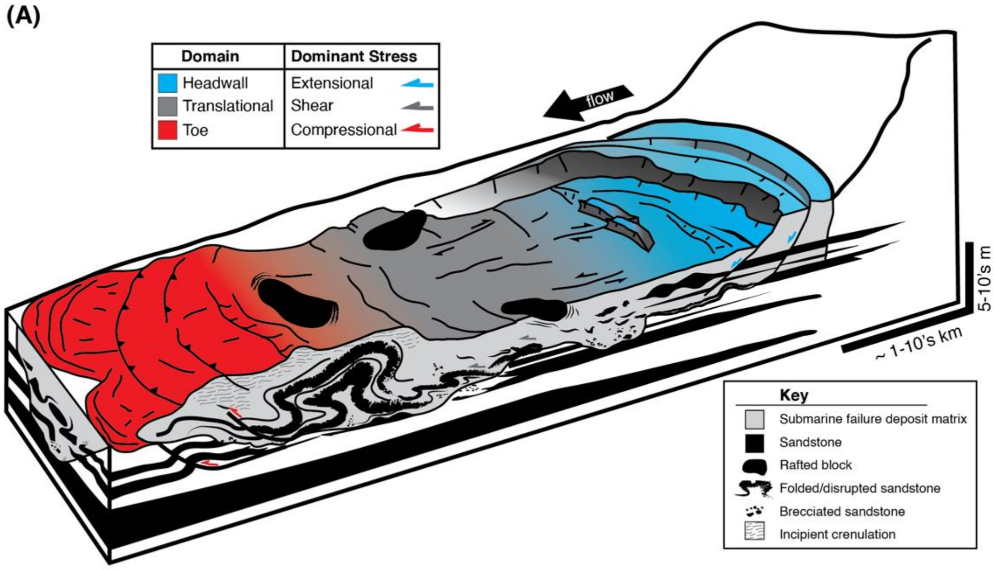

(B)

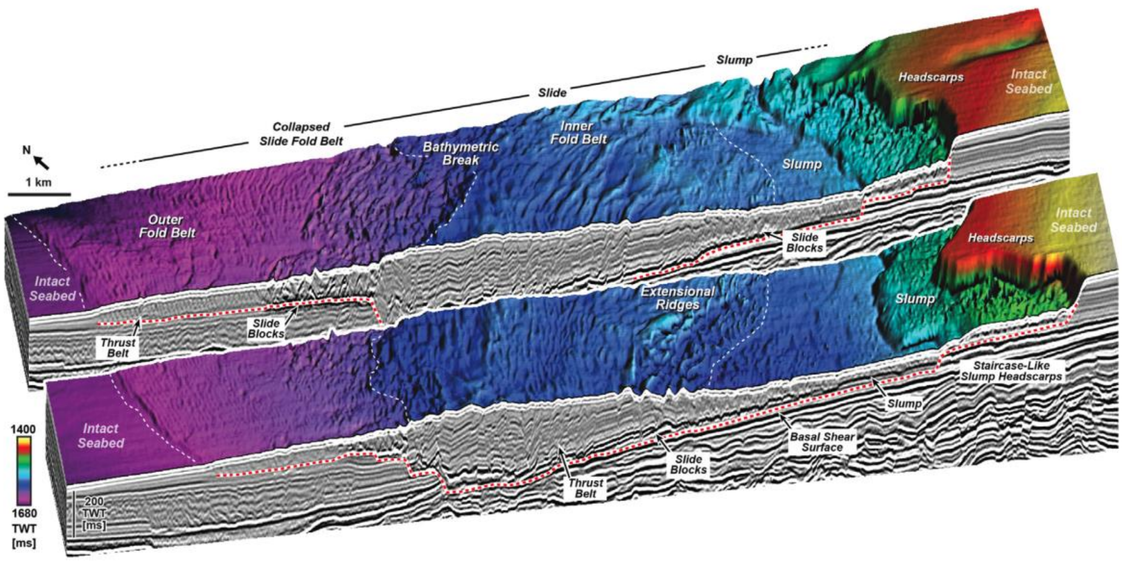

Figure 3 A) Idealized submarine failure deposit with the three typical MTD domains and corresponding dominant stress. (B) Seismic example of a submarine mass transport complex (MTC) at the seafloor in Exmouth Plateau, NW shelf of Australia, whereby stress-dominant domains are characterized by the identification of strain structures. Figure is modified from Scarcelli (2020).

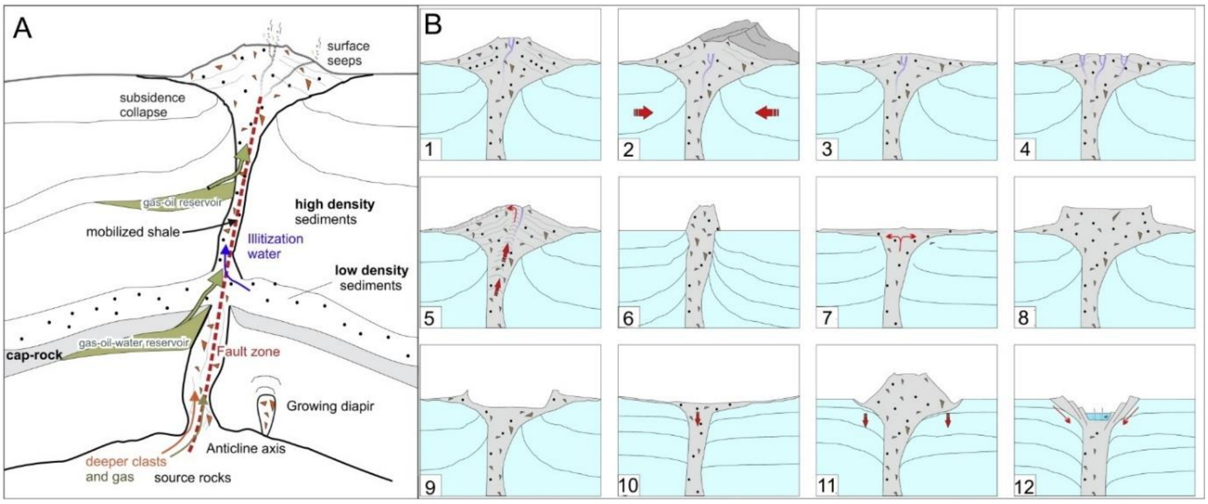

Figure 4 A) Conceptual drawing indicating the main elements that compose most mud volcanoes and corresponding sources of fluids (from Mazzini and Etiope, 2017). B) Mud volcanoes morphologies: 1) conical, 2) elongated, 3) pie-shaped, 4) multicrater, 5) growing diapir-like, 6) stiff neck, 7) swamp-like, 8) plateau-like, 9) impact craterlike, 10) subsiding structure, 11) Subsiding flanks, 12) sink-hole type.

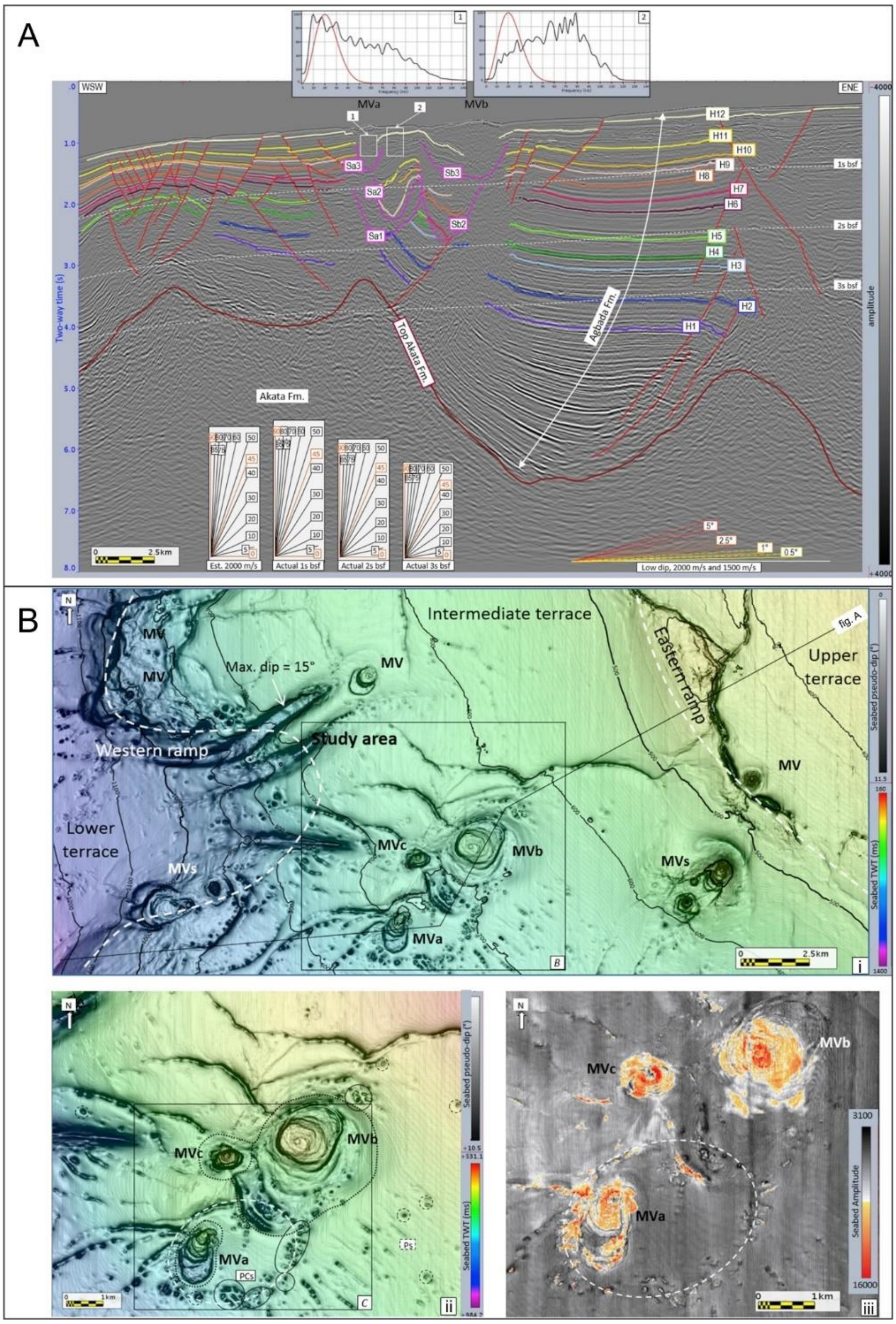

Figure 5 Example of seismic section (A) and seafloor maps from 3D seismic data (B) from mud volcanoes in the western lobe of Niger Delta system, offshore Nigeria, studied by Dupuis et al. (2019). The studied features of the mud volcanoes MVa and MVb are highlighted by the magenta surfaces Sa1 to Sb3. The Insets 1–2 show the frequency spectra

(black curve) within the areas (white boxes) below and on the flanks of MVa, respectively. The maps include: i) and ii) two-way time map of the seafloor (in color) with gradient overlain on it and indicating the location of mud volcanoes based on Dupuis et al. (2019). Mud volcanoes MVa, MVb and MVc are the three mud volcanoes studied in this Chapter, and iii) map of seafloor amplitudes.

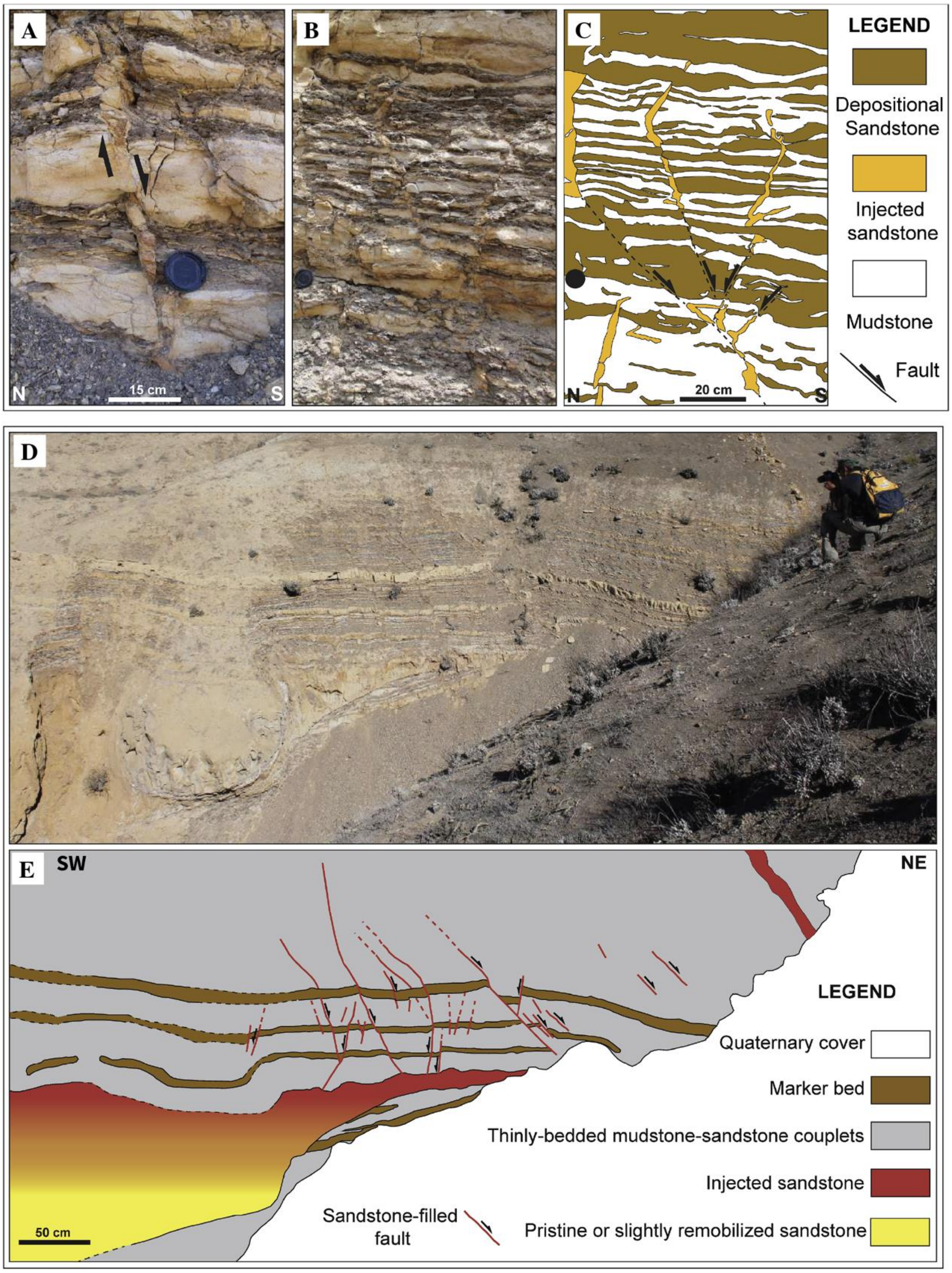

Figure 6 Examples of sand-filled normal faults (SFNF) from the Panoche/Tumey hills area in California. A) The photo shows Type 1 SFNF in the Tumey Gulch area, namely: a) SFNF with centimetre-scale offsets and openings of a few centimetres. b) Field photograph and c) associated line drawing of conjugate sets of Type 1 SFNF with centimetre-scale

offsets. In the photos, faults die out upwards over tens of centimetres, and the overlying layers are undeformed. The anomalous curvatures observed in some of the fault planes are related to ‘post-emplacement’ compaction. B) Overview of Type 1 SFNF from in the Tumey Gulch area (Outcrop O2). The figure shows: a) Panoramic photo and b) corresponding line drawing of a SFNF array overlying a remobilized turbidite sandstone body. Once again, the anomalous curvature shown by the fault planes is mainly due to ‘post-emplacement’ deformation processes. Figures are modified from Palladino et al. (2018).

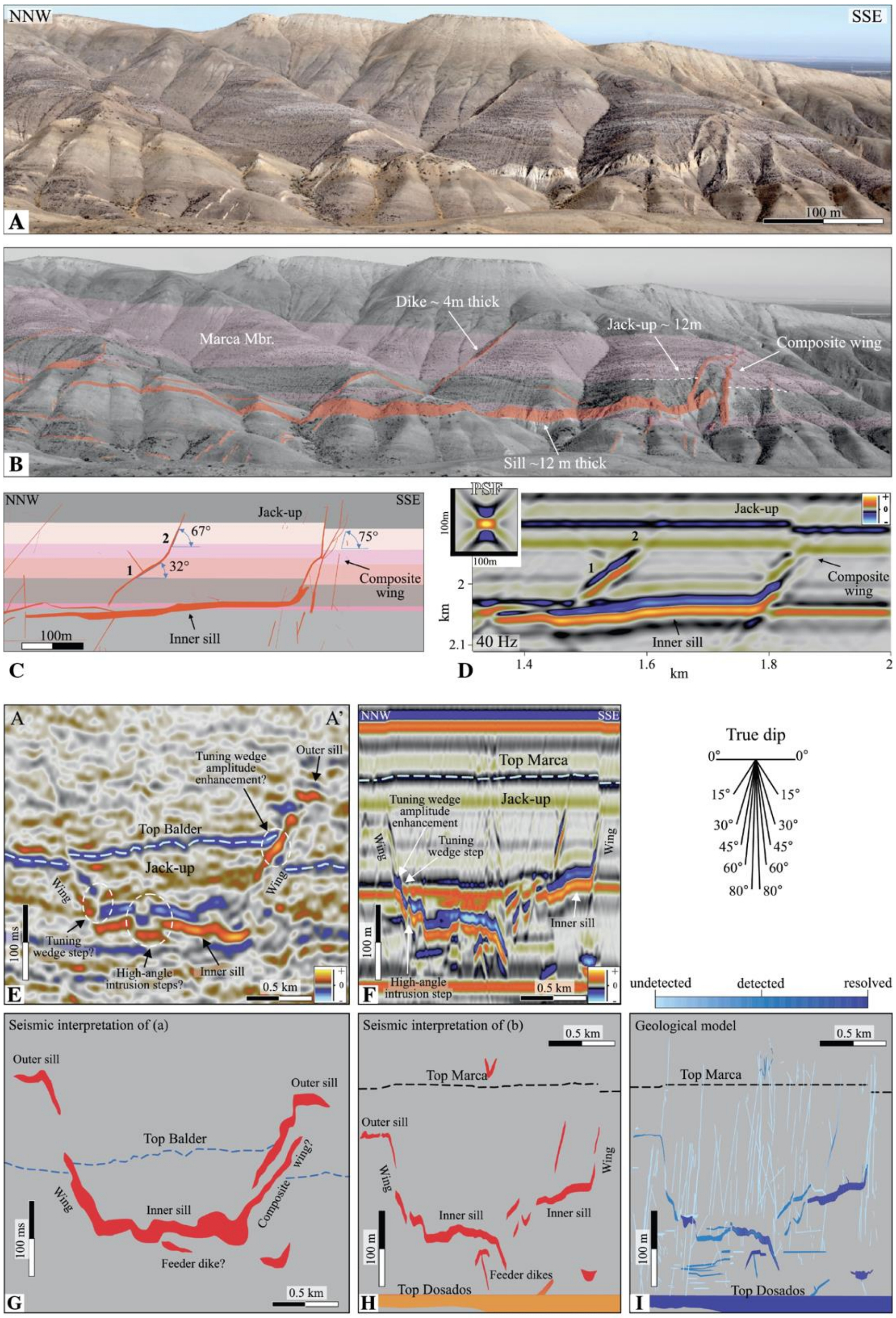

Figure 7 Complex geometries and imaging of sandstone intrusions as detailed in Grippa et al. (2019) based on information from Central California, USA. A) The figure shows part of the Right Angle Canyon in the Panoche hills area: a) detail of the southern wing of the Right Angle Canyon (RAC) and portion of the southern inner sill. b) Geological interpretation of the photo shown in a) highlighting how discordant is the sandstone intrusion and the overall

jack-up of the overlying mudstone. c) Geological model of the southern RAC wing. d) Synthetic seismic model of the southern wing using a zero-phase Ricker wavelet with a peak frequency of 40 Hz to convolve the reflectivity model. B) Comparison of actual seismic data of sandstone intrusions with synthetic data in which the horizontal and vertical scales are approximately equal. a) Seismic section through a saucer-shaped sandstone intrusion in the Volund field, Norwegian North Sea (Huuse et al., 2004, Schwab et al., 2014). Note that emplacement of the inner sill causes the jack-up of the overlying strata, as also shown in the outcrop photos above. Dashed white ovals highlight the occurrence of steps within the inner sill reflections and at the base of the wing reflection, as well as amplitude enhancement effect. b) The 40 Hz synthetic seismic section from the RAC shown above displaying a similar geometry to the Volund section. c) Seismic interpretation of a) showing the main sandstone intrusion features on seismic data. d) Seismic interpretation of b) showing the geometry of the saucer-shaped intrusion as a seismic interpreter would see them. e) Geological model of the RAC showing its high number of high-angle sandstone intrusions, which are unlikely to be detected by a seismic survey.

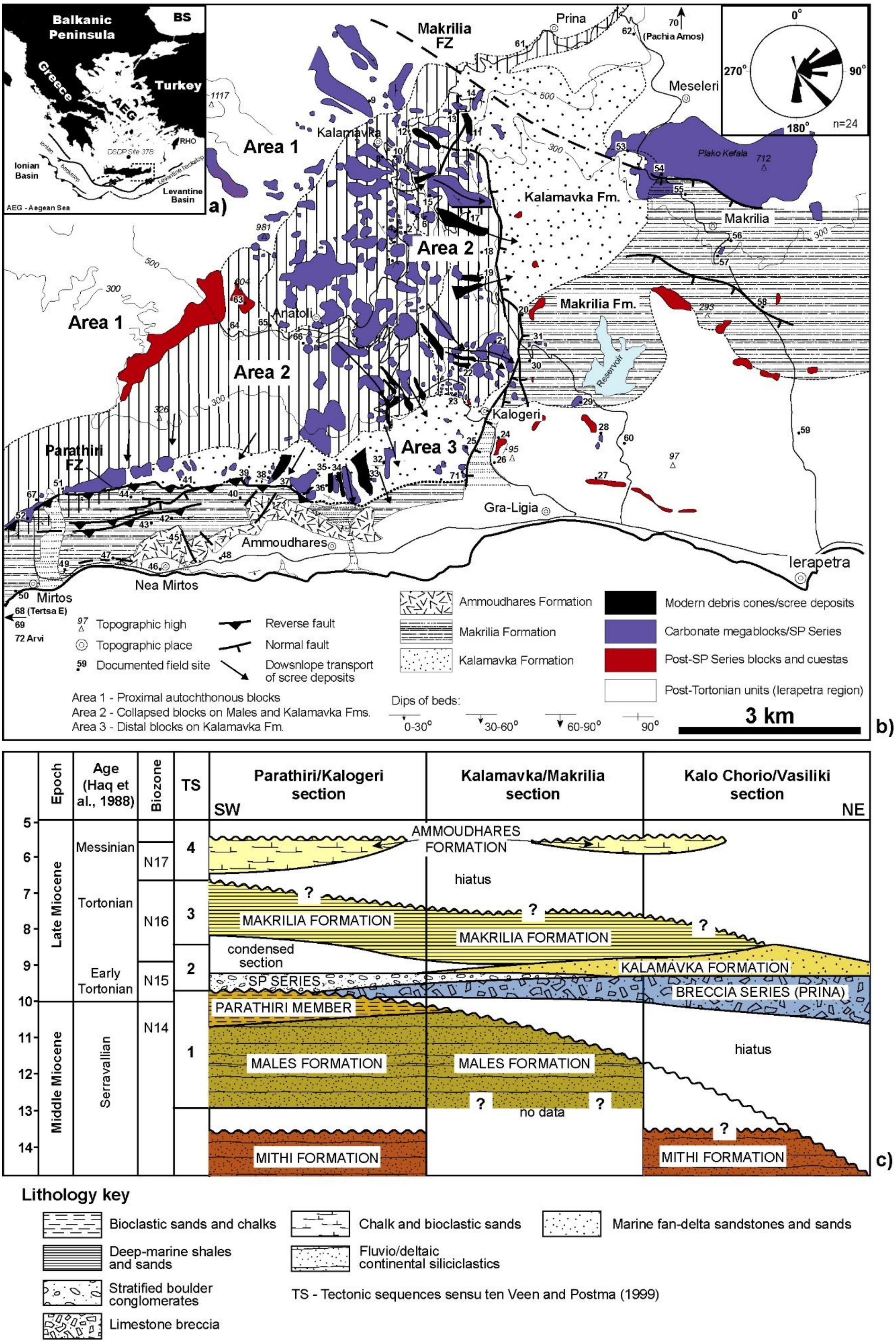
Balkanic Peninsula
BS
Greece
Turkey
AEG
Ionian Basin
Levantine Basin
DSDP Site 378
RHO
AEG - Aegean Sea
a)
Makrilia FZ
Prina
70 (Pachia Amos)
Meseleri
Kalamavka
Area 1
Area 2
Area 3
Kalamavka Fm.
Makrilia
Makrilia Fm.
Plako Kefala
Anatoli
Reservoir
Kalogeri
Parathiri FZ
Gra-Ligia
Ammoudhares
Nea Mirtos
Mirtos
Ierapetra
68 (Tertsa E)
69
72 Arvi
0°
90°
180°
270°
n=24
Topographic high
Topographic place
Documented field site
Reverse fault
Normal fault
Downslope transport of scree deposits
Ammoudhares Formation
Makrilia Formation
Kalamavka Formation
Modern debris cones/scree deposits
Carbonate megablocks/SP Series
Post-SP Series blocks and cuestas
Post-Tortonian units (Ierapetra region)
Area 1 - Proximal autochthonous blocks
Area 2 - Collapsed blocks on Males and Kalamavka Fms.
Area 3 - Distal blocks on Kalamavka Fm.
Dips of beds:
0-30°
30-60°
60-90°
90°
3 km
b)
Epoch
Age (Haq et al., 1988)
Biozone
TS
Parathiri/Kalogeri section
Kalamavka/Makrilia section
Kalo Chorio/Vasiliki section
SW
NE
Late Miocene
Middle Miocene
Messinian
Tortonian
Early Tortonian
Serravallian
N17
N16
N15
N14
AMMOUDHARES FORMATION
hiatus
MAKRILIA FORMATION
condensed section
KALAMAVKA FORMATION
SP SERIES
BRECCIA SERIES (PRINA)
PARATHIRI MEMBER
MALES FORMATION
no data
MITHI FORMATION
c)
Lithology key
Bioclastic sands and chalks
Chalk and bioclastic sands
Marine fan-delta sandstones and sands
Deep-marine shales and sands
Fluvio/deltaic continental siliciclastics
Stratified boulder conglomerates
TS - Tectonic sequences sensu ten Veen and Postma (1999)
Limestone breccia

Figure 8 General map of SE Crete’s slide blocks modified from Alves (2015). The small map in (A) shows the location of the investigated slope successions in SE Crete. In the geological map of SE Crete’s palaeoslope shown in (B), Area 1 comprises autochthonous carbonate blocks and breccia–conglomerates showing limited gravitational collapse. Area 2 comprises disrupted deep-water (carbonate) fan cones, carbonate megabreccias and boulder conglomerates. Area 3 includes carbonate fan cones, collapsed blocks, and minor debris-flow deposits (boulder conglomerates) deposited in distal regions of the palaeoslope. (C) Stratigraphic panel for SE Crete, where a tectonic trough (Ierapetra Basin) was subject to extensional and transtensional movements since, at least, the end of the Serravalian. The stratigraphic panel is modified from Postma and Drinia (1993) and van Hinsbergen and Meulenkamp (2006). SP-Stratified Prina Series.

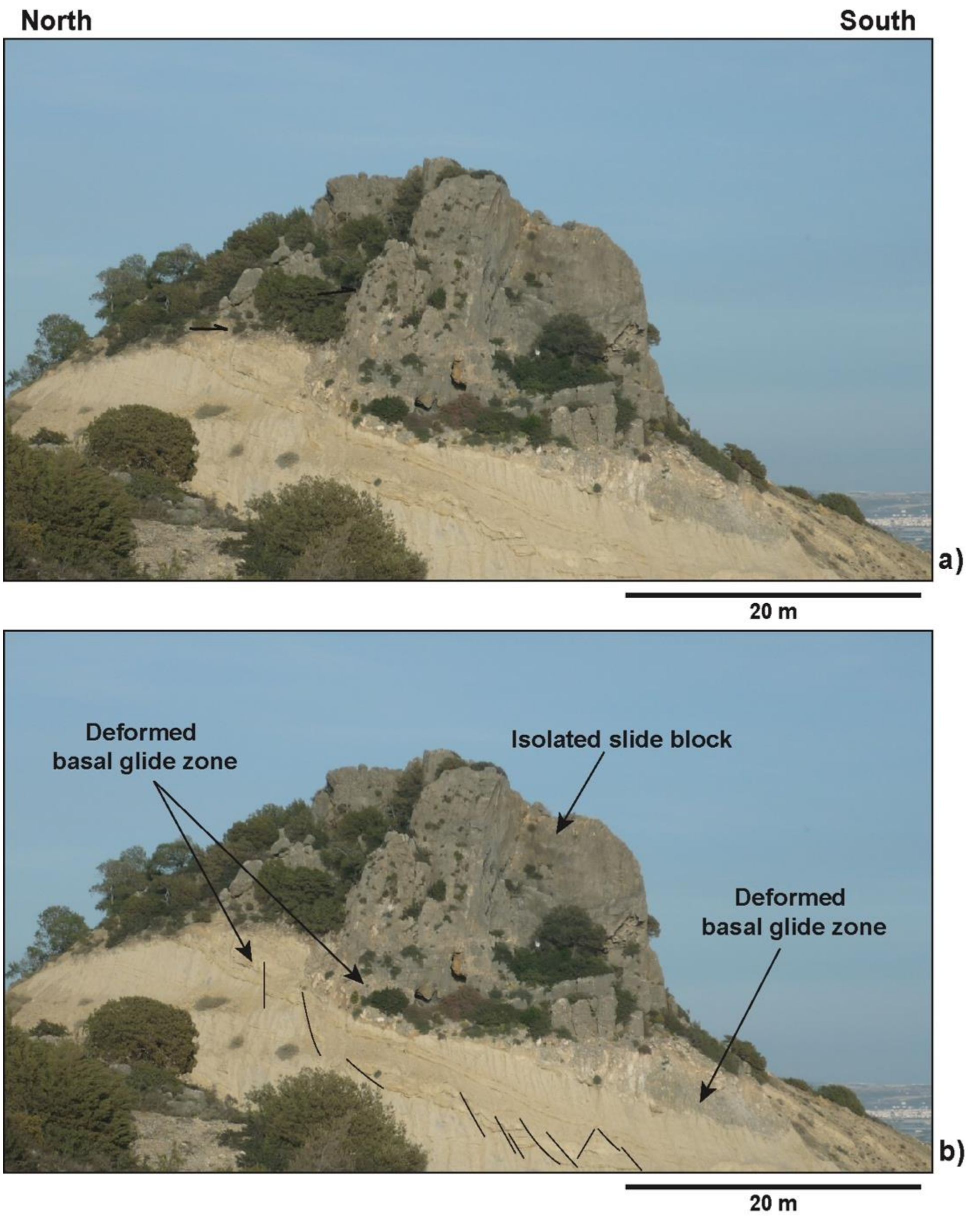

Figure 9 Collapsed slide block at Location 33 in Figure 8A, showing associated basal features. Note the dual character of the basal shear zone at this location 33 - up to 2 m of coarse immature breccias occur below the slide block and change abruptly into in a sandier deformed area with slope siliciclatic (sandy) material. The thickness of the basal glide zone reaches more than 4 metres in its thickest zone.

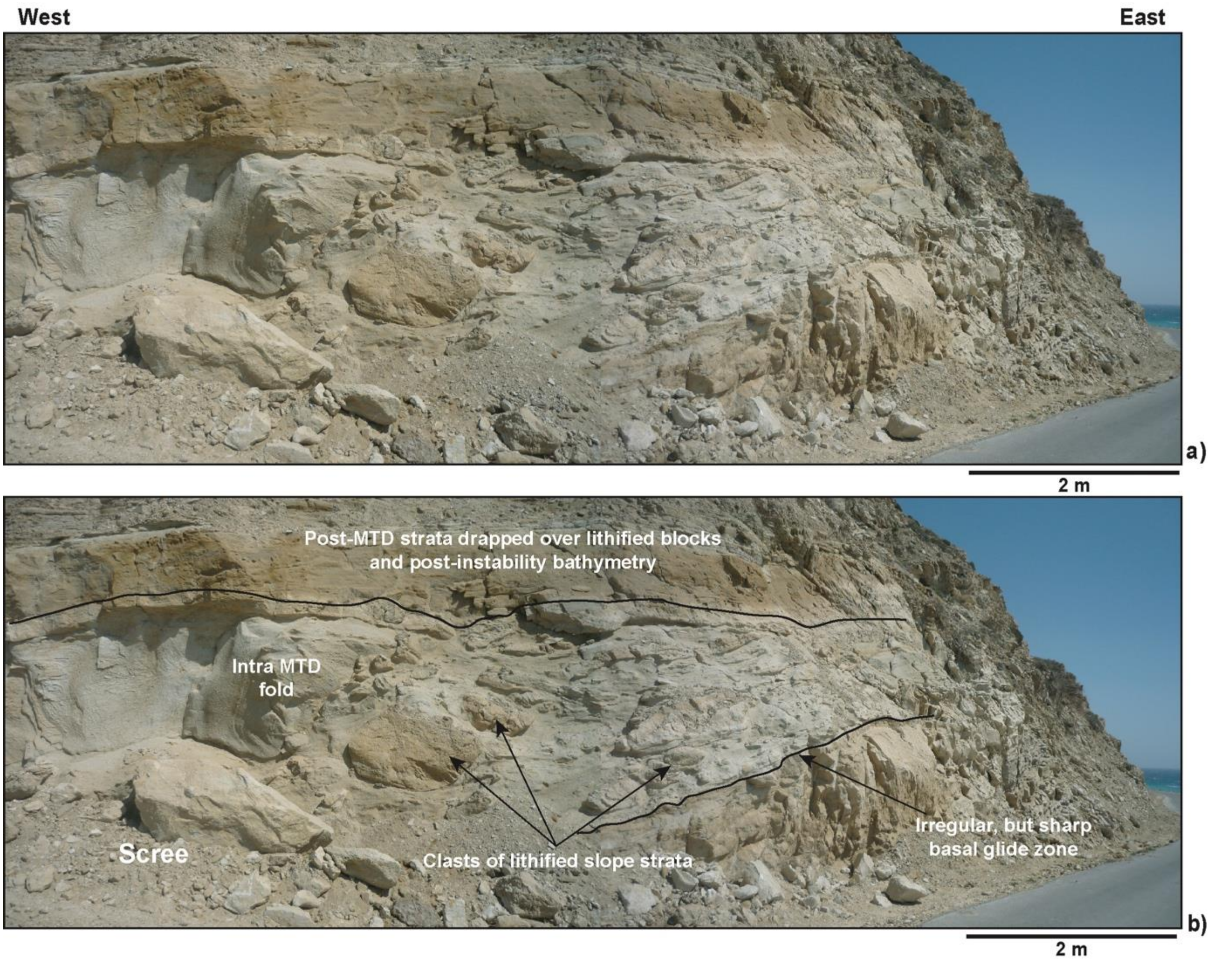

Figure 10 Detail of a sandy MTD in the Ammoudhares Formation near Location 50 in Figure 8A. Note the complex arrangement of siliciclastic material and small blocks within the imaged MTD, in which internal folding (slumps) alternate with lithified blocks of sediment. The basal glide zone is sharp and very thin (<30 cm) in this location.

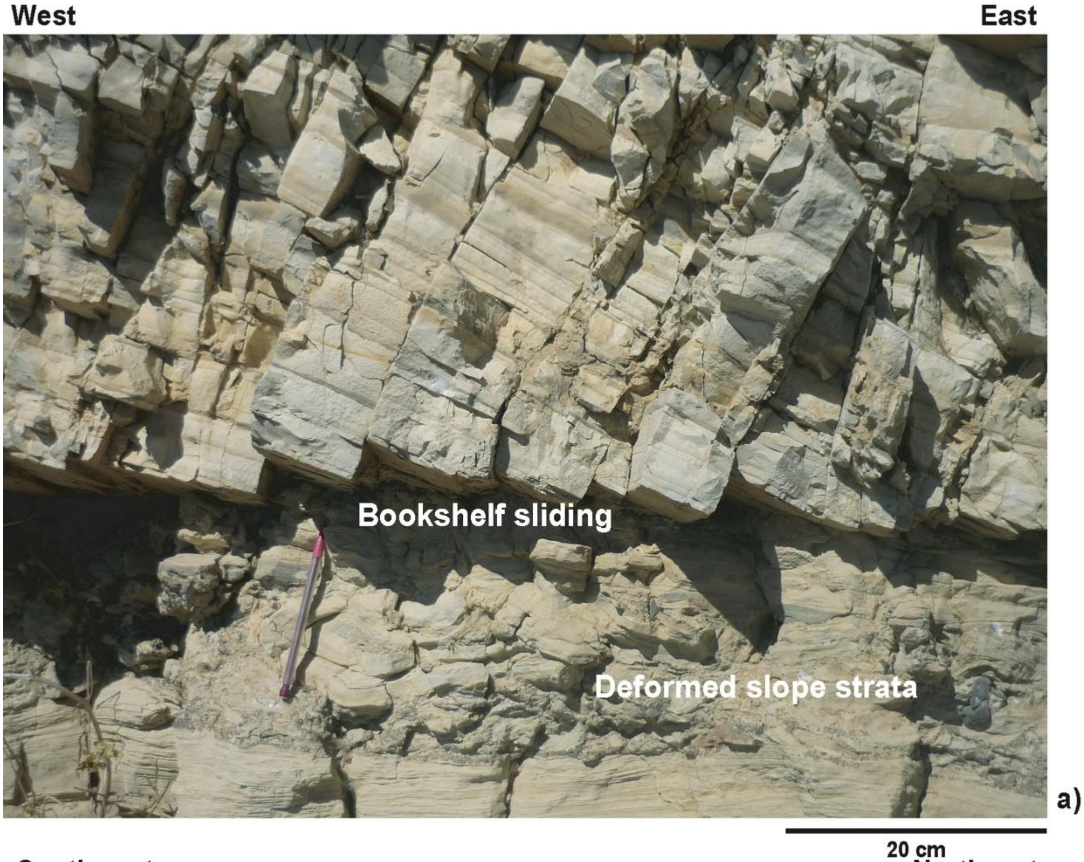
West
East
Bookshelf sliding
Deformed slope strata
a)
20 cm

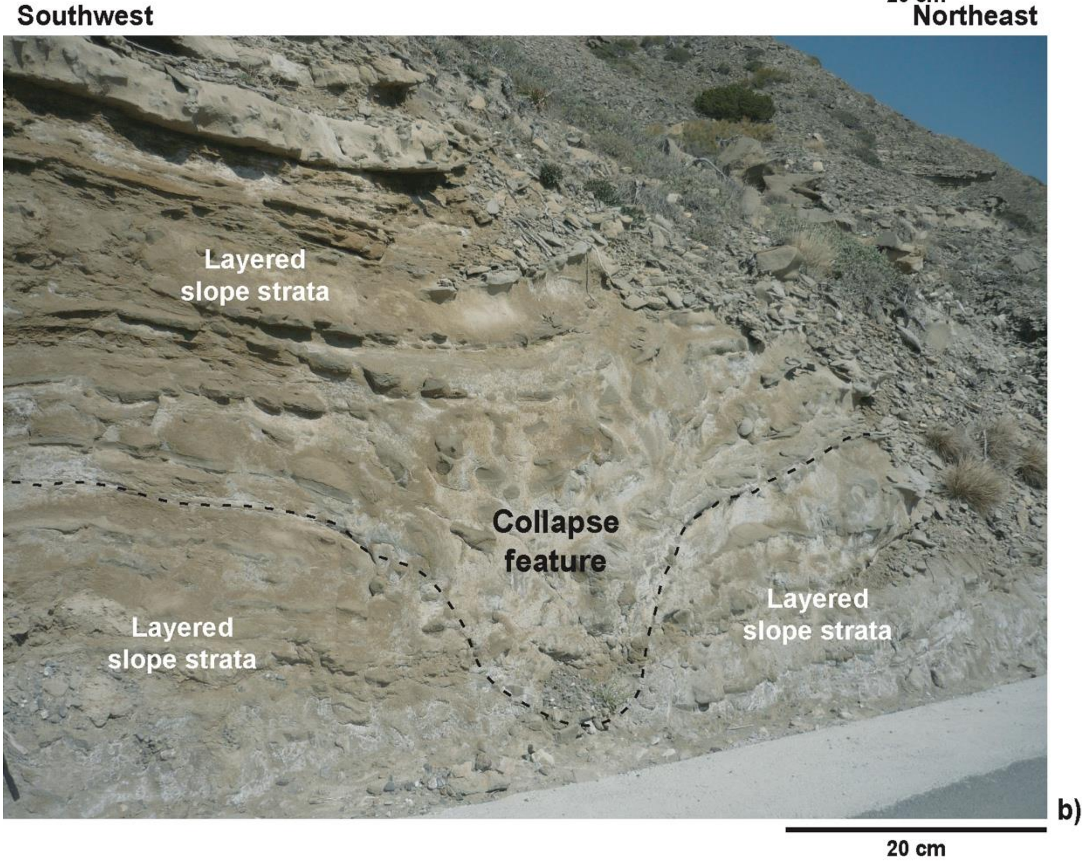
Southwest
Northeast
Layered slope strata
Collapse feature
Layered slope strata
Layered slope strata
b)
20 cm

Figure 11 A) Example of bookshelf sliding of slope strata at Location 12 in Figure 8A. This type of sliding may have occurred post-depositionally by the readjustment of the paleo-slope to tectonic oversteepening or local overpressure increase. B) Collapse feature near Location 68 in Figure 8a. Here, tectonic oversteepening and withdrawal of soft slope strata may have caused the local collapse feature imaged in the photograph. The depositional facies suggest the strata in this photo belong to the Makrilia Formation (see Figure 8B), though very similar to Ammoudhares facies.

West East

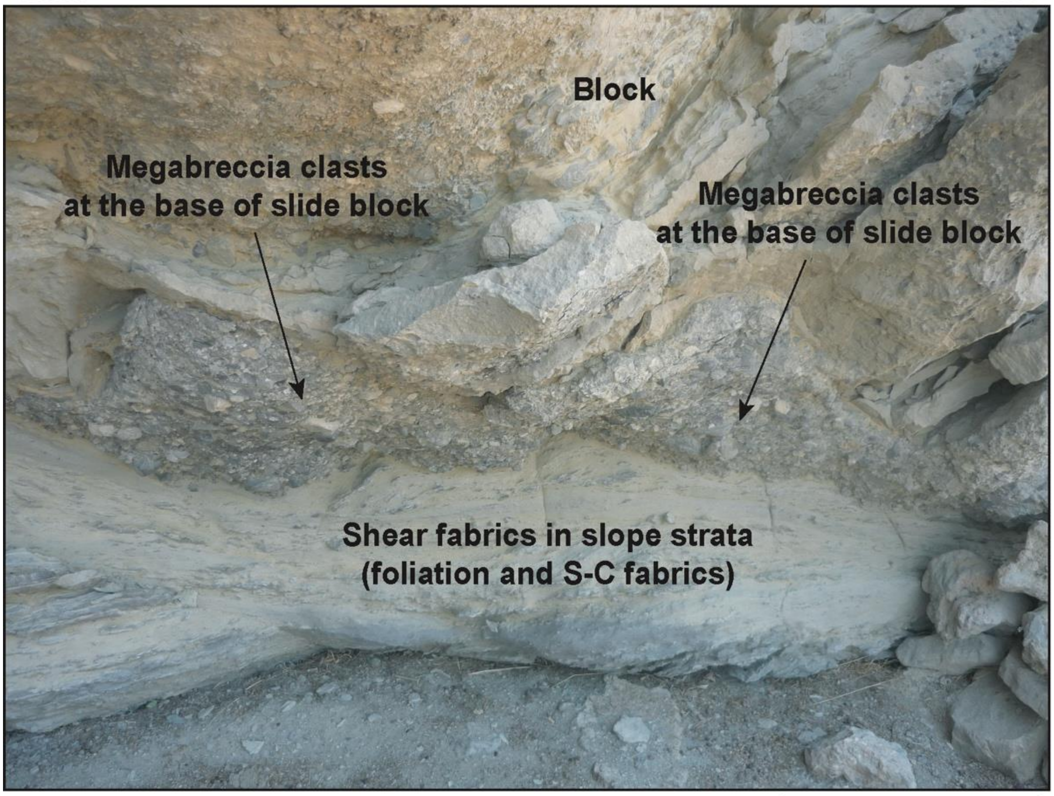

1 m

West East

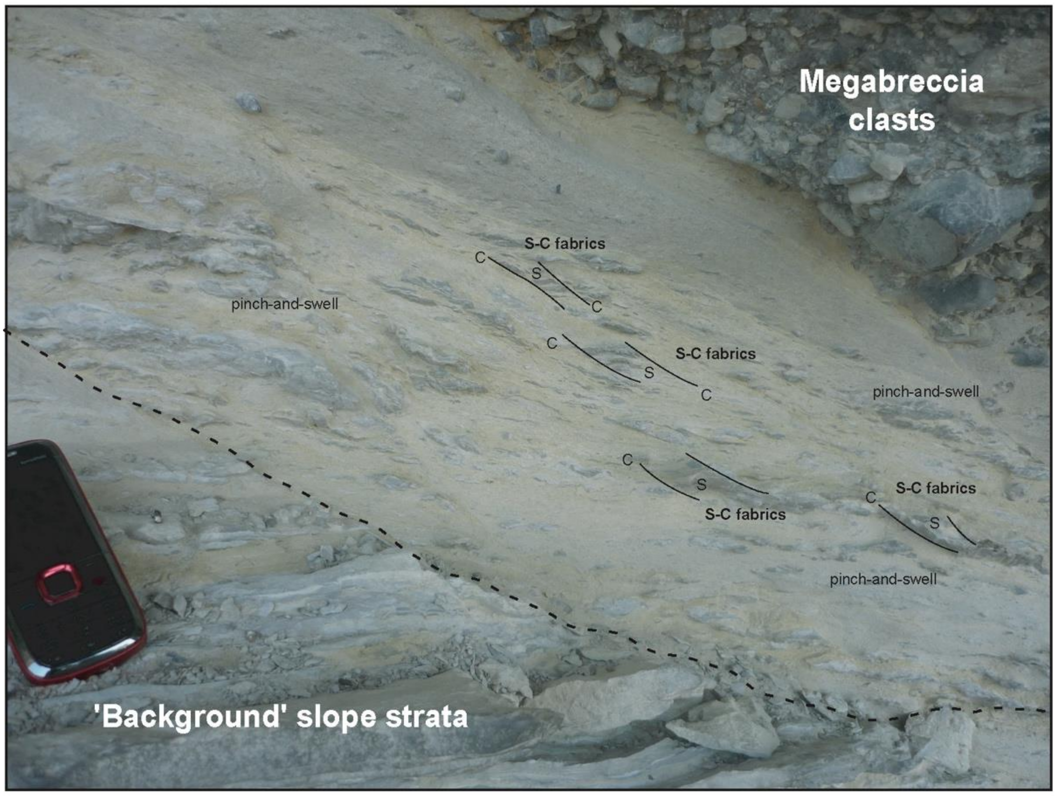

50 cm

Figure 12 Detailed examples of soft-sediment deformation in the basal shear zones of blocks, Location 11 (Figure 8A). A) Local carbonate megabreccias below a 20 m-thick block. B) Foliated slope strata with local S-C fabrics indicating that the transport direction of the block above is to the right (east).

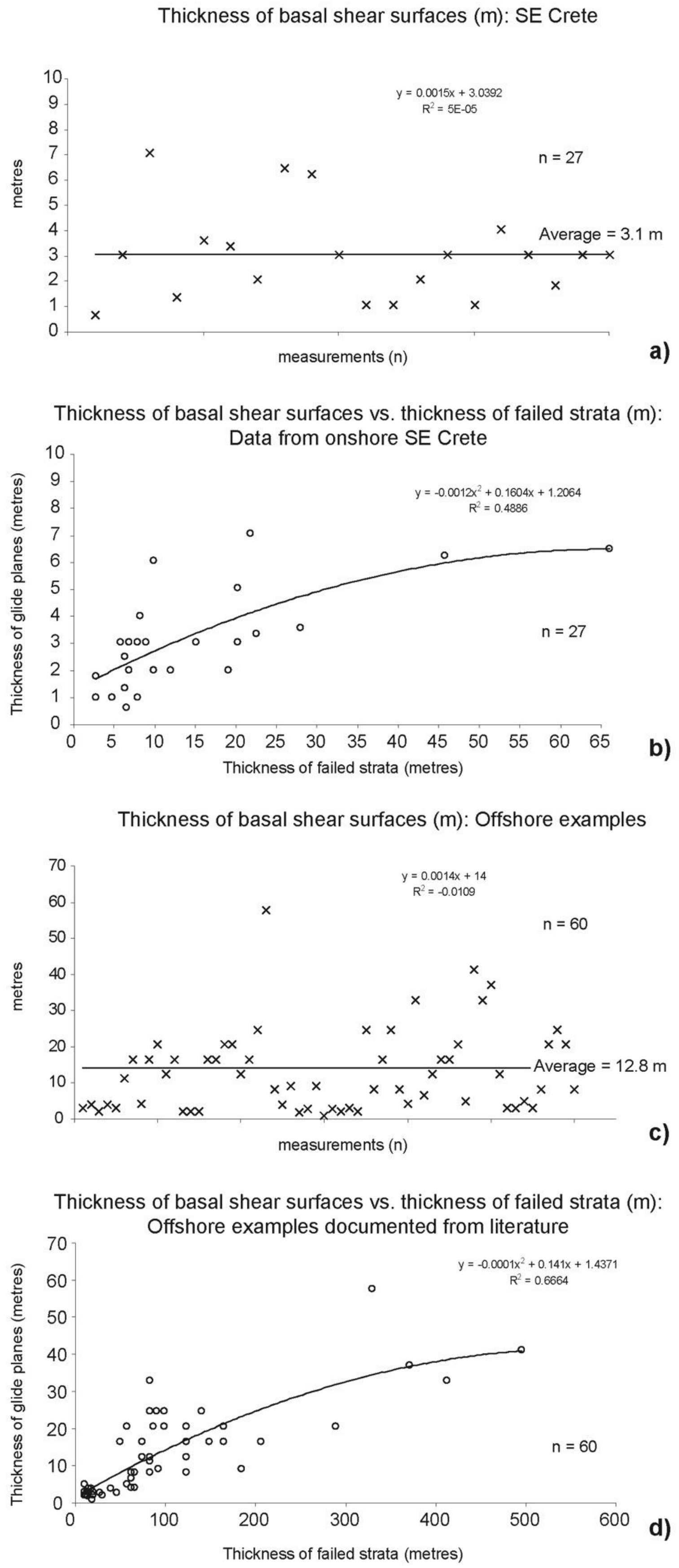
Thickness of basal shear surfaces (m): SE Crete
y = 0.0015x + 3.0392
R^2 = 5E-05
n = 27
Average = 3.1 m
metres
measurements (n)
a)
Thickness of basal shear surfaces vs. thickness of failed strata (m): Data from onshore SE Crete
y = -0.0012x^2 + 0.1604x + 1.2064
R^2 = 0.4886
n = 27
Thickness of glide planes (metres)
Thickness of failed strata (metres)
b)
Thickness of basal shear surfaces (m): Offshore examples
y = 0.0014x + 14
R^2 = -0.0109
n = 60
Average = 12.8 m
metres
measurements (n)
c)
Thickness of basal shear surfaces vs. thickness of failed strata (m): Offshore examples documented from literature
y = -0.0001x^2 + 0.141x + 1.4371
R^2 = 0.6664
n = 60
Thickness of glide planes (metres)
Thickness of failed strata (metres)
d)

Figure 13 Graphs showing the scale relationships between the thicknesses of failed strata above vs. the thickness of basal shear zones (R ratio). Measurements were taken from several authors as described in Alves and Lourenço (2010) and Alves (2015) - Hampton et al. (1996), Gardner et al. (1999), Gee et al. (1999), Gee et al. (2006), Gee et al. (2007), DePlus et al. (2001), Bohannon and Gardner (2004), Haflidason et al. (2004), Lee (2005), Frey-Martinez et al. (2006), Greene et al. (2006), Lee et al. (2006), Vanneste et al. (2006), Hjelstuen et al. (2007), Minisini et al. (2007), Normarck et al. (2007), Sultan et al. (2007), Bull et al. (2008), Moscardelli and Wood (2008b), Alves and Cartwright (2009), Alves et al. (2009).

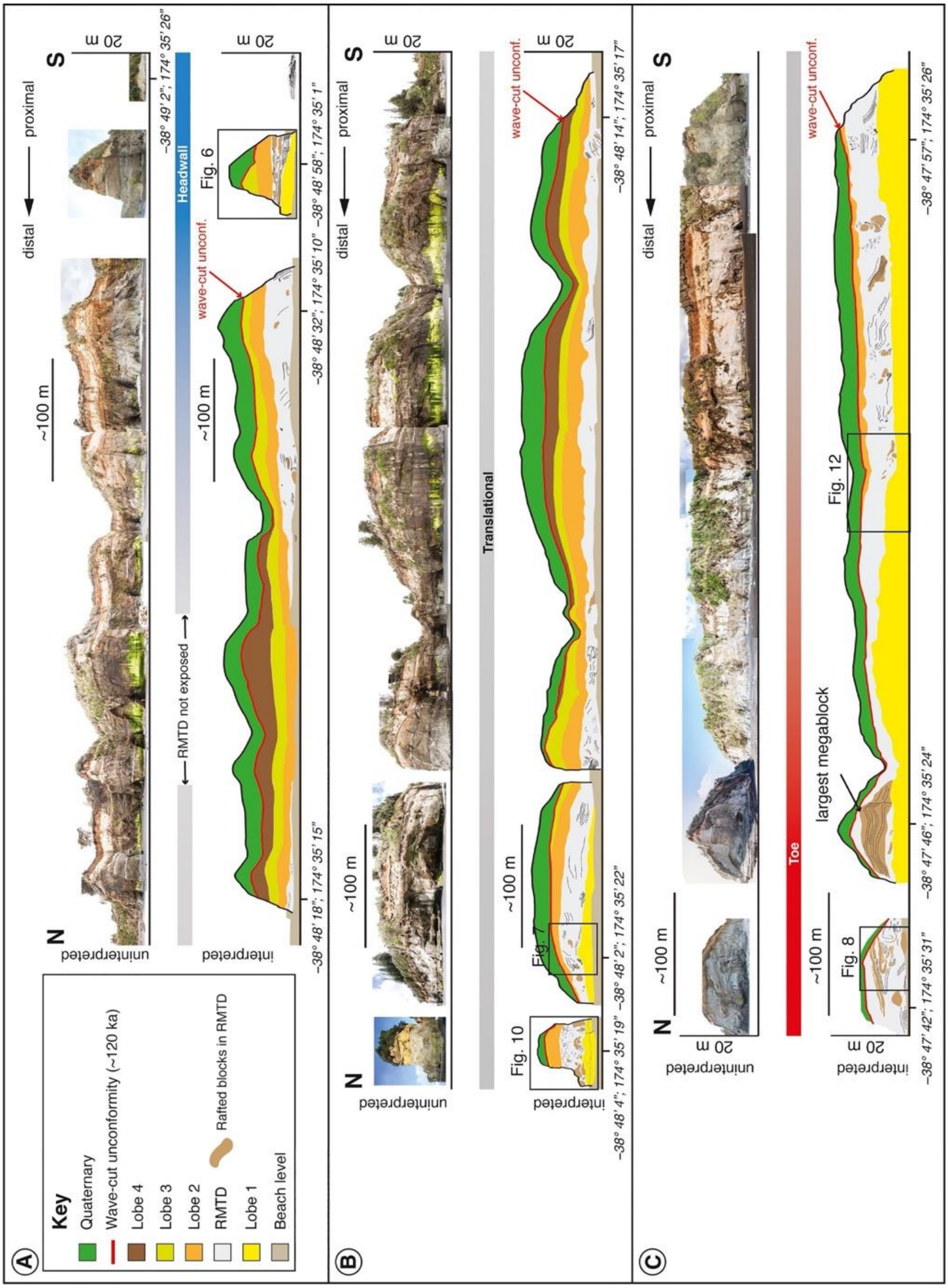

Figure 14 Photomosaic panels of the Rapanui mass transport deposit (RMTD) with approximate coordinates. Outcrops are exposed semi-obliquely to the northwest depositional

dip. See Fig. 4D for the approximate map location for each panel. The RMTD is sandwiched betweeb two sandstone units interpreted as submarine fan lobes and here informally labelled as Lobe 1 and Lobe 2. Slide blocks inside the RMTD have been traced to scale. A) Uninterpreted (above) and interpreted (below) panel covering part of the headwall into the translational domain. B) Uninterpreted (above) and interpreted (below) panel in the translational domain. Note the increase in slide blocks inside the RMTD matrix. C) Uninterpreted (above) and interpreted (below) panel covering part of the translational into the toe domain. Here, the upper contact of the RMTD is sharply truncated by the Rapanui wave cut unconformity.

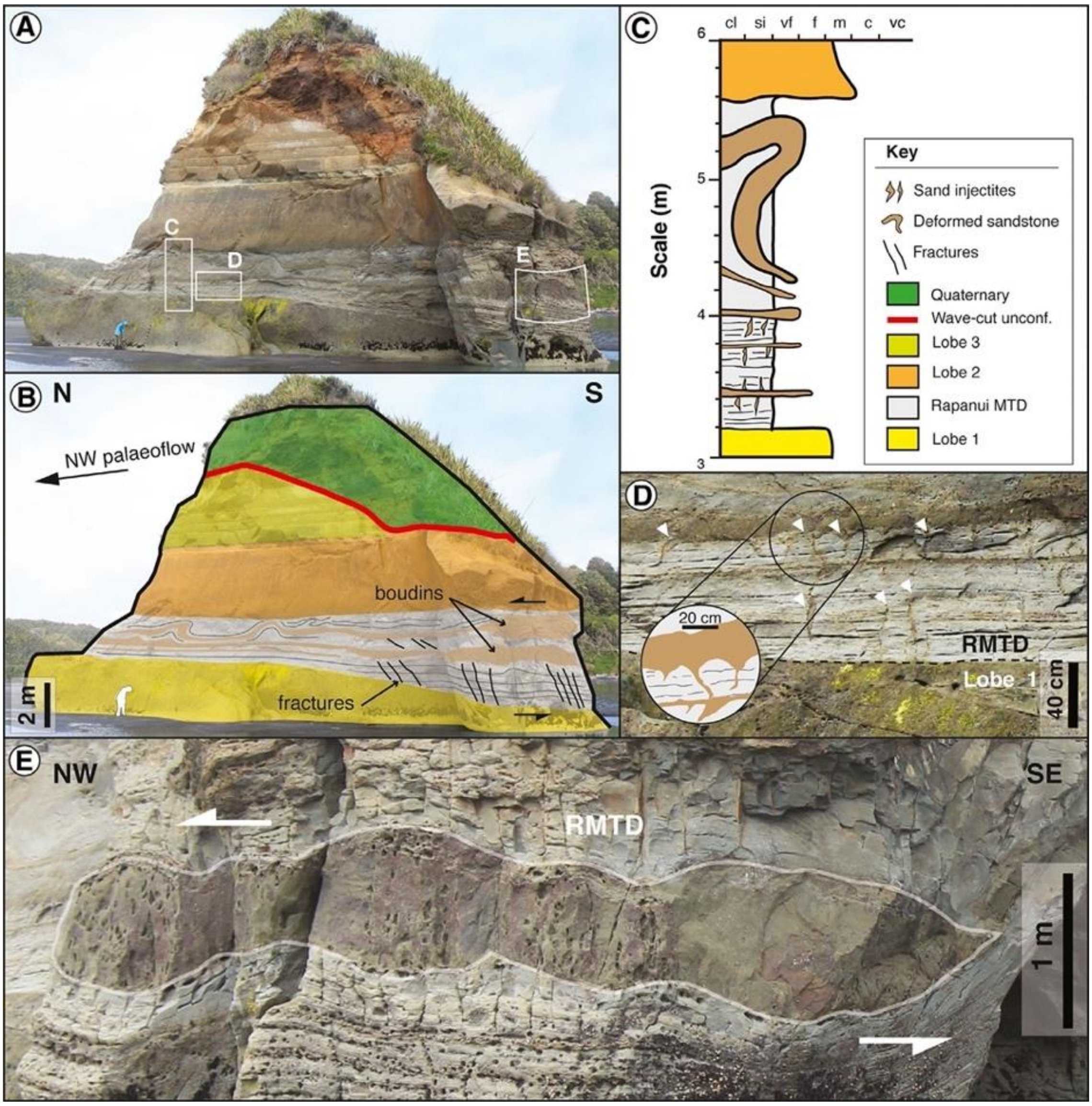

Figure 15 A) Uninterpreted and (B) interpreted key outcrop in the headwall domain of the Rapanui mass transport deposit (RMTD) – see Figs 4D and 5A for location. Note that deformation structures within the RMTD are associated with extensional stress and comprise fractures, boudinage and clastic injectites. However, deformation did not completely obliterate the original stratification of the RMTD 'protolith'. Fractures abruptly stop against thick sandstone layers and substratum. C) Representative stratigraphic measured section in the headwall of the RMTD. Note that sandstone beds deformed plastically (presenting, for example, folds and boudinage) but disaggregation is minor. D) Close up of the sand injectites

in the RMTD. These cuspidate injectites (white triangles) have lengths around 10 to 20 cm and form during sudden dilation of brittle beds (i.e. sandstone). The contact between the RMTD and the underlying deposits (Lobe 1), marked with the dashed line, is sharp and deformation is limited within the RMTD. E) Close-up of metre-scale, shear-band boudin in a thick sandstone bed. This type of boudinage is associated with ductile deformation and large lateral displacement. Boudins only formed in the sandstone beds and can be used to estimate shear sense (see white arrows).

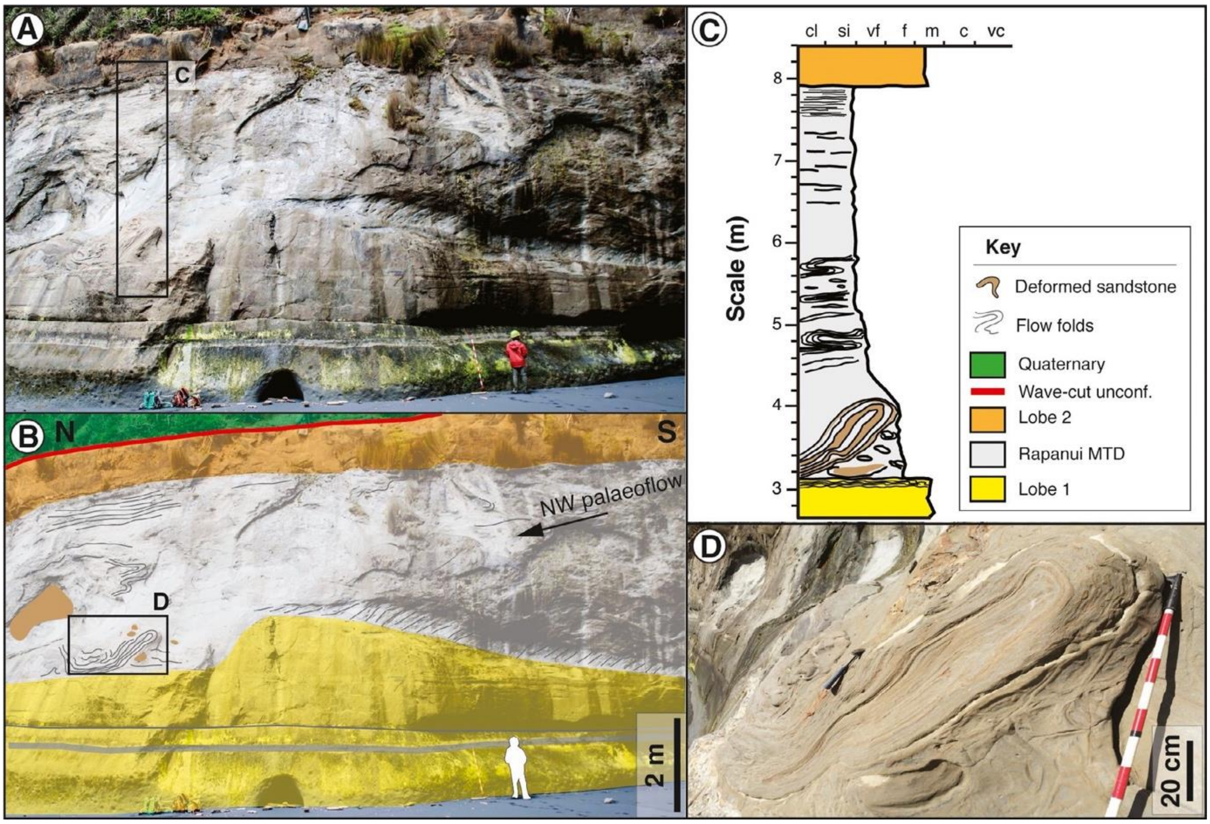

Figure 16 A) Uninterpreted and (B) interpreted key outcrop in the translational domain of the Rapanui mass transport deposit (RMTD) – see Figs. 4D and 5B for location. Note the homogenization/stratal disruption of the RMTD matrix; nearly all primary bedding/stratification has been completely obliterated. Slide sandstone blocks are present in the matrix and some blocks show disaggregation (see Fig. 10). The basal shear zone here is irregular and shows evidence of entrainment and fluidization (see partially fluidized and

folded sandstone from substratum in the close-up in (D). Flow folds or flowage structures are identified in the matrix resulting from partial to complete fluidization conditions (viscoplastic nature) during mass transport. C) Representative stratigraphic measured section in the translational domain. D) Close-up of fluidized sandstone from the substratum in the basal shear zone.

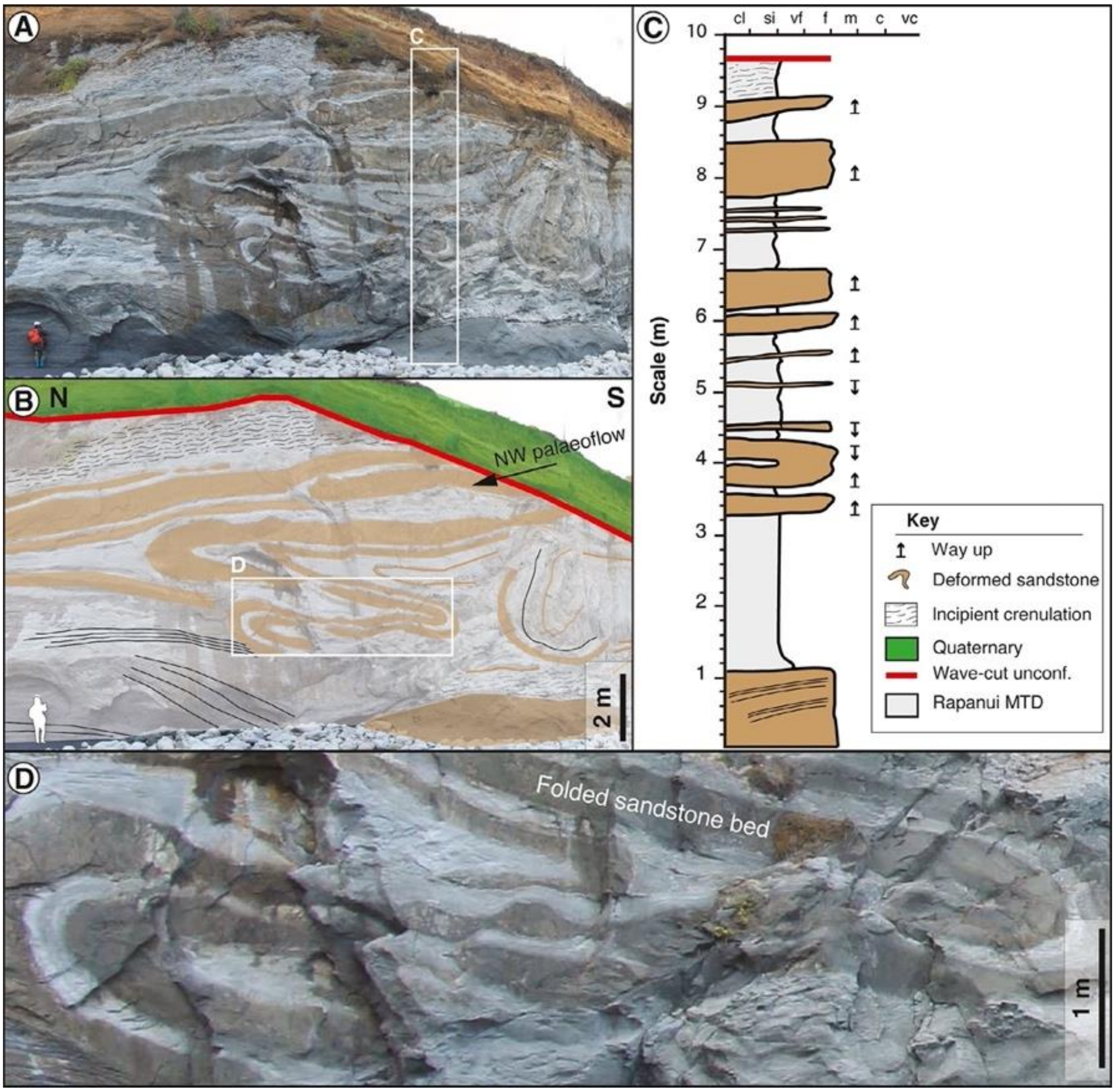

Figure 17 A) Uninterpreted and (B) interpreted key outcrop in the toe domain of the Rapanui mass transport deposit (RMTD) – see Figs 4D and 5C for location. The dominant deformation structures shown here are meter-scale compressional folds. These types of folds are probably associated with pressure ridges formed in the toe domain. Some folds display a

sheath-like geometry such as the one in the close up in (D). Matrix near hinge of folds displays an incipient crenulation. C) Representative stratigraphic measured section in the toe of the RMTD. D) Close-up of sheath fold.

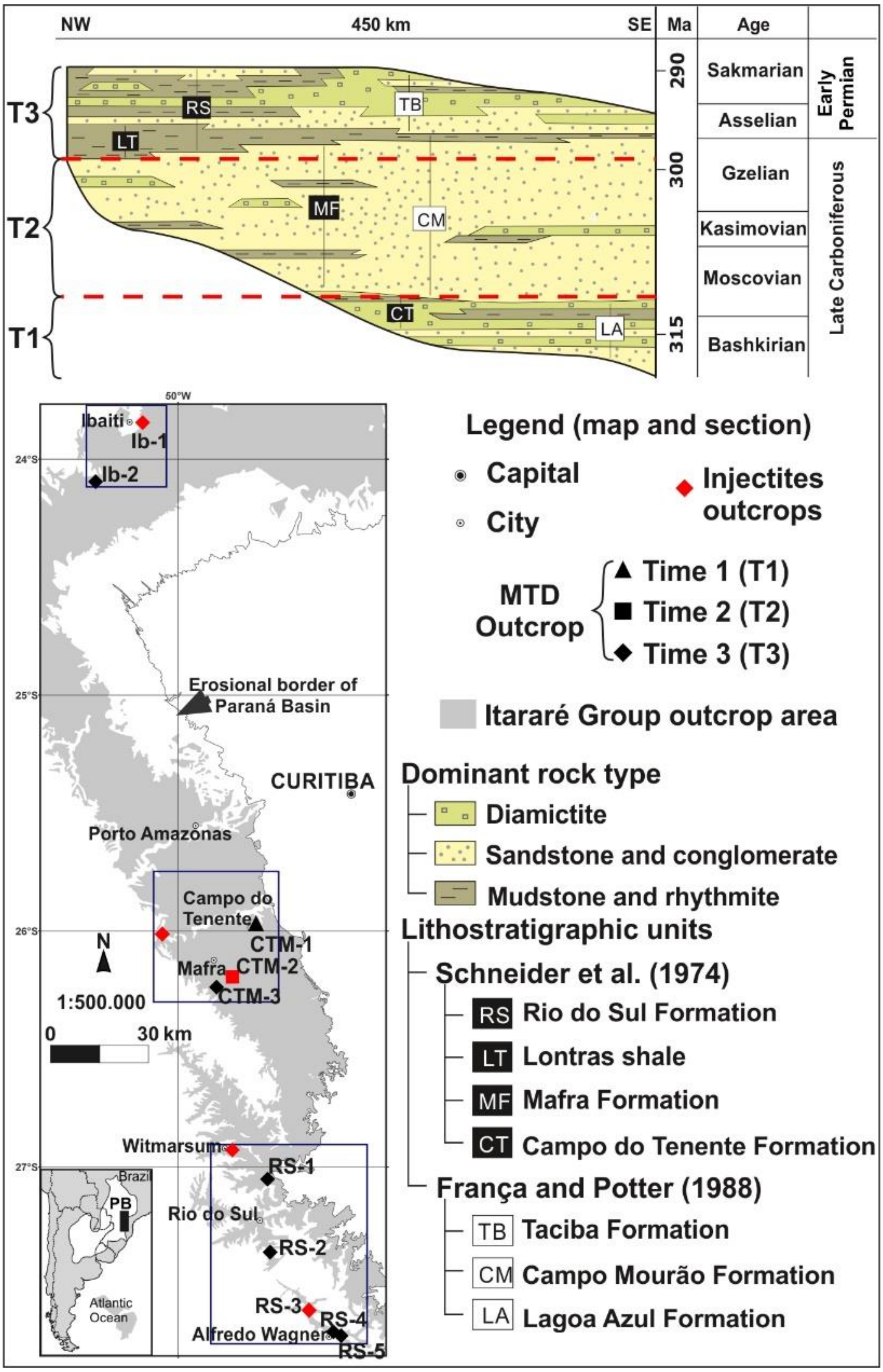

Figure 18 Location map and stratigraphic setting of MTDs cases in the Itararé Group (Paraná Basin in South Brazil) in the three areas of Ibaiti (Ib), Campo do Tenente-Mafra

(CTM) and Rio do Sul (RS). The geographic location and stratigraphic positions of each presented mass transport deposit (outcrop locality) are indicated by codes and symbols, respectively. In the outcrops indicated in red were documented sand injectites. Modified from Rodrigues et al. (2020).

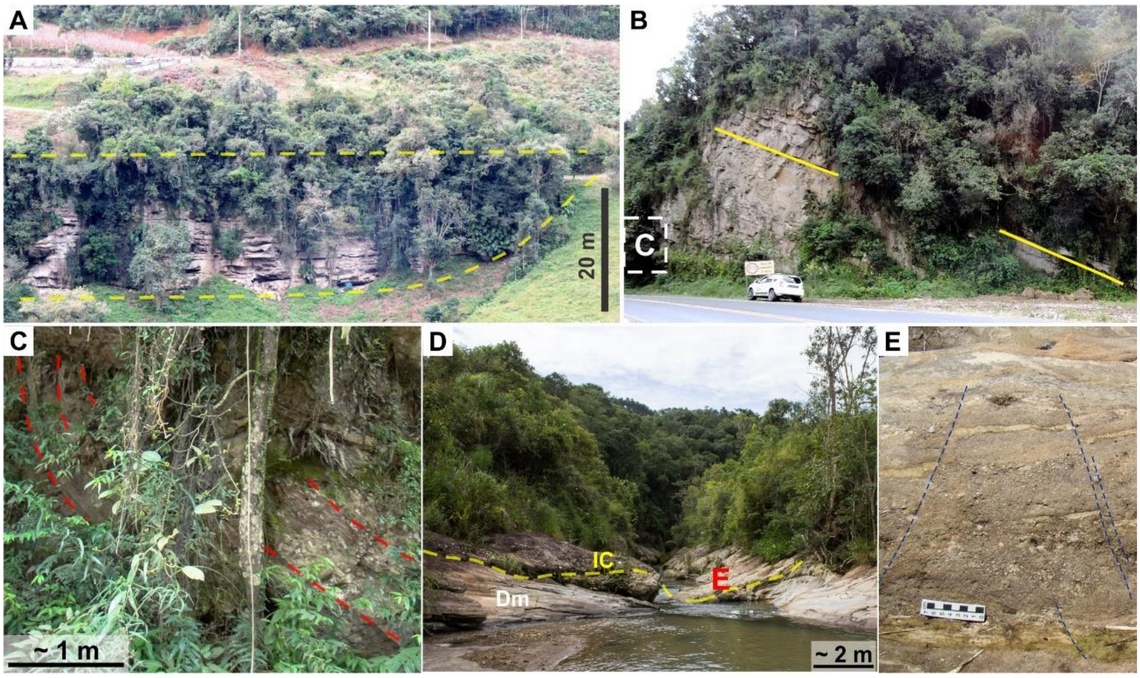

Figure 19 Large intrabasinal clasts (IC) of sandstones: A) without internal deformation (outcrop RS-5; Rodrigues et al., 2020); B) with tilted bedding (adapted from Rodrigues et al., 2020) and C) localized fold (outcrop RS-4); D) resting on banded diamictite (Dm; outcrop Ib-1) and E) internally deformed by normal faults.

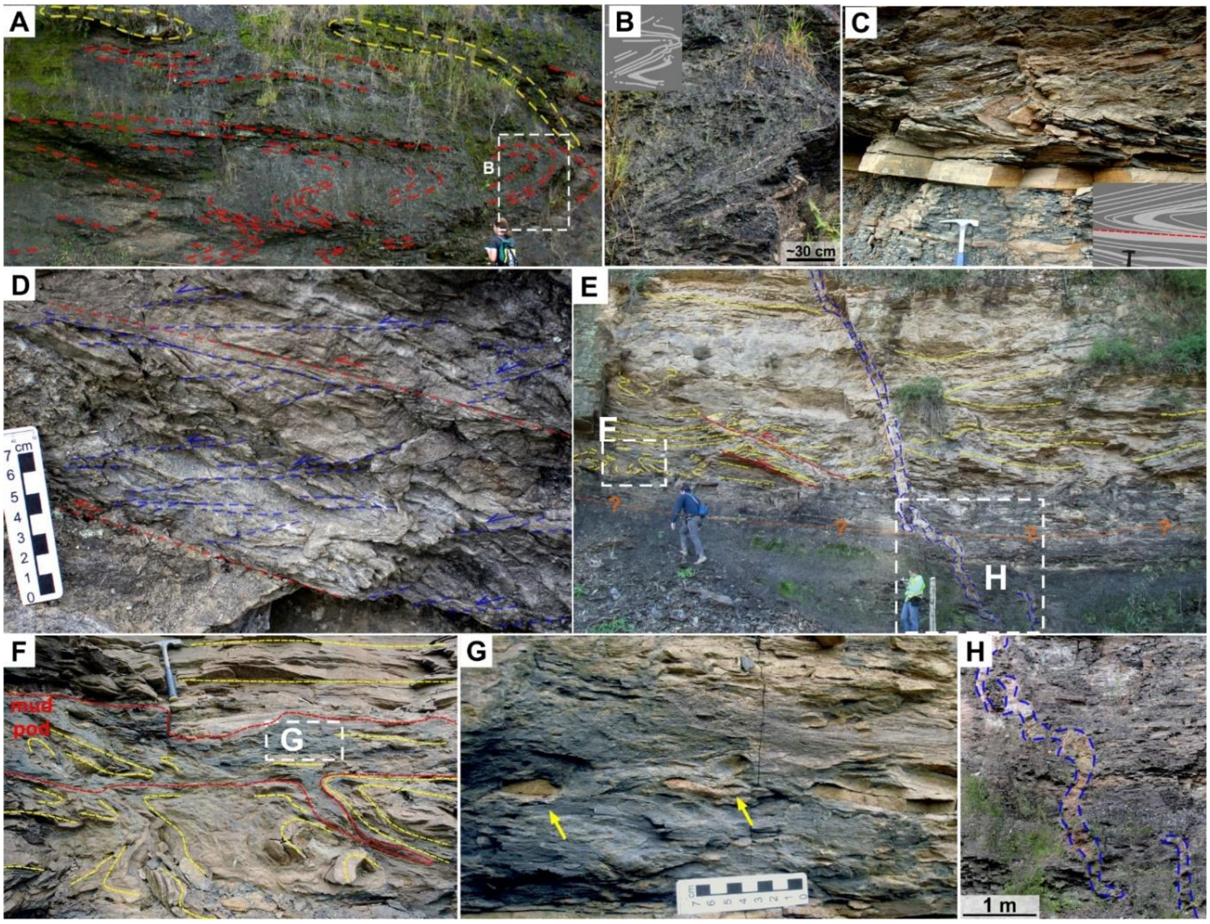

Figure 20 MTDs in outcrops RS-1 (A to C) and RS-3 (D to K) that exemplify slides/slumps cases in the Itararé Group. MTD outcrop RS-1: A) Interval of rhythmite folded with symmetric boudin at the limb of a thicker sandstone layer that is folded (adapted from Rodrigues et al., 2020); B) Detail of recumbent folds; and C) Recumbent folds with hinge thickening in thicker sandstone layers, next to the bottom of the MTD (possible detachment surface indicated by the red dashed line) (Rodrigues et al., 2020). Lower MTD in outcrop RS-3: D) normal faults associated to subhorizontal or low-angle inverse faults in rhythmite. Upper MTD in outcrop RS-3: E) symmetric to asymmetric folds and thrust faults in a sandstone and rhythmite interval, crosscut by sand injectites with “en echelon” pattern; F) asymmetric to recumbent folds in rhythmites with mud-layers with no preserved lamination, sand-layers folded partially disrupted and pods of mud (dark gray material broadly highlighted by red dashed line; E and F adapted from Rodrigues et al., 2020); G) symmetric

boudins (indicated by yellow arrows) in limbs of folded sand layers (Rodrigues et al., 2020); H) detail of sand injectites, with partially folded aspect that possibly results from compaction that affects the upper MTD and the underlying rhythmite. Possible base limit of the upper MTD indicated by the orange dashed lines (F).

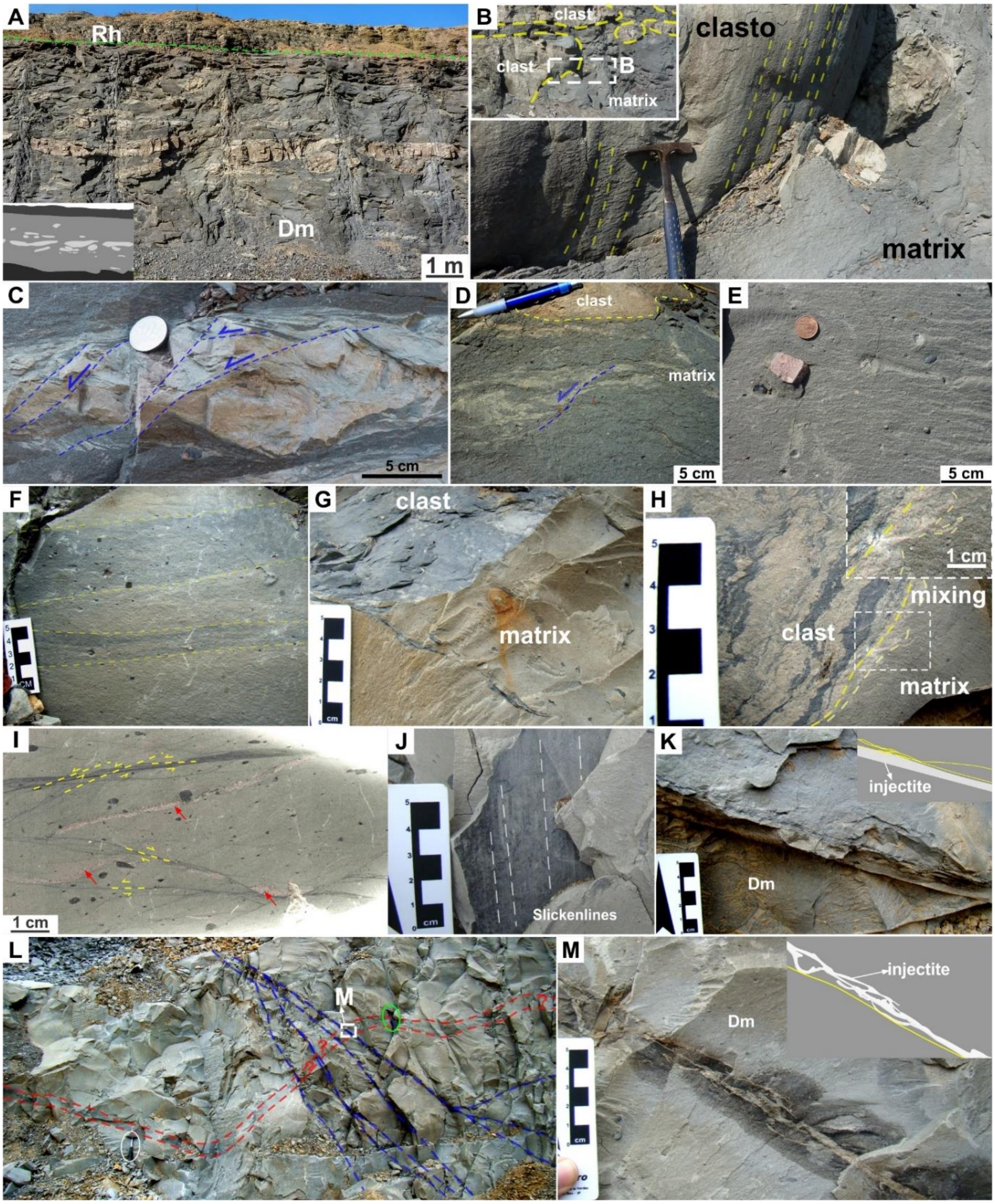

Figure 21 MTDs in outcrops CTM-1 (A to E) and CTM-2 (F to M) that exemplify debris flows in the Lagoa Azul and Campo Mourão formations, respectively. MTD outcrop CTM-1: Diamictite (Dm) with A) sandstone clasts deformed as symmetric boudins, with rhythmite

deposited on the top (contact approximate indicated by green dashed line) (modified from Rodrigues et al., 2020); B) these sandstone clasts formed by boudinage were subsequently deformed by grooves/stretch marks at the borders (A and B modified from Rodrigues et al., 2020); C) some sandstone clasts were deformed by normal faults and shearing at the borders forming films of sediments incorporated by the matrix, which can be heterogeneous with remnant sand laminations sheared and deformed by normal faults (D; Rodrigues et al., 2020) or massive (E; Vesely et al., 2018, Rodrigues et al., 2020). MTD outcrop CTM-2: Diamictite (Dm) with massive (homogenous) to heterogenous matrix with discrete textural/compositional banding (F; highlighted by yellow dashed lines) and mud granules dispersed (Rodrigues et al., 2020). This diamictite also shows larger deformed clasts such as mud clasts with sheared borders (G) and rhythmite clasts with internal laminations sheared and folded and with sheared borders, with mixed zones resulting from the partial incorporation of sediment clasts by the matrix (H) (Rodrigues et al., 2020). I) Clay smear faults (planes and zones) with anastomosed patterns that deform some of the sand injectites (Rodrigues et al., 2015, 2021). J) Displacement surface (dark grey surface; looking down on the plane) with slickenlines in clay smear fault (highlighted by white lines; Rodrigues et al., 2020). K) Tabular injectite parallel to clay smear fault (yellow lines in the drawing) (adapted from Rodrigues et al., 2020). L) Sand injectites subparallel to clay smear faults (highlighted by blue dashed lines) that crosscut open folds in banded matrix (highlighted by red dashed lines). M) Irregular anastomosed injectite subparallel to clay smear fault (yellow lines in the drawing).

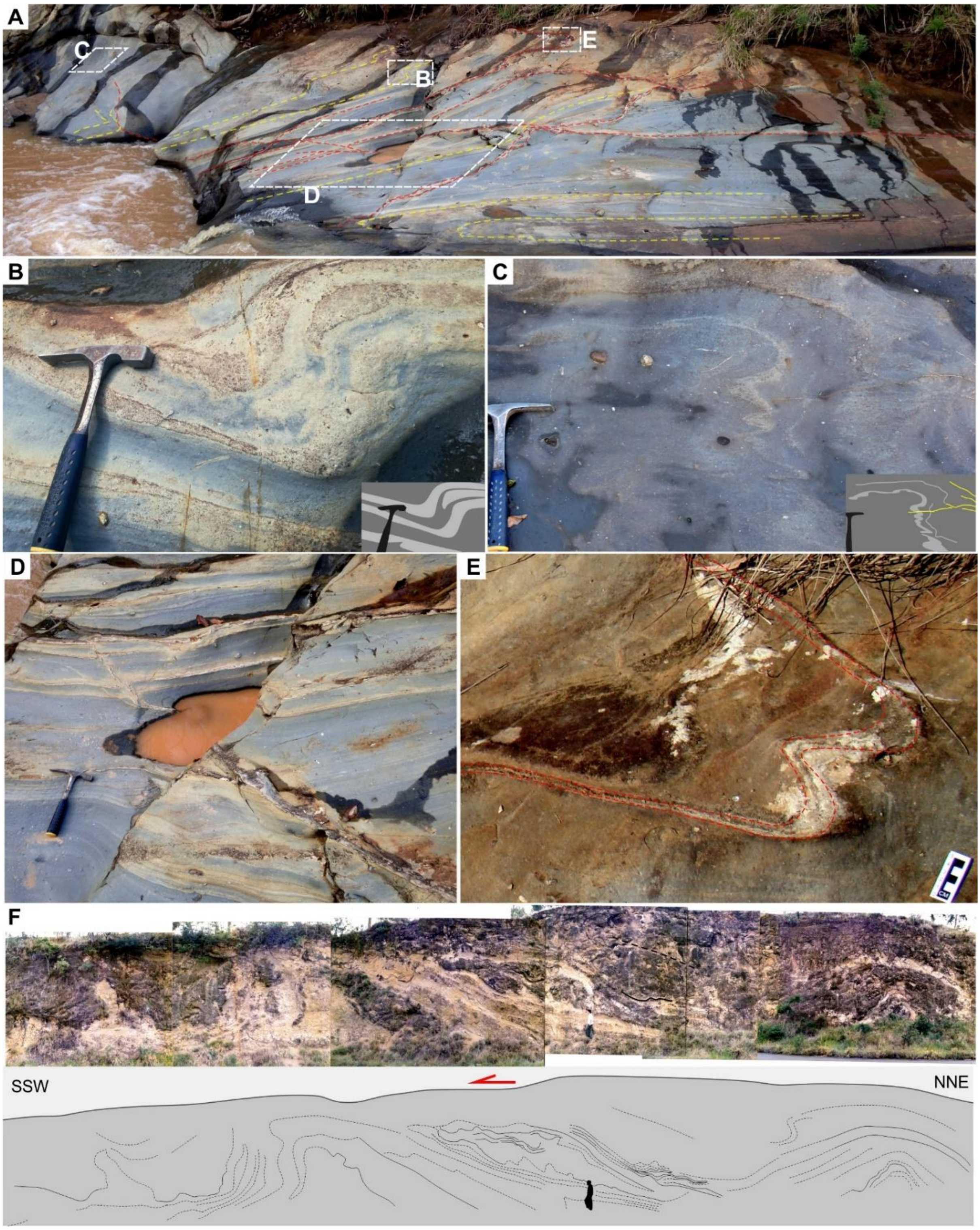

Figure 22 MTDs in the outcrops Ib-1 (A to E) and Ib-2 (F) that exemplify debris flow cases in the Taciba Formation, in the Ibaiti region. MTD outcrop Ib-1: A) Diamictite with matrix characterized by well-defined textural/compositional banding partially folded (highlighted by yellow dashed lines) and sand injections (highlighted by red dashed lines). B)

Asymmetric fold in banded matrix (Rodrigues et al., 2020). C) Banded matrix folded and locally disrupted crosscut by thin later sand injection. D) Injectites in the form of sills and dikes associated to the first stage of injection (Rodrigues et al., 2020). E) Sandy sill folded (highlighted by red dashed line) (modified from Rodrigues et al., 2020). MTD outcrop Ib-2: F) Photomosaic and interpreted sketch of mass transported diamictite with metric-scale symmentric and asymmetric folds (modified from Mottin et al., 2018).

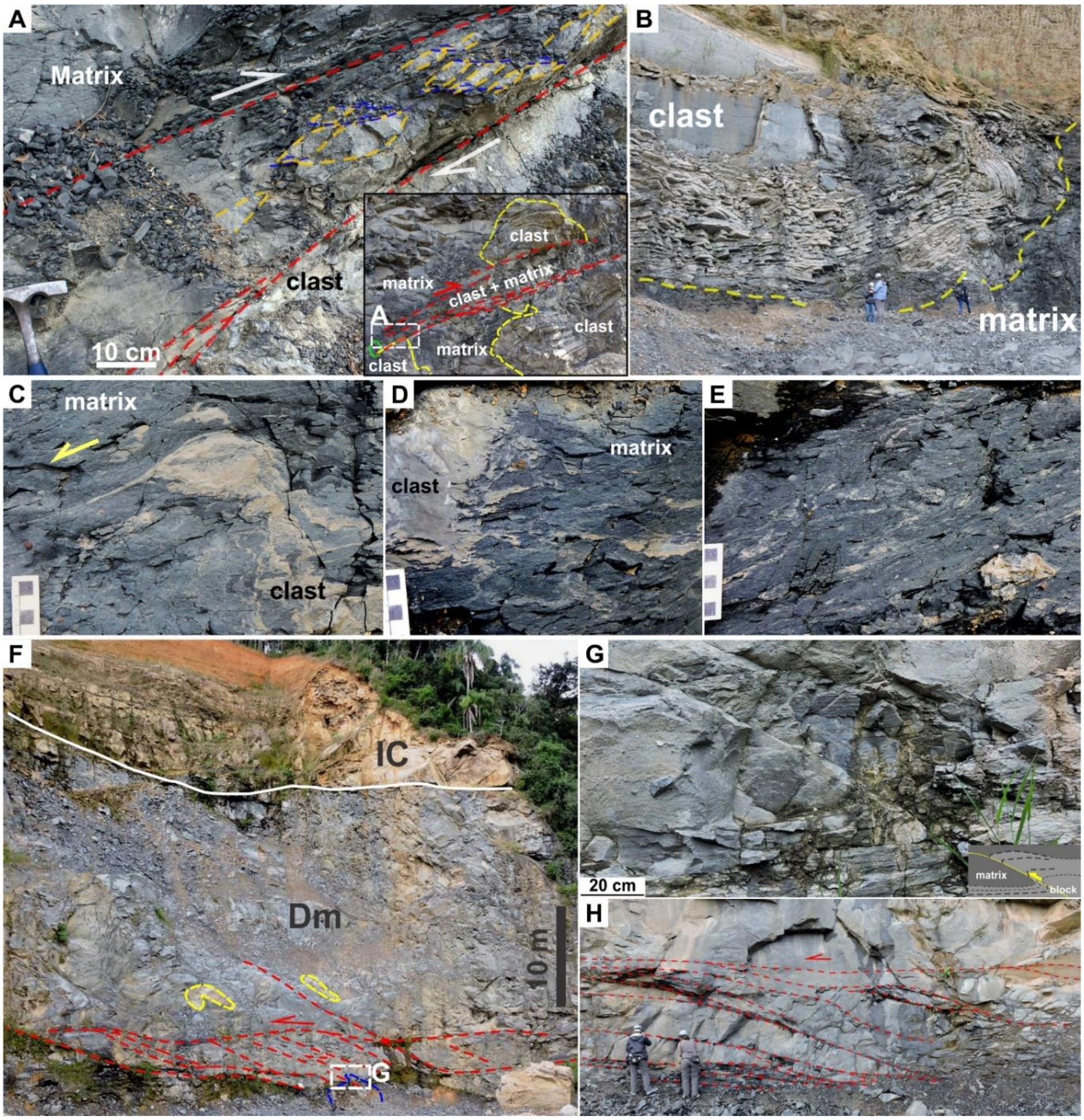

Figure 23 MTDs of the outcrops CTM-3 (A to E) and RS-2 (F to J) that exemplify debris flow cases in the Taciba Formation, in the regions of Campo do Tenente-Mafra and Rio do Sul, respectively. MTD outcrop CTM-3: A) Reverse fault that affect the diamictite matrix and intrabasinal clasts of rhythmite, which show internal deformation by folds not related to the external deformation; within the fault zone occur matrix and clasts fragments deformed, commonly with sigma shape (highlighted by blue dashed lines). B) Intrabasinal clast of rhythmite internally deformed decimetric to decametric folds (Rodrigues et al., 2020). C) Shearing at the borders of sand-rich rhythmite clast and resulting sandy films and fragments incorporated by the matrix. D) Sandstone clast with border disintegration, mutual injection (matrix injection in clast and clast sediments injection in matrix) and incorporation of clast sediment by matrix (Rodrigues et al., 2020). E) Diamicite matrix with sheared and disrupted sand lamination (Rodrigues et al., 2020). MTD outcrop RS-2: F) Diamictite (Dm) with inverse shear zones (red dashed lines) and deformed intrabasinal clasts of rhythmite (blue dashed lines) and sandstone (yellow dashed lines), and large intrabasinal clast (IC) resting on the diamictite (adapted from Rodrigues et al., 2020). G) Detail of inverse fault and associated drag fold that affect both matrix and rhythmite clast (Rodrigues et al., 2020). H) Inverse shear zones, commonly, with clay smear associated (adapted from Rodrigues et al., 2020).

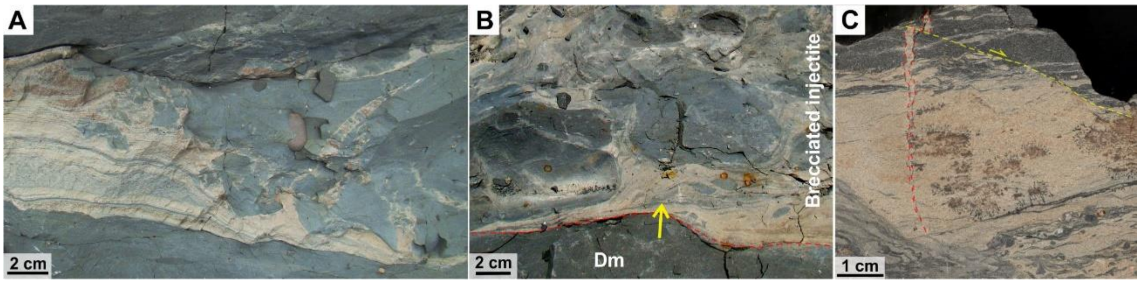

Figure 24 Other examples of sand injections identified in MTD of Itararé Group in the Campo do Tenente-Mafra (A and B) and Rio do Sul regions (C) (see location in Fig.1). A) Sandstone layer partially fluidized and injected in diamictite matrix; note the irregular portions of the host rock partially to totally enveloped by the injections. B) Breccia resulting from sand injection in diamictite; note that some host rock fragment show shearing (indicated by yellow arrow) (adapted from Rodrigues et al., 2020). C) Sand injectite that crosscuts deformed laminations of rhythmite and is also ductily sheared with the host layers. Although the parental layer is not present in the sample, it is a sand layer within the MTD.